



The InSight HP3 Penetrator (Mole) on Mars: Soil Properties Derived from the Penetration Attempts and Related Activities

T. Spohn, T. Hudson, E. Marteau, M. Golombek, M. Grott, T. Wippermann, K. Ali, C. Schmelzbach, S. Kedar, K. Hurst, et al.

► To cite this version:

T. Spohn, T. Hudson, E. Marteau, M. Golombek, M. Grott, et al.. The InSight HP3 Penetrator (Mole) on Mars: Soil Properties Derived from the Penetration Attempts and Related Activities. Space Science Reviews, 2022, 218 (8), pp.72. 10.1007/s11214-022-00941-z . hal-03918280

HAL Id: hal-03918280

<https://u-paris.hal.science/hal-03918280>

Submitted on 2 Jan 2023

HAL is a multi-disciplinary open access archive for the deposit and dissemination of scientific research documents, whether they are published or not. The documents may come from teaching and research institutions in France or abroad, or from public or private research centers.

L'archive ouverte pluridisciplinaire **HAL**, est destinée au dépôt et à la diffusion de documents scientifiques de niveau recherche, publiés ou non, émanant des établissements d'enseignement et de recherche français ou étrangers, des laboratoires publics ou privés.



Distributed under a Creative Commons Attribution 4.0 International License



The InSight HP³ Penetrator (Mole) on Mars: Soil Properties Derived from the Penetration Attempts and Related Activities

T. Spohn^{1,2} · T.L. Hudson³ · E. Marteau³ · M. Golombek³ · M. Grott² · T. Wippermann⁴ · K.S. Ali³ · C. Schmelzbach⁵ · S. Kedar³ · K. Hurst³ · A. Trebi-Ollennu³ · V. Ansan⁶ · J. Garvin⁷ · J. Knollenberg² · N. Müller² · S. Piqueux³ · R. Lichtenheldt⁸ · C. Krause⁹ · C. Fantinati⁹ · N. Brinkman⁵ · D. Sollberger⁵ · P. Delage¹⁰ · C. Vrettos¹¹ · S. Reershemius⁴ · L. Wisniewski¹² · J. Grygorczuk¹² · J. Robertsson⁵ · P. Edme⁵ · F. Andersson⁵ · O. Krömer¹³ · P. Lognonné¹⁴ · D. Giardini⁵ · S.E. Smrekar³ · W.B. Banerdt³

Received: 3 November 2021 / Accepted: 26 November 2022 / Published online: 9 December 2022
© The Author(s) 2022

Abstract

The NASA InSight Lander on Mars includes the Heat Flow and Physical Properties Package HP³ to measure the surface heat flow of the planet. The package uses temperature sensors that would have been brought to the target depth of 3–5 m by a small penetrator, nicknamed the mole. The mole requiring friction on its hull to balance remaining recoil from its hammer mechanism did not penetrate to the targeted depth. Instead, by precessing about a point midway along its hull, it carved a 7 cm deep and 5–6 cm wide pit and reached a depth of initially 31 cm. The root cause of the failure – as was determined through an extensive, almost two years long campaign – was a lack of friction in an unexpectedly thick cohesive duricrust. During the campaign – described in detail in this paper – the mole penetrated further aided by friction applied using the scoop at the end of the robotic Instrument Deployment Arm and by direct support by the latter. The mole tip finally reached a depth of about 37 cm, bringing the mole back-end 1–2 cm below the surface. It reversed its downward motion twice during attempts to provide friction through pressure on the regolith instead of directly with the scoop to the mole hull. The penetration record of the mole was used to infer mechanical soil parameters such as the penetration resistance of the duricrust of 0.3–0.7 MPa and a penetration resistance of a deeper layer (> 30 cm depth) of 4.9 ± 0.4 MPa. Using the mole's thermal sensors, thermal conductivity and diffusivity were measured. Applying cone penetration theory, the resistance of the duricrust was used to estimate a cohesion of the latter of 2–15 kPa depending on the internal friction angle of the duricrust. Pushing the scoop with its blade into the surface and chopping off a piece of duricrust provided another estimate

Note by the Editor: This is a Special Communication linked to two topical collections on the InSight Mission to Mars that have been published in Space Science Reviews. In addition to invited review papers and topical collections, Space Science Reviews publishes unsolicited Special Communications. These are papers linked to an earlier topical volume/collection, report-type papers, or timely papers dealing with a strong space-science-technology combination (such papers summarize the science and technology of an instrument or mission in one paper).

Extended author information available on the last page of the article

of the cohesion of 5.8 kPa. The hammerings of the mole were recorded by the seismometer SEIS and the signals were used to derive P-wave and S-wave velocities representative of the topmost tens of cm of the regolith. Together with the density provided by a thermal conductivity and diffusivity measurement using the mole's thermal sensors, the elastic moduli were calculated from the seismic velocities. Using empirical correlations from terrestrial soil studies between the shear modulus and cohesion, the previous cohesion estimates were found to be consistent with the elastic moduli. The combined data were used to derive a model of the regolith that has an about 20 cm thick duricrust underneath a 1 cm thick unconsolidated layer of sand mixed with dust and above another 10 cm of unconsolidated sand. Underneath the latter, a layer more resistant to penetration and possibly containing debris from a small impact crater is inferred. The thermal conductivity increases from 14 mW/m K to 34 mW/m K through the 1 cm sand/dust layer, keeps the latter value in the duricrust and the sand layer underneath and then increases to 64 mW/m K in the sand/gravel layer below.

Keywords Record of operating a penetrator on Mars · Martian soil mechanical and thermal properties · Homestead Hollow near surface structure

1 Introduction

The InSight Mars lander (e.g., Banerdt et al. 2020) is the first geophysical observatory on a planet other than the Earth and, with the exception of the geophysical instruments that the Apollo missions installed on the Moon, the only geophysical observatory on another solar system body. The goals of the InSight mission focus on the exploration of the interior structure of Mars and its evolution. An important datum for assessing planetary evolution is the present day surface heat flow from the interior as it provides an important constraint on the thermal evolution of the planet as well as an upper bound on the bulk abundance of radiogenic elements. Therefore, the payload of InSight includes a heat flow probe in addition to an ultra-sensitive seismometer with short-period and broadband sensors, transponders to track the movement of the rotation axis of the planet, a magnetometer, and a package of atmospheric science sensors. The heat flow probe, HP³, had been planned to install a string of 14 temperature sensors down to a depth of 3–5 m and measure a temperature and a thermal conductivity vs depth profile up to the target depth. The temperature sensors were imprinted on a kapton foil that was to be drawn to depth by a small penetrator, nicknamed the “mole”. The latter was equipped with temperature sensors that can be heated using a constant input power. The mole would have paused its penetration at regular depth intervals. Heating the sensors and measuring the temperature rise (24 h heating) and fall (48 h cooling) as a function of time, would have allowed a measurement of the thermal conductivity as a function of depth (Spohn et al. 2018). Grott et al. (2021) have recently published a measurement of the thermal conductivity by the mole at a depth of 37 cm, its final depth after unsuccessfully trying to dig deeper.

The design of the HP³ heat flow probe was driven by the equation for conductive heat flow q ,

$$q(z) = -k(z) \frac{dT}{dz} \quad (1)$$

where z is the depth, $k(z)$ is the depth-dependent thermal conductivity, and T is temperature. Measuring the heat flow from the interior requires measuring the temperature gradient at a depth where disturbances caused by diurnal, annual, and interannual surface temperature

variations are small enough to allow for the targeted measurement accuracy. For HP³, with $\pm 5 \text{ mW/m}^2$ as the targeted accuracy, the minimum tip depth required was estimated to be 3 m (Spohn et al. 2018). Practical considerations of mass and volume as well as planetary protection rules limited the maximum depth to 5 m. The MEPAG Special Regions Science Analysis Group (Rummel et al. 2014) found that the depth to buried ice – to be particularly well protected against contamination – in the tropics and mid-latitudes on Mars would be $> 5 \text{ m}$. The signal to noise ratio would be improved by repeatedly measuring the temperature gradient and the thermal conductivity during a significant fraction of a martian year.

After the mission had been launched on May 5th, InSight landed on Nov 26th, 2018 in western Elysium Planitia. The landing site is on the western side of a quasi-circular depression, interpreted to be a degraded $\sim 27 \text{ m}$ diameter impact crater (Grant et al. 2018; Golombek et al. 2020a; Warner et al. 2020), informally named Homestead hollow. The site features a smooth, sandy, granule- and pebble-rich surface and is located adjacent to slightly rockier and rougher terrain to the west (Rocky Field). Small craters ($< 10 \text{ m}$ diameter) are common around the lander. Some of these craters have little relief and are filled with fine grained material. Farther afield, bright circular patches or hollows interpreted to be soil-filled, degraded craters are common.

Homestead hollow has a similar morphology and soil characteristics to the degraded, sediment-filled impact craters on the Gusev cratered lava plains (Golombek et al. 2006; Grant et al. 2006) and records degradation by eolian, impact, and lesser mass wasting processes (Golombek et al. 2020a; Grant et al. 2004, 2020; Weitz et al. 2020). The origin of Homestead hollow as a degraded impact crater suggests that the crater is dominantly filled with eolian sand that is $\sim 3\text{--}5 \text{ m}$ thick in the landing ellipse, based on an initial depth/diameter ratio of 0.15 (Sweeney et al. 2018; Warner et al. 2020; Golombek et al. 2020b).

At the end of February 2019, following successful deployment of the HP³ support system assembly from the lander deck to the ground, the team commanded the mole to start penetrating. It soon became clear that the mole had failed to penetrate to the target depth of 70 cm for the first hammering session. The team tried for almost a full martian year (22 months) to diagnose the anomaly and assist the mole in penetrating deeper. The attempts were stopped in early January 2021 after it had become clear that immediate success was not to be expected and the power situation of the lander required prioritizing other instruments on InSight. In the course of trying to get the mole to dig, various data sources provided constraints on the cause of the penetration anomaly and have been analyzed to give a better understanding of the properties of the martian soil at the landing site.

In this paper, we will report in detail the operations that were performed on Mars with the mole and the robotic arm. We will further interpret the data collected from these operations in terms of mechanical and thermal properties of the regolith and its structure. In a separate paper (Spohn et al. 2022) we discuss what lessons can be learned about the design and the operation of the InSight HP³ mole. It is hoped that these can inform future attempts to use small penetrators on Mars or other extraterrestrial bodies, whether for heat flow or other scientific and exploration purposes.

Section 2 describes the physical and technical properties of the mole and its support structure. Section 3 then describes the properties of the robotic arm and camera system that was used during the anomaly resolution attempts. Section 4 describes the site selection process and outcome, and Sect. 5 describes in detail our record of operations and observations on Mars. In Sect. 5.3 we describe the geometry and the geological setting of the pit that the mole had carved during the first hammering sessions using digital terrain models derived from imaging data. In Sect. 6 we derive soil mechanical properties from the mole penetration and from the interactions of the scoop at the end of the robotic arm with the regolith.

Soil thermal properties derived from mole heating experiments are also summarized in this section. In addition, we describe the results of the interpretation of seismic signals recorded from the mole hammering by the InSight seismometer, SEIS. A synopsis Sect. 7 will conclude the paper.

2 The Mole Penetrator and Its Support Structure

The Heat Flow and Physical Properties Package HP³ (see Fig. 1) has been described in detail in Spohn et al. (2018) and will be briefly described here. It consists of the Back End Electronics (BEE) housed inside the InSight lander's thermal enclosure, the deck-mounted radiometer (RAD) to measure surface brightness temperature, and the Support System Assembly (SSA) that is deployed to the martian surface by the InSight Instrument Deployment System (IDS) (see Sect. 3 and Trebi-Ollennu et al. 2018). The Support System Assembly consists of a carbon fiber Support Structure (SS) that initially hosts the following subsystems: the Engineering Tether (ET), the Science Tether (ST), the Tether Length Measurement device (TLM), and the mole. The ET, which is actually three separate copper/kapton ribbons bonded together, electrically connects all deployed elements of the SSA to the BEE.

The critical subsystem that enables access to sufficient depth to avoid the temperature disturbances caused by annual surface temperature variations is a self-impelling cylindrical penetrator with a length of 400 mm and a diameter of 27 mm, nicknamed the "mole". Its major components are (1) its hull, with an ogive shaped tip, foils for the thermal conductivity measurement embedded in the hull, and electrical connections to the rest of HP³; (2) the internal hammer mechanism with a motor, drive shaft, cylindrical cam, drive springs, hammer, and brake spring; and (3) a shock-protected package of static accelerometers for measuring the mole tilt with respect to gravity (STAtic TILt sensors, or STATIL). The foils embedded within the hull are copper/kapton flexible heaters that can also be used as temperature sensors. To measure thermal conductivity, the mole is used as a modified line-heat source (e.g., Carslaw and Jaeger 1959; Banaszkiewicz et al. 1997) when these foils (called TEM-A, short for Thermal Excitation and Measurement–Active) are supplied with a constant power, generating heat that is then conducted to the surrounding soil. The change in mole temperature is recorded during the heating and cooling phases (24 h and 48 h, respectively) to derive thermal conductivity (Grott et al. 2021).

The mole is connected to the HP³ system by a flexible kapton/copper tether called the Science Tether (ST). This tether has two functions: First, it provides power and commands to the mole and returns data from the mole to the electronics box. Second, the ST passively measures the temperature at known points along its length. This latter function (called TEM-P, short for Thermal Excitation and Measurement–Passive) uses 14 platinum resistance temperature sensors (PT100) embedded at unequally spaced intervals along its 5 m length, which would nominally have been pulled into the ground by the Mole. The ST has markings on either edge that enable relative and absolute measurements of tether movement.

To determine thermal conductivity as a function of depth, and to properly separate the contributions of surface insolation and geothermal heat to the temperature data, the depth of the mole body and the vertical depth to the individual TEM-P sensors needs to be known with a precision of ~ 1 cm. The STATIL sensors within the mole provide its angular orientation with respect to the local gravity vector with high time resolution. The Tether Length Measurement device in the SSA uses a combination of LEDs and photosensors to optically observe the markings on the Science Tether as it is extracted by the mole during penetration. The depth of the mole body and the TEM-P sensors would have been reconstructed from the STATIL and TLM readings.

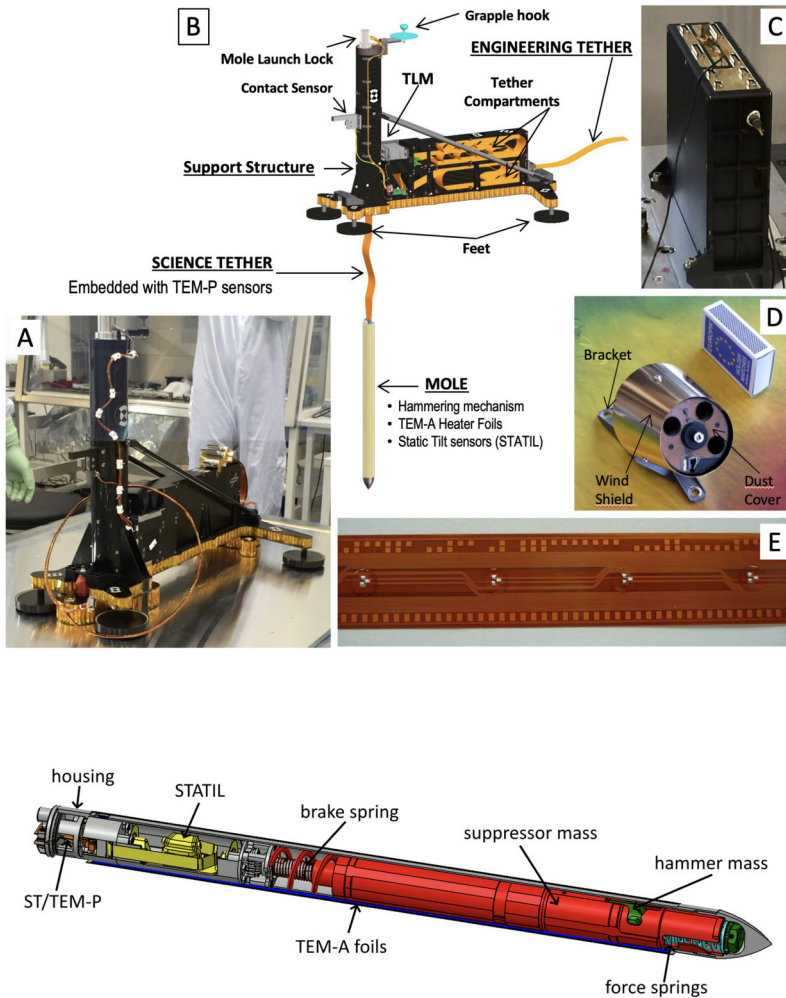


Fig. 1 Elements of the Heat Flow and Physical Properties Package (HP³). (A) Flight model Support System Assembly (SSA). (B) Annotated cutaway of the SSA showing Mole and Engineering Tether partly deployed. (C) Back End Electronics within the InSight lander, (D) Deck-mounted HP³ Radiometer (matchbox for scale). (E) Science Tether showing embedded TEM-P sensors, relative depth markings (bottom) and Gray binary code absolute depth markings (top). A prototype with closely spaced sensors is shown here for illustration; the actual flight Science Tether has greater (and irregular) spacing between sensors. The bottom panel shows an annotated cutaway of the HP³ mole (from Spohn et al. 2022) with the tiltmeter STATIL (yellow), the Science Tether ST/TEM-P attachment (orange), the TEM-A foils (purple), the suppressor mass including the brake spring of the hammering mechanism (red), the hammer mass (green), the force springs (light blue) and the housing (grey)

The heart of the mole is its hammer mechanism which has been described in detail in Krömer et al. (2019) and in Spohn et al. (2018, 2022) (compare Fig. 1, bottom panel). The electro-mechanical mechanism converts the energy of compressed drive springs into the forward acceleration of a tungsten hammer that impacts the interior anvil surface of the mole tip. The hammer mechanism assembly (motor, gear box, drive shaft, drive springs, and hammer) is free to slide within the mole hull, bound only at its aft end by the brake

spring and the wire helix. For simplicity, the brake spring and the wire helix are collectively referred to as the brake spring from here on. The mechanism is mounted in such a way that the forward force is independent of the attitude of the mole. During a hammer ‘stroke’ (consisting of an initial high-force impulsive impact, a second impact, and several lesser impacts, collectively called ‘strikes’) causes the mole to move forward into the ground. The recoil of the hammer mechanism from the strikes is largely absorbed by compression of the brake spring, with a small acceleration component transferred to the housing which must be compensated externally by friction in the soil.

The mechanism is designed such that the forward force on impact on the tip is maximized, while the recoil transferred to the housing is minimized and stretched over a comparatively long period of time. The forward force imparted to the housing from the first hammer stroke of a healthy mole has been measured in the laboratory (Wippermann et al. 2020) to be 1100 ± 150 N. In contrast, the recoil force transferred to the housing by the brake spring is only 5–7 N (Spohn et al. 2022). For the mole to make overall forward progress, this comparatively small but non-zero rebound must be compensated. This force can be provided by friction, such as from the friction springs of the support structure (see below) or by friction from the regolith. It can also come from direct physical impediment of rebound at the back of the mole such as collapsed regolith or other solid object loaded against the back cap. Without sufficient resistance-to-rebound, the mole will ‘bounce’ in place and no forward progress will occur.

2.1 The Support Structure

The design of the Support Structure (SS) was influenced by the extremely limited space available on the lander deck and by the requirement to have it stably placed on the martian surface, while allowing for cm-scale surface topography and high-velocity martian wind gusts. The Support Structure’s main parts are a vertical tube housing the mole and a rectangular box housing the tethers (compare Fig. 1). The maximum height of the tube (and thus the maximum length of the mole) were constrained by the available volume below the lander backshell that covered the deck until just prior to landing. These design constraints influenced the overall SSA shape, the number, size, and placement of its feet, and the placement of the mole and the stored tethers (see Reershemius et al. 2019). The tether storage compartment is split horizontally by a separation wall into a top compartment for the Science Tether and a bottom compartment for the Engineering Tether.

The 3.5 m long Engineering Tether is passively extracted from the aft end of the structure during deployment to the surface by the Instrument Deployment Arm (IDA, Sect. 3). After deployment, it extends across the deck down to the deployment site. The deployed SS has three key functions: 1) to support the mole in the vertical tube during the initial phase of penetration, 2) to store the 5 m long Science Tether (ST) before extraction by the mole, and 3) to host the TLM and other components fixed to the structure. The TLM sits between the Science Tether storage compartment and the vertical tube approximately one-third of the distance between the SS base and the top of the tube. The ST is threaded through the TLM and then connects to the back cap of the mole. During penetration and ST extraction, markings on the side of the tether pass by the TLM LEDs allowing light to be transmitted to photodetectors. The detector signals provide relative and absolute measurements of the extracted tether length.

It is important to discuss the location of the TLM relative to the back of the mole and how it contributed to operational decisions and the unavailability of mole depth data during early penetration. The TLM’s placement low on the central tube was driven in part by volumetric

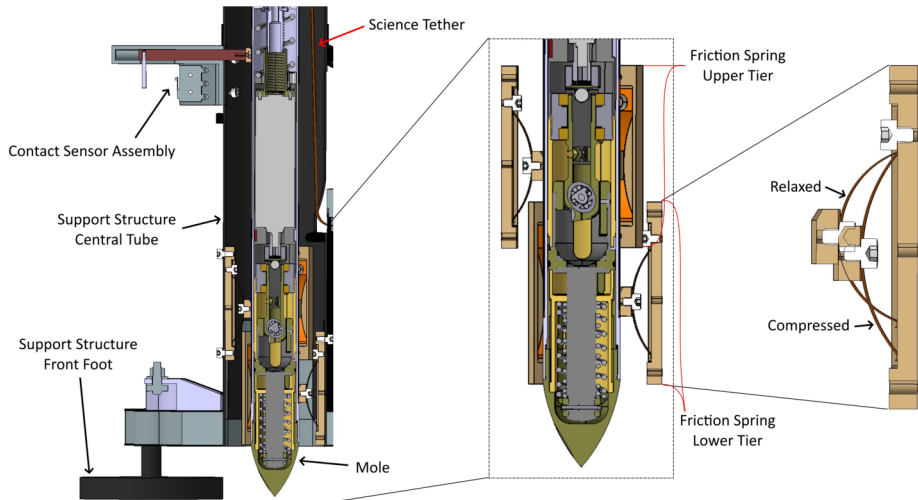


Fig. 2 This partial cross-section of the forward-front portion of the Support Structure shows the mole in its position prior to penetration. The contact sensor assembly position (top left) allows it to indicate when the mole has moved 14.8 cm out of the tube. The outlines at the center and right show the positions of the upper and lower friction spring tiers, and also the shape of the springs in their relaxed and compressed states. A portion of the Science Tether service loop can also be seen extending up from the TLM towards the back cap of the mole (not pictured)

constraints on the lander deck, and in part by concerns about SS stability in the martian wind. Without the mole inside, the carbon-fiber SS is very light (about 2.1 kg, Reershemius et al. 2019) and the 150 g TLM makes up a significant portion of the ‘empty’ SS mass. Had the SS been constructed with the TLM placed high, near the back-end of the mole, the resulting cross section’s center of pressure would have been well above the structure’s center of gravity. This would have posed a tip-over risk during the post-penetration observational phase when the SS was mostly empty. Placing the TLM low solved many issues, but created a new one: there now needed to be a ‘service loop’ in the Science Tether, passing up the central tube (see Fig. 2) between the TLM and the attachment point at the back cap of the mole. This service loop would need to be exhausted (by approximately 54 cm of mole penetration) before the ST would begin to move through the TLM and provide data.

Recognizing this dearth of data, the SS was designed with a contact sensor to provide some intermediate indication of mole penetration before TLM data became available. Located near the vertical mid-point of the central tube, it detects mole egress by changing state when the back cap of the mole passes this point (see Fig. 2). The mechanism uses a spring-loaded piston-switch connected to a tee-bar that protrudes into the central tube and loads against the outer surface of the mole. When the mole passes, the spring pushes the piston into the tube, tripping the sensor and indicating that 14.8 cm of the mole had moved out of the central tube.

One of the critical functions of the SS is to position and maintain the mole approximately orthogonal to the deployment surface for initial penetration, and to provide the necessary friction for the mole to make forward progress until (it was assumed) friction with the regolith would provide the necessary restoring force. The SS supplied this initial friction via a system of so-called ‘friction spring’ assemblies located at the bottom of the central tube. Six spring assemblies are arranged in two tiers, with the three springs in each tier spaced 120 degrees apart around the tube’s interior (see Fig. 2).

The bow-shape of each thin copper-beryllium leaf spring is fixed at one end, with the other end curled over and free to glide. Each spring is attached to a base that serves both as a mounting interface to the tube, and as a glide track for the free end of the spring. A contact block (also called ‘gliding element’) mounted on the peak of the spring touches the outer surface of the mole to provide friction. The spring assemblies are mounted with the free-gliding end oriented towards the penetration direction, allowing the mole free motion downward while resisting rebound motion.

While static, or during forward (i.e., downward) motion, the springs apply 7 ± 0.5 N force to the mole. This would tend to center the mole while allowing it to progress freely through the tube. During mole rebound, which the springs were specifically designed to resist, the contact blocks’ friction against the hull would transfer to the springs’ fixed ends, increasing inward curvature and causing a higher spring force of up to 30 ± 2 N measured horizontally on the mole, producing a self-locking effect that resists upward motion. Prior to landing, it was estimated that for an unconsolidated sandy regolith the friction springs would need to apply this reaction force until the mole was approximately 3/4 buried (Reershemius et al. 2019), after which it was assumed regolith friction would be sufficient to resist the rebound.

3 The Robotic Arm and Scoop

The Instrument Deployment System (IDS) (Fig. 3) consists of a robotic arm, two color cameras, and the motor controller electronics and software to control them. The Instrument Deployment Arm (IDA) is a robotic arm on the InSight lander with four degrees-of-freedom. It has a back-hoe design with a yaw joint (shoulder azimuth) at the base, and then three pitch joints, shoulder elevation, elbow, and wrist (Trebi-Ollennu et al. 2018).

The primary purpose of the IDA was to deploy the science payloads, lifting them from the lander deck and placing them on the surface. Additionally, it was intended to take images of the IDA workspace, lander, and martian atmosphere. The images of the workspace were used to choose the deployment locations for the science instruments and for planning the motions of the IDA (see Sect. 4).

The IDA has a camera mounted to the forearm and two end effectors: a scoop and a grapple. The scoop (Fig. 4) is an open, bucket-shaped chamber with a sharp blade, about 2.29 mm thick, at the front and a second dull blade on the outside back of the bottom of the scoop. The scoop is about 76 mm wide at the tip and 102 mm in overall length. The grapple has five fingers which can be actively opened and shuts passively. During the deployment of the science payloads to the martian surface, and during the re-deployment of the HP³ support structure to move it off of the mole (Sect. 5.2.2), the grapple hung from a compliant umbilical cable at the IDA wrist joint. During IDA operations to interact with the mole and surrounding terrain, including taking images of the HP³, the grapple was closed around a ball-and-cable grapple restraint mechanism, stowing it on the side of the IDA forearm (Fig. 4). The Instrument Deployment Camera (IDC) is a color camera with a 1024×1024 resolution and a 45×45 degree field of view (Maki et al. 2018). It is mounted to the forearm of the IDA, such that it can see objects suspended in the grapple and also providing a view of the scoop.

Stereo images can be acquired by the IDC by moving the IDA either horizontally by rotating the shoulder joint or vertically by rotating the shoulder or elbow joints. However, unlike dual camera stereo systems in which both cameras have “toe in” to point to a common spot, the IDA cannot do this so the stereo images are side-by-side requiring different

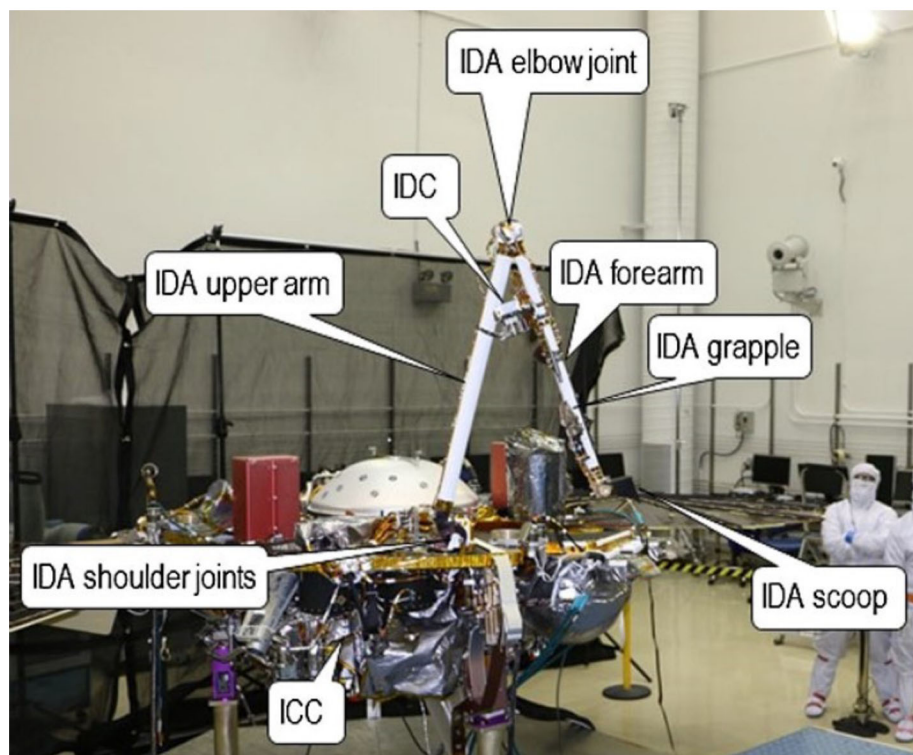


Fig. 3 The Instrument Deployment System



Fig. 4 The IDA scoop. In the left image, the scoop is shown above the HP³ mole in this IDC image. The front blade is visible. The grapple is seen stowed to the side of the IDA forearm. In the right image, the scoop in the Earth-based testbed is shown in an “inclined push” configuration on the testbed mole back cap. The dull blade on the outside back of the scoop is visible

processing to create digital elevation models, DEMs, (Abarca et al. 2019). The IDC has acquired a large number of color surface images, including stereo coverage at two resolutions (0.5 and 2 mm per elevation posting) of the instrument deployment workspace to select the locations to place the instruments, three complete stereo panoramas (morning, afternoon, and evening), and stereo images of the lander, its footpads, and terrain under the lander. In addition, higher resolution DEMs have been acquired using Structure from Motion (SFM) techniques in which more images with smaller offsets are acquired (Garvin et al. 2019). A common imaging sequence used for this technique involved a four by four matrix of images with small offsets followed by a single image of the entire area ($4 \times 4 \times 1$).

The Instrument Context Camera (ICC) is a color camera mounted to the underside of the lander deck. It has a 1024×1024 resolution, and a fish-eye lens with a 124×124 degree field of view (Maki et al. 2018). It is pointed to view most of the IDA workspace.

The IDA has approximately 2 meters of reach when fully outstretched. At the martian ground level, however, the IDA can reach 1.7 meters from the IDA base, projected to the ground, with the scoop outstretched. The HP³ was initially deployed close to the maximum reach of the robotic arm, at a distance of about 1.4 meters from the ground-level projection of the IDA frame. This limited the ability of the IDA to perform any operations that extended more than a short distance farther than the location of the mole.

The configuration of the IDA determines the force it can produce at the scoop. To prevent the IDA from damaging itself when interacting with the martian terrain, the IDA flight software and command sequences limit the torques at each of the four joints to 35, 120, 65, and 10.5 Newton-meters at the shoulder azimuth, shoulder elevation, elbow, and wrist joints, respectively (Trebi-Ollennu et al. 2018). At the location of the mole, in a configuration such that the flat bottom side of the scoop is pressing against the ground, this allows the IDA to produce an estimated peak force on the ground of about 46 N. The estimated force the IDA was capable of exerting in a lateral direction against the mole's shaft, using the shoulder azimuth joint, is about 10 N.

Hardware and software constraints limit the maximum rate at which the cameras can acquire images and save them to non-volatile memory. If using one camera only, either IDC or ICC, the maximum acquisition rate is once every 32 seconds. If using both cameras in an alternating fashion, consecutive IDC images will be spaced 47 seconds apart, and consecutive ICC images will also be spaced 47 seconds apart.

While the IDA was not intended for use to assist the mole's penetration, it provided the means to do so. The IDA was used to move the HP³ support structure off of the mole, revealing the underlying situation to the IDC camera. The scoop on the IDA was later used to push against the mole itself – thus balancing rebound – and to push and scrape the terrain surrounding the mole. The IDA and IDC were used to take close-up images of the mole, including during hammering attempts.

4 HP³ Instrument Deployment Site Selection

The highest priority activity after landing and putting the spacecraft in a fully operational configuration was determining where to place the instruments on the surface. The Instrument Site Selection Working Group (ISSWG) determined the locations to place instruments in the workspace based on the spacecraft tilt, workspace topography, surface characteristics (soils, rocks, etc.) and instrument placement requirements. Six subgroups made up the ISSWG: 1) geologists, 2) physical property scientists, 3) arm and deployment engineers, 4) Multi-mission Image Processing Laboratory (MIPL) personnel, and instrument representatives for

Table 1 HP³ deployment requirements (01–06) and desirements (07–17), and primary and secondary sub-groups who evaluated them

Req ID	Constraint	Primary	Secondary
HP3-01	HP ³ footplane tilt < 15° of horizontal	HP ³	Depl/IDS Geology
HP3-02	No rocks > 3 cm high or relief > 3 cm high under HP ³	HP ³	Depl/IDS Geology
HP3-03	HP ³ footpatch roughness < ±1.5 cm	HP ³	Depl/IDS Geology
HP3-04	HP ³ placed on load-bearing soil	Geology	Depl/IDS Geology
HP3-05	Mole egress clear of rocks > 1.5 cm diameter	HP ³	Geology
HP3-06	No partially buried rocks near the HP ³ that could be blocking the subsurface path of the mole	Geology	HP ³
HP3-07	HP ³ away from lander and other sources of thermal noise (e.g., rocks)	HP ³	< none >
HP3-08	< none >		
HP3-09	HP ³ should be ≥ 0.9 m away from SEIS and WTS shadow	HP ³	SEIS
HP3-10	Mole egress clear of rocks > 0.5 cm diameter	HP ³ , waived	Geology, waived
HP3-11	HP ³ feet clear of stones > 2 cm diameter (to prevent sliding)	HP ³	Geology
HP3-12	HP ³ on flat (enough) terrain with all 4 feet in contact with the ground, to avoid rocking during mole hammering cycles	HP ³	Geology
HP3-13	It should be checked that there are no line-of-sight obstacles obstructing the ICC field of view	Depl/IDS	HP ³
HP3-14	< none >		
HP3-15	It is desired to image all four feet of the HP ³ SS using the IDC	Depl/IDS, waived	HP ³ , waived
HP3-16	The tether should not be routed over (sharp) surface stones due to wind action over the course of the mission	Depl/IDS	Geology HP ³
HP3-17	HP ³ and SEIS engineering tether should not touch	Depl/IDS	HP ³

5) SEIS (seismometer), and 6) HP³. The workspace is in front of the spacecraft (to the south), next to where the arm is attached to the edge of the lander. The workspace extends out to roughly 2 m away from the lander and 2 m to either side in a crescent shaped area (Fig. 5). Instrument placement requirements for HP³ (Spohn et al. 2018) are related to surface slope, rocks, load bearing soil, tether geometry, and the desire to be away from the lander (and the seismometer) to reduce thermal interference (Grott 2009; Siegler et al. 2017) and are summarized in Table 1. Before landing, preliminary preferred instrument locations were identified as starting points for the site selection process, with both instruments as far as possible away from the lander and from each other, and with the seismometer to the west to avoid crossing tethers.

Within a week of landing on November 26, 2018, the IDA was deployed and began acquiring images of the surrounding terrain, spacecraft and solar panels using the IDC. The first mosaic of the workspace was available on December 10, 2018, two weeks after landing. This product was made using images acquired with all arm components above the height of the lander deck. Orthoimage and DEM mosaics with 2 mm per elevation posting were created from stereo IDC images (Fig. 5a) (Abarca et al. 2019). The workspace revealed was

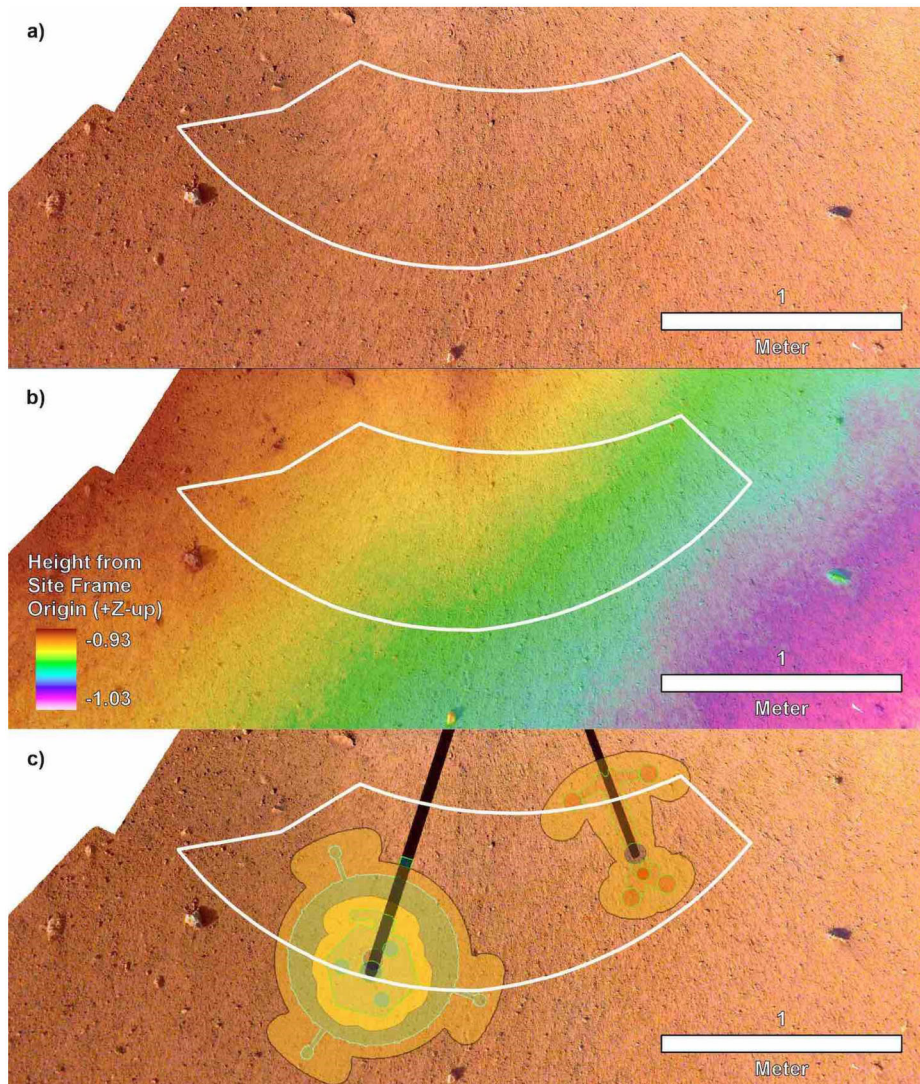


Fig. 5 Image mosaic, DEM, and instrument placements selected by the ISSWG and project. **(a)** The first IDC image mosaic created of the workspace at 1 mm/pixel with the deployment area outlined in white. **(b)** High-resolution DEM produced from the second mosaic of the workspace at 1 mm per elevation posting and the deployment area outlined in white. Note that the deployment area has a total relief measured in centimeters. **(c)** Locations selected for the instruments with black lines to the instrument grapple points. SEIS and WTS are to the left and HP³ is to the right. North is up for all

particularly accommodating, with a sandy, granule and pebbly surface, few rocks, and low slopes that met all of the instrument deployment requirements over most of the deployment area. Because of this, instrument deployment locations were both near their pre-landing preferred positions.

By pointing the arm below the lander deck and closer to the ground, a higher resolution workspace stereo mosaic was acquired by the IDC and was available on December

1st, 2018. Individual frames had a pixel scale of 0.5 mm and the DEM from these instruments had 1 mm per elevation postings (Fig. 5b). All instrument deployment requirements at the preliminary instrument locations were met (by a large margin) in the higher resolution data (Fig. 5c). In addition to meeting all HP³ requirements, all the desiresments were met except for two, which were waived because they were judged to have little impact, at the selected location (Table 1). At JPL, the InSight Deployment Testbed environment was ‘Mars-scaped’ to resemble the actual workspace on Mars. Deployment of the instruments to the selected locations was tested using an engineering model of the IDA and weight models of the instruments; these tests were successful and indicated no problems with proceeding. The instrument placement locations (Fig. 5c) were certified, approved by the instrument Principal Investigators, and selected by the project on December 17, 2018.

5 The Mole Saga: A Record of Actions on Mars

This section provides a chronological narrative of the actions taken on Mars from the first attempt to penetrate into the subsurface (sol 92) through the cessation of penetration anomaly response activities (sol 754). This narrative reflects several co-evolving understandings and attitudes within the anomaly response team including: (1) a narrowing, by process of elimination, of the root causes and contributing factors to the mole’s poor penetration performance, (2) a growing understanding of the properties of the martian regolith at the landing site, (3) a progression in project risk posture with respect to assets such as the science tether, the robotic arm, and the mole itself, (4) an increase in activity complexity (e.g., from simple commands for more hammering to complex activities involving precise arm positioning and loading), (5) the success, failure, or exhaustion of a particular assistance approach, and (6) the accommodation of dwindling resources to combat the anomaly, including those available on Mars (e.g., power) and on Earth (e.g., operational personnel and schedule encumbrances).

Consideration of the above factors lead to a particular order of operations, such as the choice to pin the mole with the scoop prior to attempting pit infill. Methods used in later stages of the anomaly resolution, such as pushing directly on the mole back cap and scraping regolith into the pit, were evaluated early in the process but initially tabled due to a lack of understanding of the environment, confidence in operational capabilities, and/or a perception of high risk. As the team’s understanding grew and the option space shrank, some (but by no means all) of these considered methods were brought back into play. The enumeration of all decision points, risk rankings, and descriptions of paths-not-taken is beyond the scope of this paper. Where possible, the driving factors on the choice to pursue or abandon a given method are given in the narrative.

One further driving consideration deserves elaboration: the scientific motivation to get the mole to its operational depth (≥ 3 m) as fast as possible. The mole targeted a tip depth of 3–5 m due to its requirement to emplace temperature sensors below significant influence of the annual thermal wave. Upon arrival, however, the InSight lander introduced a step-function change in the local thermal boundary conditions by removing surface dust and decreasing the albedo (Golombek et al. 2020a). This introduced a new shadow pattern and a new perturbation of the surface energy balance. The perturbation propagated into the regolith (see Grott 2009; Siegler et al. 2017), introducing a new thermal wave that would complicate the interpretation of the temperature data. The team hoped to emplace the mole as rapidly as possible, outrunning the downward-propagating lander effect while still meeting other constraints, such as making multi-sol thermal conductivity measurements during penetration

Table 2 The Mole Saga: phase names, sol intervals, and summary descriptions

Phase	Sols	Description
Initial Attempts (IA)	92–94	Two initial hammerings commanded w/ stop triggers of 4 and 5 hours, respectively, or a 0.7 m depth reported by TLM. TLM does not report any ST extraction; STATIL reports significant tilt changes, some SS motion observed via footprints
Diagnostics & Lift (D&L)	97–211	Information gathering via imaging campaigns at various times of day and IDC positions, imaging of the SS ‘window’, and two short diagnostic hammerings. SS is re-grappled and lifted away from the mole in three steps.
Pit Characterization (PC)	220–234	Imaging of mole, pit, and surroundings
Regolith Interaction 1 (RI-1)	237–257	Flat scoop pushes and chop tests attempt to collapse the pit
Pinning 1 (P1)	291–318	Mole is pinned horizontally and vertically – successful penetration of ~ 5 cm proves there is no obstructing stone
Reversal 1 (REV1)	322–325	Reconfiguration of the arm to protect the ST removes direct contact with the mole resulting in insufficient resistance to rebound, a mole reversal event extracts ~ 18 cm of the mole
Pinning 2 (P2)	329–380	Mole is pinned horizontally and vertically. Successful and fast penetration permits recovery from the reversal event to approximately the same depth as at the end of Pinning 1
Reversal 2 (REV2)	400–407	Mole is pinned with vertical preload only – another reversal event occurs, extracting ~ 5 cm of the mole
Regolith Interaction 2 (RI-2)	414–420	A regolith scrape test is performed, and chops are executed in an attempt to further collapse regolith into the pit
Back Cap Push – Horizontal Scoop (BCP-H)	427–577	The mole is incrementally pushed by the scoop on its back cap, providing direct resistance to rebound and allowing the mole to descend ~ 7 cm until the back cap is flush with the surface
Regolith Interaction 3 (RI-3)	598	Regolith is scraped into the pit, obscuring most of the mole
Back Cap Push – Inclined Scoop (BCP-I)	604–645	The mole is incrementally pushed using an inclined scoop, allowing the back cap to descend to ~ 2 cm below the surface
Regolith Interaction 4 (RI-4)	659–700	More regolith is scraped into the pit; each scrape is followed by a flat-scoop tamping action
Final Free Mole Test (FFMT)	754	The scoop is positioned as for the Back Cap Push to prevent mole reversal. 500 strokes are commanded, but no forward motion is observed.

and allowing sufficient time for the thermal energy of hammering to dissipate. Ultimately HP³ lost this race, but its influence on early anomaly response decisions was significant.

Table 2 names the major phases of the Mole Saga, the sols covered by each phase, and the major activities and results of the events of the phases. Unless otherwise specified, the distance from the mole back cap to the original regolith surface, as measured along the mole body (i.e., ‘along-mole distance’) is reported below. The depth of the mole tip measured along the mole body is obtained by subtracting the back cap distance from the length of the mole of 40 cm. Vertical tip depths underground can be determined by multiplying the latter by the cosine of the mole tilt.

This section includes three key figures for reference throughout the discussion: Fig. 6 shows a linear timeline of all actions taken on Mars in the 22 months (662 sols) between the

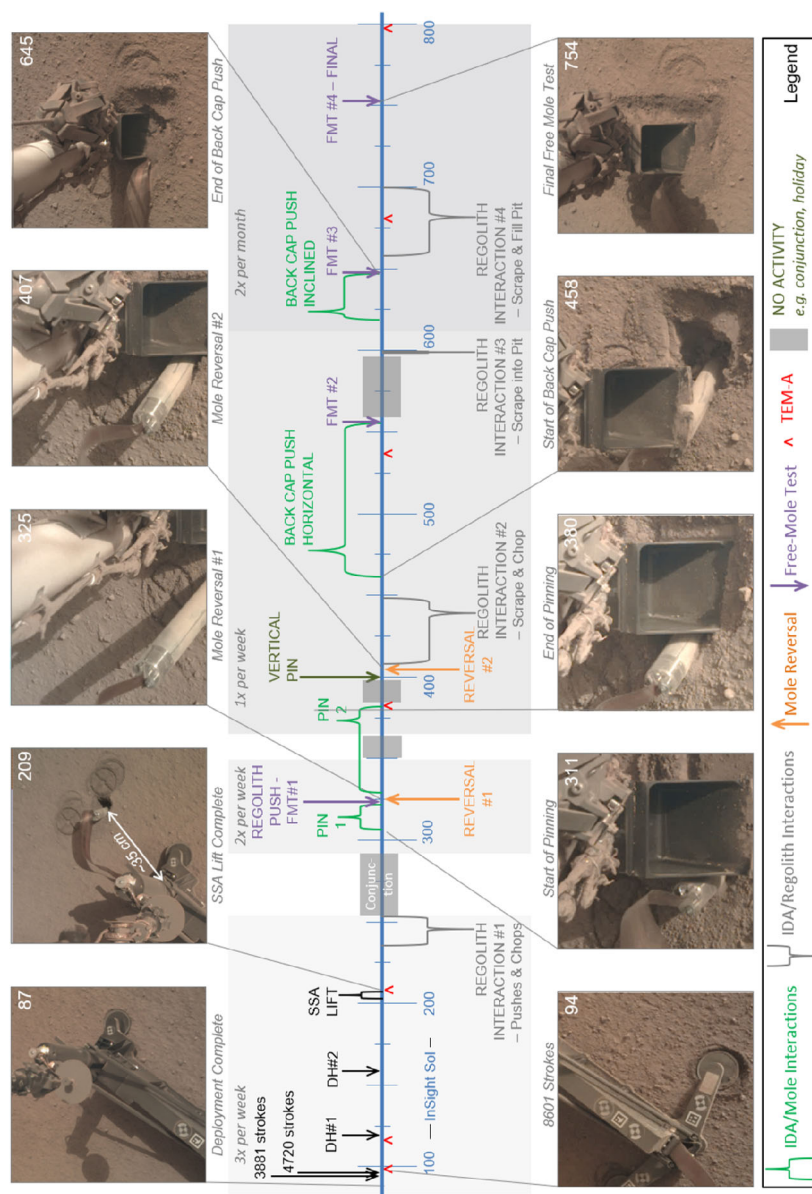


Fig. 6 This linear timeline shows key periods (braces) and events (arrows and caret) of the mole penetration anomaly from the end of SSA deployment (Sol 87) to the final Free-Mole Test (Sol 764). Callout figures with sol numbers in the upper right show selected zoomed views from the IDC. Shaded background regions indicate changes in operational cadence

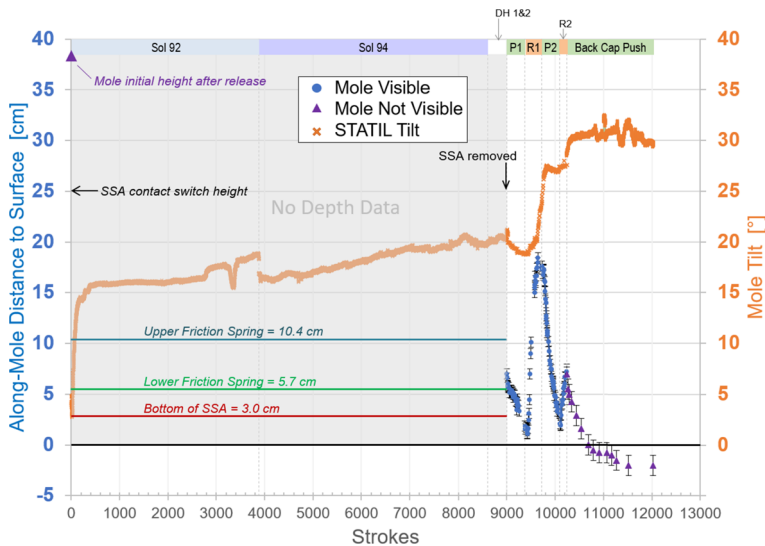


Fig. 7 This plot shows (left axis, circles and triangles) the distance along-mole from the mole back cap to the original regolith surface (zero datum), and the tilt of the mole with respect to local gravity (right axis, x's) as measured by STATIL; both axes are referenced to the total number of hammer strokes accumulated since sol 92. Blue circles indicate along-mole distance to datum as determined from IDC images of glint features on the mole back cap. Filled purple triangles indicate along-mole distance determined through various indirect means (e.g., SSA contact switch or IDA scoop/regolith relative position)

first hammering attempts and the final Free Mole Test. Figure 7 plots, for the entire timeline, the mole back cap distance to the regolith ('along-mole distance' on the left-hand axis) and mole tilt (right-hand axis) as a function of hammer stroke. And Fig. 8 presents a zoom-in on Fig. 7, highlighting the mole distance and tilt during the period when it was assisted by the robotic arm, from the first pinned hammering on sol 308 to the final Free Mole Test on sol 754.

The supplementary material contains a table with a sol-by-sol breakdown of all actions on Mars including number of commanded hammer strokes. STATIL data on mole tilt presented in the figures and discussed in the text are derived from a combination of data from the STATIL "A" and "B" channels, representing the 'x-tilt' and 'y-tilt' channels from just one of the two STATIL sensors.

5.1 Initial Attempts: Sols 92 & 94

After successful deployment of the HP³ SS to the martian surface on sol 76, the grapple was adjusted and released (sols 79, 81, 83), and placement position was confirmed via mosaic imaging (sol 85). Once placement was confirmed, the mole was released from its launch lock on sol 87. Launch lock release represented a committal of position: the mole was now free of the support structure and, though supported internally by the friction springs, could no longer be moved to any other deployment location. Upon release, the mole was expected to drop under gravity from its locked position, allowing the tip to penetrate into the uppermost dust layer by ~ 1 cm. It is believed this occurred as expected, though no confirmation of the actual tip penetration due to this gravity drop can be given.

On Sol 92 the first hammering was commanded with a target depth of 70 cm. Due to the length of the Science Tether service loop between the TLM and the back cap of the mole

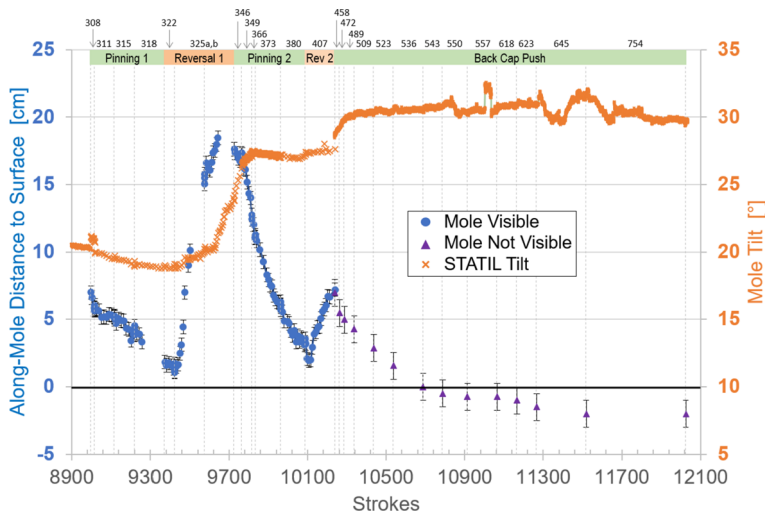


Fig. 8 This plot zooms in on data shown in Fig. 7 beginning on sol 308 when the first pinned-mole hammering test was executed. Symbol colors and meanings are the same as in Fig. 7. Note the different scales for the left-hand axis (back-cap distance to surface) and right-hand axis (mole tilt from STATIL). Individual sols where hammering occurred are indicated along the top border; vertical dashed lines show the boundaries of each sol's planned hammer strokes. The major periods of successful mole penetration (Pinning 1, Pinning 2, and Back Cap Push) are indicated by green horizontal bars along the top, while major periods of mole reversal (Reversal 1 and Reversal 2) are in orange

(~ 29 cm), the ST was not expected to engage in the TLM until the mole tip reached a depth of ~ 54 cm. The target depth of 70 cm was chosen to allow absolute depth markings on the science tether to be read by the TLM and so provide the stop-hammering command to the HP³ electronics. Data from penetration tests at DLR Bremen and at JPL (Wipperfmann et al. 2020) in a variety of regolith simulants led to the expectation that the mole would reach this target depth within the first 30 minutes (or ~ 500 strokes) of hammering. Motivated by the desire to penetrate to target depth quickly, a nominal hammering timeout period of 4 hours was set to allow for the possibility that the shallow regolith was more difficult to penetrate than in any of the terrestrial tests.

The penetration anomaly was first recognized when data from the first hammering attempt indicated that the mole had hammered for the full 4 hours (later determined using mole motor current data to be ~ 3881 hammer strokes) and no data was reported from the TLM. Data that were also available at this time included: (1) The mole back cap passed the contact switch (24.5 cm above the regolith surface) 4 minutes 54 seconds (77 strokes) after hammering began. (2) STATIL reported significant tilt changes, with the greatest magnitude occurring in the first 11 minutes (~ 170 strokes), see Figs. 7 and 13. The final reported tilt was 16° with respect to gravity. (3) At an unknown time or times during the interval, the SS moved along its long axis towards the InSight lander by ~ 1.7 cm, as revealed by footprint markings of the initial placement site.

Assumptions at the time, informed by terrestrial penetration experiments, suggested that over-large resistance in the regolith (either a stone or unexpectedly dense material) was a likely culprit for the poor penetration performance, since all telemetry indicated a fully functioning instrument. A large stone entirely blocking the path of the mole was considered unlikely, though, based on pre-mission studies of the likelihood of penetration to the target depth (Charalambous 2014; Golombek et al. 2017). So, on sol 94, a second hammering

period was commanded with the same 70 cm target tip depth and a 5 hour timeout. As with the first attempt, no readings were recorded by the TLM and the mole timed out after 5 hours (4720 strokes).

During the second interval, the following were observed: (1) The overall tilt as reported by STATIL increased slowly from $\sim 16^\circ$ degrees to $\sim 20^\circ$, reaching a $\pm 1^\circ$ plateau in the last third of the Sol 94 hammering. The jump in reported angle from 18 degrees to 16 degrees between sols 92 and 94 is likely due to an offset caused by TEM-A being active during sol 92 as an auxiliary heat source for the unburied mole. TEM-A and STATIL use the same ground line. There was likely no actual change in mole tilt between the two sols and the absolute tilt values recorded for sol 94 are considered more reliable. (2) At an unknown time or times during the second interval, the SS again was moved, leaving footprint impressions in the regolith. This time the movement appeared as a rotation of ~ 4 degrees anti-clockwise around a pivot at the rear edge of the aft right foot. The clear impressions of the SS feet edges and internal cross struts, as opposed to scrape marks, suggested that the SS was partially lifted; this is explored more in Sect. 6.

5.2 Diagnostics & SS Lift: Sols 97–211

5.2.1 Diagnostics

From sol 97–158, a multitude of images were taken with the ICC and the IDC (the latter with the IDA in various poses) at various times of day to try to reveal more about the mole's attitude and what was preventing forward motion. Images were taken near sunrise and sunset to try to observe long shadows under the SS (these were unsuccessful in providing new information). There were some hints of the mole and the yet-to-be-discovered pit in the ICC images, but these were at the limit of the camera's resolution and interpretation remained ambiguous until later. Contrast-stretched images of the small 'window' in the back of the SS's central tube revealed that the science tether was still inside, though it appeared to be in a skewed position. Two TEM-A measurements performed on sol 97 and 116 revealed that some portion of the mole was above ground and subject to diurnal temperature fluctuations.

On sols 118 and 158, two so-called 'Diagnostic Hammerings' were conducted of 197 and 198 strokes each (about 12.5 minutes of hammering), while the IDC was posed to take 'movies' of the SS and the Science Tether via a small window at the rear of the tubular housing of the mole. As described in Sect. 3, the camera software limited the maximum rate of image acquisition. In the case of sols 118 and 158, both IDC and ICC were used in parallel, limiting the cadence of IDC images to one every 47 seconds. Nonetheless, the movies so acquired revealed that the SS was jostled about during hammering, though no significant net motion such as occurred in sols 92 and 94 was observed. The window imaging did not show unambiguous motion of the science tether.

During the Diagnostic Hammerings, the SEIS instrument adopted a different digital filter configuration enabling it to listen more precisely to the individual 'strikes' of the hammering mechanism. If the timing between strikes could be determined with sufficient accuracy, this could serve as a proxy for the health of the hammering mechanism (see Sect. 6.5 below). Laboratory experiments suggested that the timing between the 1st and the 2nd strike differed markedly between a penetrating mole and a mole hammering against an obstacle. Since at this point it was still a possibility that the mole had been stopped by a large stone, it was hoped that analysis of the acoustic properties of the hammer strikes might provide clues. Unfortunately, the data were inconclusive.

The data acquired during this period were analyzed and possibilities were debated amongst the team. All signs appeared to point to a healthy mole, leaving three categories of root cause: (1) External Obstruction: the mole was obstructed by a large stone or an otherwise pathologically impenetrable regolith layer. (2) Internal Configuration: the mole and/or science tether was snagged or otherwise physically inhibited by the support structure. Or (3) lack of sufficient friction between the mole hull and the regolith. Having exhausted the available sources of information, a plan was devised to remove the SS.

5.2.2 Support System Assembly Lift

The plan to remove the SS from the embedded mole had three main advantages: (1) if successful, it would eliminate the Internal Configuration category of root cause, (2) it would provide a clear view of the mole's state and the state of the surrounding regolith, and (3) it would open up avenues for the IDA to directly or indirectly assist the mole. Still, the lift was a risky proposition: STATIL data and the observed SS motion suggested that the mole had rattled around against the SS quite a bit, possibly resulting in an off-nominal tether configuration with respect to the springs. If the tether or the mole were snagged, lifting the SS could extract the mole further from the ground.

To assess and react to these concerns, the lift was thus performed in three stages with ground-in-the-loop assessment after each stage. After the IDA grapple had been unstowed and successfully re-grappled the SS grapple hook, the SS was lifted 12 cm on sol 203. Analysis of the SS position relative to initial deployment, internal SS geometry, and mole tilt together implied that the back cap was no more than ~ 10 cm above the regolith surface, so 12 cm was chosen as the amount of lift needed to ensure that the SS was clear of the mole, and that the narrowest (i.e., most snag-prone) portion of the science tether was below the friction springs. Lift stage 1 was successful, there being no anomalous SS tilting or apparent mole extraction as seen in ICC images. At the end of the lift, IDC images revealed a portion of the mole and also provided the first clear pictures of what became known as 'The Pit.'

The second stage of the lift, performed on sol 206, lifted the SS an additional 13 cm, for a total SS lift of 25 cm. This amount was needed to exhaust the science tether service loop and pull a small amount of it through the TLM. Ground-in-the-loop confirmed that 7.6 cm of tether was extracted through the TLM with no anomalous SS tilting and no apparent movement of the mole, thus indicating a successful lift.

The final stage of the lift on sol 209 lifted the SS an additional 29 cm vertically (for a total lift of 54 cm), thereby extracting sufficient science tether slack to allow the SS to be placed away from the mole. The SS was then brought down in a step-wise fashion to a point closer to the lander, ultimately being placed with the SS's mole egress point ~ 35 cm from the center of the pit. The lift operation completed successfully and the mole, pit, and science tether were now clearly visible. This phase closed with a further TEM-A measurement on sol 211 (this was not useful for thermal conductivity, but was performed to observe the difference between a shadowed mole and one exposed to the sun and sky).

The close of this phase saw the team in possession of new data: (1) The mole height above the regolith was observed to be ~ 7 cm (along-mole distance to the original regolith surface). (2) The mole azimuth pointed to the southwest and its body appeared to rest against the northeast corner of the pit. (3) The pit itself had irregular yet nearly vertical walls and a depth of ~ 5 cm or more, indicating the presence of a cohesive layer (a.k.a. duricrust) much thicker than any that had been anticipated. This observation lent significant strength to the lack-of-friction hypothesis.

5.3 Pit Characterization & Regolith Interaction 1

From sol 220–234, closeup and mosaic images were taken of the mole, pit, and surroundings at various times of day. Mid-day images provided good illumination into the pit, further revealing its irregular southerly and westerly nearly vertical walls and significant depth. Figure 9 shows the results of digital elevation models of the pit and Fig. 10 shows a close-up image of the pit's southerly wall with part of the mole in the foreground. The maximum depth of the pit, its volume and average depth depend on a definition of a reference surface. Using the yellow dashed line in the middle panel of Fig. 9 tracing the rim of the pit as reference, the maximum depth is 72 mm, the volume is $6.73 \times 10^4 \text{ mm}^3$ and the average depth is 19.3 mm. Using the 0.085 m contour line in the DEM as reference, the respective values are 69 mm, $5.4 \times 10^4 \text{ mm}^3$, and 20.1 mm. The volume estimates do not include the mole which contributes $1.1 \times 10^4 \text{ mm}^3$ to $1.5 \times 10^4 \text{ mm}^3$ depending on the average depth of the pit. The mole blocks the view to a significant part of the bottom of the pit. It is unknown whether or not additional volume of the pit is to be found there. Some of the layers within the pit have pebbles that appear cemented in a finer-grained matrix (Fig. 10). These steep, resistant layers are similar to the duricrust observed in the pits beneath the lander and the clods of material scattered during landing.

A review of the geologic history of the landing site finds no significant amounts of surface or subsurface liquid water since the deposition of the Hesperian basalts (Golombek et al. 2017). Any geomorphic features that form from water (liquid or solid) are completely absent and the hydrogen level in the area is low. However, the observed duricrust could have been cemented by salts deposited by low water-to-rock ratio weathering by thin films of water via interactions of atmospheric water vapor and soils as suggested by chemical measurements by Viking and Mars Exploration Rover spacecraft (Banin et al. 1992; Haskin et al. 2005; Hurowitz et al. 2006).

By this time, the remaining root causes for the mole penetration anomaly had been reduced to two possibilities: There was an external obstruction, or there was insufficient friction provided by the surrounding regolith. Or perhaps both. In an attempt to address the latter problem by collapsing the pit walls to provide more regolith friction, the IDA scoop was brought down to touch the regolith in two types of interactions: A flat scoop push, wherein the broad flat side of the scoop was pressed into the ground (sol 240 and 253), and a vertical chopping motion performed with the scoop's flat edge vertical and the tip pointed normal to the surface (sol 243, 250, and 253). The scoop flat push resulted in a sharply defined area, approximately 0.5–1 cm deep (Fig. 11), resulting from the compaction of an unconsolidated layer see Sect. 6.4). The chopping activities were largely unsuccessful at collapsing the pit, although the chop on sol 243 did break off a small wedge (1 cm \times 1 cm) that fell into the pit. Neither the chopping nor pushing attempts resulted in a significant change in pit morphology below the surface compacted layer. The small collapsed wedge did however provide constraints on estimates of the consolidated layer strength which is evaluated in Sect. 6.4.

5.4 Pinning 1

Nothing could be done about a subsurface stone or other obstacle blocking the mole. However, the low abundance of large stones at the surface and other considerations of landing site geology (e.g., Golombek et al. 2020a), weakened this hypothesis. Instead, if lack of friction was the cause, application of force on the mole from the IDA could help overcome the deficiency enough to get the mole to a depth where it could dig on its own. By positioning the scoop adjacent to the mole and then overdriving the arm both horizontally and

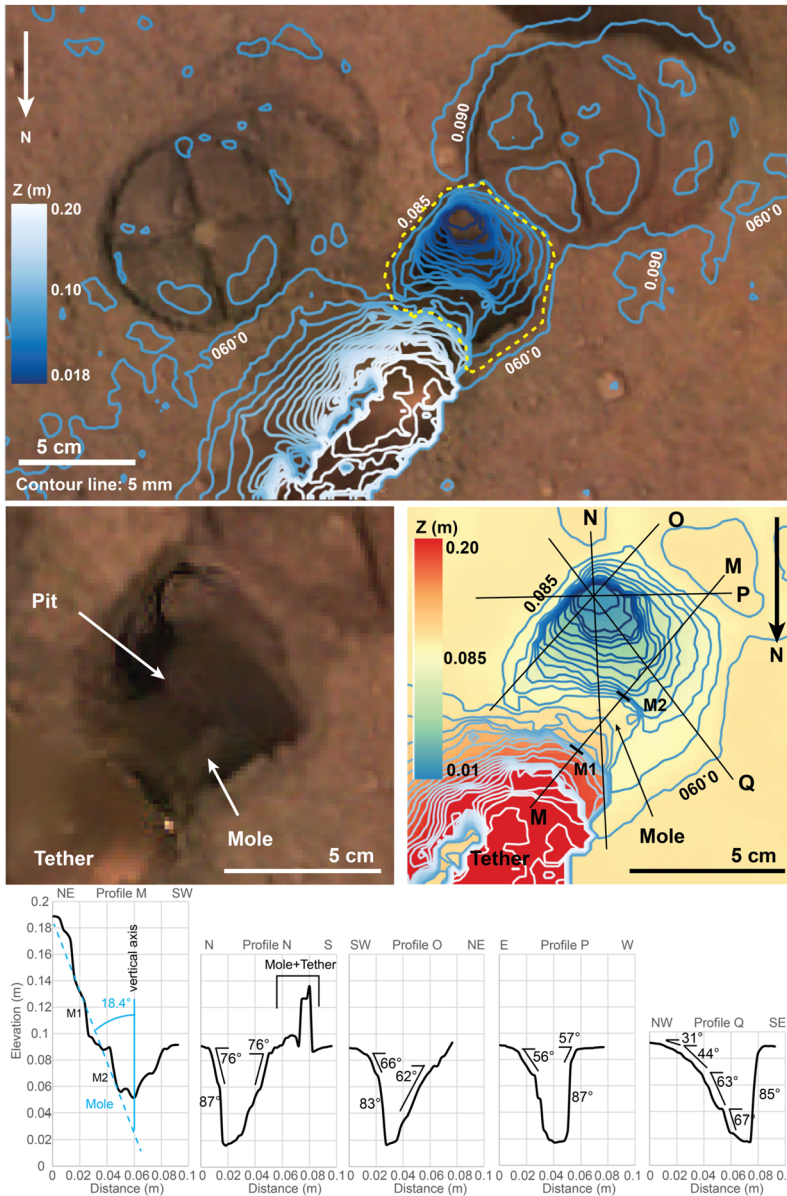


Fig. 9 Digital elevation model of the pit based on a $4 \times 4 \times 1$ IDC imaging data set taken on sol 230 after SSA replacement and using virtual control point methods. The top frame shows 5 mm depth interval contour lines superimposed on the orthorectified image mosaic. The rim of the pit is marked by a yellow dashed line. In addition to the pit, the imprints of the SSA feet in the fine-grained surface layer are clearly seen as well as the tether connected to the back-end of the mole. Below the top frame, from left to right, a close up orthorectified image of the pit is shown and a colour-digital elevation model (DEM) of the pit in which the reference elevation plane is 2 cm below the deepest point of the pit. Labelled black lines correspond to the location of topographic profiles M–Q shown in the panels in the bottom row. Profile M extends all along the mole between points M1 and M2 and up the tether. The average slope between M1 and M2 is 18.4° which compares well with the tilt angle of the mole measured by STATIL of $20 \pm 1^\circ$. Selected measured topographic slopes are given



Fig. 10 Image of the hole created by the HP³ mole showing the almost vertical southerly wall of the pit and resistant layers in it. These layers have steep edges and overhangs indicating cohesion in the soil. Small rocks appear cemented in a fine-grained matrix, similar to the pits beneath the lander. Mole is in the foreground angled $\sim 15^\circ$ towards the right

vertically into the mole hull ('pinning' the mole), the frictional force between the mole and scoop and between the mole and the regolith beneath could be increased. It was hoped that this increased friction would exceed the 5–7 N rebound force threshold and allow the mole to make forward progress.

We used the seismometer as a tiltmeter to monitor the quality of the preload force exerted by the IDA. By low-pass filtering the seismometer response to the loading and unloading IDA motions, we could compare the relative magnitudes of the forces exerted by the IDA by



Fig. 11 Image of mole hole and surface after interactions with the HP³ SSA feet and scoop. Circular cross patterns are imprints of the HP³ SSA feet in the soil. Smooth, reflective rectangular surface is where the flat base of the scoop (7.1 cm wide) was pressed against the soil, causing a 5–10 mm indentation. Horizontal troughs near the top and bottom of the scoop imprint are where the front and back blades of the scoop (Fig. 4) penetrated into the soil

comparing the tilts induced by loading, during hammering, and unloading. We found that the preload exerted by the IDA was maintained across intervals of weeks of no activity. During hammering, the preload when pushing directly on the regolith was generally progressively reduced. When pushing on the side of the mole, the preload was largely maintained, though some instances showed some decrease.

From sol 291–305, the IDA was brought into position and pinned the mole at a point ~ 3 cm above the regolith surface. On sol 308, 20 hammer strokes were commanded. The resulting movie using only the IDC (image cadence: 32 seconds) showed some barely perceptible (~ 5 mm) motion downward, as well as mole rotation around its long axis. There was no significant change in overall tilt reported by the STATIL sensors, though they did confirm that the slight rotation of the mole during these 20 strokes was a real effect. The tendency of the mole to rotate during hammering around its long axis is a consequence of an uncompensated small torque in the hammer mechanism. The resulting torque is usually mostly compensated by friction. It has been observed in the laboratory and had not caused any concern.

In the period from sol 308 to 598, the back cap of the mole was visible to the IDC, allowing the distance-to-regolith to be determined from image analysis. The technique used tracked a solar 'glint feature' at the edge of the back cap whose position was invariant to mole rotations. In this period, mole hammerings and the associated IDC images occurred around the same time in mid-afternoon, providing a similar sun angle. This reference point provided the location of the mole in IDC image space. The width of the mole in pixels was measured at the same longitudinal position. This was used along with the known mole width (27.0 mm), mole tilt, and camera resolution (0.82 mrad/pixel) to derive the glint's range from the camera. Each image was additionally co-registered to the base map of the workspace (taken on sols 16 and 243) to get an absolute, consistent reference frame for the camera model. This adjusted camera model was then used to convert the glint location and range into XYZ coordinates, thus providing its position. Accumulated analysis errors result in an uncertainty of back cap height of ± 0.5 mm, shown by the error bars in Figs. 7 and 8.

On sol 311, the IDA was commanded to move down by 5 mm. This vertical re-pinning motion was accommodated by the scoop sliding along the inclined surface of the mole, thus increasing both vertical and horizontal loading. Following this motion, 101 hammer strokes were commanded.

The 101 strokes commanded on sol 311 resulted in a downward motion of the mole of ~ 1 cm. This obvious motion of the mole into the regolith was a major event. Had there been an obstructing immovable stone or impenetrable gravel layer, there would have been no forward motion. Recall that the IDA was not pushing the mole into the regolith but only loading it from the side; all downward progress was due to mole hammering while under this limited lateral loading of 10 N at most. Unambiguous proof was finally in hand that there was no rock blocking the mole and the External Obstruction branch of the fault tree could be eliminated. This became clearer still when further hammering was commanded on sols 315 (101 str.) and 318 (152 str.). Sol 315 hammering was preceded by another 5 mm downward motion of the IDA, but sol 318 hammering had no preceding arm motion. Together, the pinning technique had resulted in a combined motion since sol 308 of ~ 5 cm into the ground. Each forward motion was accompanied by further anti-clockwise rotation of the mole. At the end of sol 318, the mole back cap was ~ 1.5 cm above the original regolith surface, see Fig. 8. The penetration rate had been 0.6 mm/stroke for the 20 strokes on sol 308 but with the depth progress not as well resolved as between sols 311 and 318. For these, it varied between 0.07 mm/stroke and 0.15 mm/stroke, 0.1 mm/stroke on average for a total of 400 strokes (compare Fig. 15).

5.5 Reversal 1

Tactics now needed to change. The vertical motions of the scoop against the sloped side of the mole during sols 311 to 318 resulted in a horizontal as well as vertical preload (stored in the compliant composites of the IDA). More mole motion would move the mole back cap below the scoop edge, resulting in a side-swipe of order one mole diameter that could potentially damage the science tether. Rotation during hammering had unfortunately oriented the mole such that the tether plane was in-line with the preload direction, maximizing the potential for tether damage.

How then to continue to assist the mole while removing this risk? Analysis suggested that some force could be transferred to the mole simply by preloading the scoop vertically onto the regolith surface immediately adjacent to it, thereby avoiding direct mole contact and removing the risk to the tether. There were also some indications that the portion of the mole below the bottom of the pit (~ 30 cm of mole) might now be experiencing more

friction, perhaps enough to allow it to dig freely. Recall that the mole back cap's along-mole distance to regolith surface when the SS was removed was ~ 7 cm, which would mean that the back cap was below the upper tier of friction springs. At the time it was argued that perhaps the mole slipped from a regime of penetration into a regime of rebounding when the back cap passed below this upper tier. With each tier providing a step-function change to resistance to mole upward motion, it was thought that the additional 5 cm of regolith contact might have put the mole back on the other side of the threshold. There were two key flaws in this analysis. First, the friction provided by 5 cm of additional regolith contact was significantly less than that of a friction spring tier (~ 30 N resisting upward motion per tier). Second, this interpretation assumed that the support structure remained in (more-or-less) close contact with the ground throughout sol 92. It was not appreciated at the time the degree to which the support structure had been lifted away from the regolith during the sol 92 hammering. The geometric analysis supporting significant SS 'ratcheting' up an already-rebounding mole (perhaps accompanied by some mole "climbing-up" the borehole wall) would not come until much later (see Sect. 6.2.1). The now-accepted interpretation is that the mole encountered sufficient resistance to begin rebounding while still being held with both tiers of friction springs. The upward force transferred to the SS through the springs was enough to lift the light support structure (7.4 N on Mars) away from the regolith; a transient state that was not captured since no IDC/ICC images were acquired during the first two hammering attempts.

As of this point it was still considered too complicated and too risky to attempt a direct push on the mole's back cap. Thus on sol 322, the arm was disengaged from its pinning position and pressed with a large overdrive into the regolith next to the mole. The scoop was positioned over the pit, which meant the force could only be transferred to the mole via the pit walls to the regolith beneath. An initial command of 50 strokes executed on sol 322. The resultant movie showed downward motion at the previous rate (compare Fig. 15) and raised hopes that the push was effective.

With an ambition that overreached our knowledge of the situation, the team commanded on sol 325 two periods of hammering (152 strokes each) separated by a re-application of the vertical preload on the regolith. This had very unfortunate results. Ambiguous motion was seen briefly at the beginning of the first hammering (sol 325a) and then gave way to a very rapid extraction of the mole. At an average rate of 1.0 mm/stroke, and a maximum rate of 3.2 mm/stroke, the mole withdrew from the regolith throughout the first phase of hammering. The back cap distance to the regolith increased from 1.5 cm to ~ 15 cm, accompanied by a tilt increase from 19° to 20° . Since there was no planned ground-in-the-loop step to recognize and react to this reversal, the reapplication of preload on the regolith occurred autonomously and the second hammering (325b) resulted in a further 3 cm of extraction, and an increase in tilt from 20° to 24° , see Fig. 8.

The story of the mole reversal rates and tilt changes during this reversal is unfortunately incomplete. A commanding error in IDC sequencing resulted in no images being taken during the latter half of either hammering phase, preventing any image analysis of mole heights during the second half of both hammerings. The end result of these reversal events was a mole that had a severe tilt of 24° and was roughly 18 cm out of the ground. The available images and the STATIL data suggest that the mole reversed its downward motion without much change in tilt but then tipped over and hit the pit wall when its center of gravity was just a few cm below the original surface. See Sect. 6.3 for a discussion of the causes of the high reversal rate and why it stopped half way through the second hammering period at 16.5 cm extraction thereby providing an estimate for the thickness of the duricrust.

5.6 Pinning 2

Subsequent to the mole reversal event, the IDA was retracted and used to image the mole and surroundings on sols 329 and 332. In the InSight testbed at JPL, the IDS team tested several other pinning techniques, hoping to find one less likely to knock the mole over. Only after examining each of them was it concluded that the existing technique used in sols 308–318 was still the least risky. Upon a careful approach to the mole with the scoop near the regolith (to reduce the lever arm to the center of mass and thus reduce the change of tipping the mole over) the mole was re-pinned horizontally on sol 339. On sol 342, vertical pinning motion of 1.5 cm was applied. Interestingly, the repining activities had almost no effect on the mole tilt.

On sol 346, 40 strokes were commanded that resulted in a few cm of downward motion accompanied by an increase in tilt from 24° to 26° . This tilt change motivated a vertical re-pinning on sol 349 consisting of 4 cm of commanded downward motion of the IDA scoop. This resulted in the scoop contacting the regolith and compressing the upper unconsolidated layer. The vertical motion was followed by 50 strokes that resulted in a rapid penetration of about 4 cm, ending the sol with a back cap distance-to-regolith of 14 cm and a further tilt increase to 27° . The IDA remained in this position for subsequent hammerings on sols 366 (19 str.), 373 (127 str.), and 380 (126 str.) which together resulted in further back cap distance-to-regolith reductions to 11 cm, 6 cm, and 3.5 cm, respectively. The tilt during these sols remained constant at 27° . The maximum rate of motion during this re-penetration (see Figs. 8 and 15) was ~ 0.6 mm/stroke occurring over sols 349 and 366. The hammerings on sols 373 and 380 had an average re-penetration rate of 0.3 mm/stroke. At the end of sol 380, the back cap of the mole was ~ 3.5 cm away from the original regolith surface. Even though still partially exposed, a TEM-A measurement was performed beginning on sol 380.

5.7 Reversal 2

IDA motions in Pinning 2 consisted of one horizontal motion (sol 339); augmented by vertical moves of 1.5 cm and 4 cm on sol 342 and 349, respectively. By sol 400, it had been 20 sols since the last hammering and 51 sols since the last application of any preload. It was feared that pre-load may have been dissipated during the previous hammerings. The concern was compounded by the scoop being in contact with the regolith since sol 349, since this may have prevented a strong scoop/mole force coupling. To re-establish preload, the IDA was commanded on sol 400 to retract vertically (commanded 1 cm up) and re-pin using a vertical-only motion (commanded 3 cm down). The upward motion did not bring the scoop out of contact with the regolith; rather, the motion was accommodated by the compliance in the arm links. By all expectations, this should still have retained the requisite preload to allow forward progress.

Unfortunately, this appeared to be insufficient to resist the mole's rebound characteristic at this depth when, on sol 407, 151 hammer strokes were commanded and resulted in a second mole reversal event. Close examination of the IDC movie reveals that at first it appeared that penetration was continuing: the depth changed by 1 cm in the downward direction in the first ~ 10 strokes, reaching a back cap distance-to-regolith of 2 cm. Downward motion stalled at this depth for about 20 strokes, then began to rapidly reverse at an average rate of 0.4 mm/stroke for the rest of the hammering session. The along-mole distance between the back cap and regolith increased from 2 cm to 7 cm, with tilt remaining roughly constant at 27.5° .

5.8 Regolith Interaction 2

During sols 414–420, the IDA was retracted and some further regolith interactions using the scoop were investigated. These consisted of a short scrape test and a further chop test. The chop test was specifically aimed at collapsing some of the pit walls, thereby increasing the amount of regolith in contact with the mole. This was somewhat successful, resulting in a small amount of duricrust being broken off the southerly wall of the pit on sol 420.

5.9 Back Cap Push – Horizontal Scoop

Throughout the anomaly since the SS lift, the team had considered multiple methods by which the IDA might assist the mole (Sorice et al. 2021). The reversal events reduced confidence that further attempts to hammer whilst pinning would be successful. Thus the pinning method was abandoned and the team transitioned to a long campaign (sols 427–557) of pushing directly on the mole's back cap with the scoop. This had the advantage of supplanting friction as the main source of resistance to rebound, placing the scoop in the path of the mole's rebound vector and directly mitigating the risk of reversal. However this delicate operation required much finer positioning than was typical for the IDA requirements and each placement was approached carefully so as to do no harm to the science tether, mole, or IDA. Since the IDA actuators could not directly follow the mole along its path into the regolith, each hammering period was followed by a repositioning of the scoop and a re-application of IDA preload. Initially this required ground-in-the-loop after each preload and hammer action, though in later stages the preload and hammer steps were combined as confidence in the methodology grew.

Though a long and arduous process (requiring 4.5 months to execute 9 back cap hammerings), it was successful: (1) the mole only moved down, the scoop providing resistance to rebound sufficient both to prevent reversals and allow the mole to progress, (2) the mole moved a total of 8 cm along its axis, ending this phase with the back cap ~ 1 cm below the original regolith surface (the maximum depth reachable by the flat scoop after the loose 1 cm surface layer had been compressed), and (3) the tilt increased only about 4 degrees from $\sim 27^\circ$ to $\sim 31^\circ$.

After the 6th of the 9 back cap hammerings, on sol 536, the mole's back cap was flush with the original (uncompacted) regolith surface.

During this and the subsequent Inclined Scoop phase, the right side of the back cap could not be seen by the IDC, thus preventing application of the glint technique described above for determining mole height. Instead, the team measured horizontal motion of the mole using the left side of the back cap relative to the ground (outside of any area churned during hammering). That distance was scaled based on known measurements (scoop slot and scoop width) and their apparent width in the image. Apparent progress in ICC images (scaled based on mole shaft width) were used to confirm that these IDC depth estimates were reasonable. Overall the technique provided a mole depth uncertainty of ± 1.0 cm and this is reflected in the error bars for the 'Mole Not Visible' points in Figs. 7 and 8.

5.10 Regolith Interaction 3

On sol 598, a full 12 cm scrape was performed to bring more material into the pit. This was fully successful and resulted in the mole being nearly completely covered.

5.11 Back Cap Push – Inclined Scoop

The horizontal scoop used during the previous back cap push campaign could not descend further than the level of the compressed unconsolidated layer, ~ 1 cm below the original regolith surface. By this time, the various scrape and chop actions had widened the pit to approximately one scoop width. This allowed the team to use an inclined scoop (30° from horizontal) to continue to preload the back cap using the scoop tip rather than its bottom edge. Three inclined back cap push activities were commanded on sols 618 (101 str.), 632 (101 str.), and 645 (252 str.).

These were successful in their execution, though they caused only a small increase in mole depth, with a combined 454 strokes resulting in only ~ 1 cm greater back cap descent. Though the mole could not be seen directly, the science tether could, and it had enough visible features to track mole progress (or lack thereof). Interestingly, the mole was observed to change orientation and tilt in an irregular fashion during these hammerings, with tilt fluctuating between 29.5° and 32° . The position of the science tether against the scoop was seen to migrate, and there was evidence of regolith pumping out of the pit adjacent to the mole's position.

The IDC movies revealed periods during these three hammerings where particles within the scoop did not move. This suggests some brief moments of 'Free Mole' hammering without IDA contact. Other images in the same hammerings showed substantial particle motion, suggesting that at those times the mole was attempting to reverse and was rebounding into the scoop. This recalls the observation of sol 407 where the mole made some downward progress, stalled, then reversed.

5.12 Regolith Interaction 4

The final actions to help the mole were focused on increasing regolith contact, and thus potential hull friction, as much as possible. The goal was to cover the mole with scrapes of regolith then use the arm to compact this material and pre-load the mole via the soil. Recall that something similar was attempted on sols 322 and 325 to aid the mole when it could no longer be safely pinned. In those previous actions the pit was empty and the force of the scoop on the surface was transferred to and dispersed in the competent duricrust layer. The desire now was to scrape regolith into the pit in several stages, tamping the pile after each one to compact and densify the material. It was hoped this would provide a more direct load path between the scoop and the mole.

From sol 659 to 700, three 12 cm scrapes were performed, bringing material from the far side of the pit into the pit itself. These were successful and resulted in a completely buried mole. A TEM-A measurement was included on sol 680 to take advantage of the pit fill to block solar insolation and remove direct exposure of sensors to the atmosphere. The measurement thus provided the first high-quality thermal conductivity data (compare Sect. 6.6). The scrapes provided piles of sand the angles of which are used in Sect. 6.4.2 to estimate the friction angle of the sand.

5.13 Final Free Mole Test

By this time, power and thermal considerations for InSight were complicating operations as dust continued to accumulate on the solar panels and Mars approached aphelion. The team had to consider the history of the mole's penetration rates, which were quite low (typically 0.1 mm/stroke and less from 31 cm depth on) in the context of the expected lifetime of

InSight. At what point could the mole make enough progress to be at an acceptable depth (3 meters) before the lander could no longer support its operation? Reaching the target depth would not be useful if the heat from hammering could not dissipate in time to make a clean measurement. TEM-A measurements and pre-landing analysis placed this necessary cooling time at around 100 sols. While it was not certain InSight could survive the thermal minimum of aphelion, if the mole could reach its target depth before this point it was reasoned that heat from hammering could dissipate during the aphelion lull and allow some good quality measurements of the thermal gradient when operations resumed.

For this plan to be successful, the low rate of penetration implied multiple days of continuous hammering to get the mole to an acceptable depth in time. Though it was hoped that the rate of penetration would increase at some depth, this could not be counted on. In order to make this constraint fit within the worsening power and thermal situation, it was decided amongst the team that after the scrapes and tamps of the previous period were completed, there would be one final Free Mole Test. In this test, the IDA scoop in a horizontal orientation would be maximally preloaded onto the regolith filling the pit above and around the mole. The mole would then be commanded to hammer 500 strokes, the high number being chosen such that the result, whatever it was, would be unambiguous.

Operational constraints and winter holidays pushed the final Free Mole Test to January 9th. Then, on sol 754, 500 strokes were performed. No further downward motion was detected by observing the science tether, although a substantial amount of lateral tether motion was observed. The mole tilt varied irregularly between 29.5° and 32°, some regolith poured out of the pit from below onto the surface next to the tether, and regolith particles on the IDA and in the scoop were seen to move erratically. This latter evidence suggests the mole was attempting to reverse and rebounding into the scoop, similar to what was seen during the back cap push activities with an inclined scoop. Thus it was determined that the final Free Mole Test was not successful and further attempts to assist the mole to achieve greater depth were abandoned.

A final IDA retraction and mosaic was performed on sol 775, and a TEM-A test with a fully buried mole was again performed on sol 795.

6 Soil Mechanical and Thermal Properties Derived from Actions and Measurements During the Mole Recovery Activities

In this section we will interpret the data collected during the 703 sols (22 months) of operating the mole and the IDA to support the mole on Mars. During the time the team had convinced itself of a model of a layered regolith at the site with a 1 cm thick dust layer above a duricrust of about 20 cm thickness. Underneath the duricrust, a ~ 10 cm thick sand layer is postulated to lie above gravel or sand with pebbles extending below 31 cm depth. This structure of the topmost layers of the regolith may be local (see Golombek et al. 2020a for a discussion of the geology of Homestead hollow) and the reader should be careful when drawing general conclusions on the martian regolith from our findings. We will discuss the dimensions and the fill of the pit to derive density and porosity ratios between the duricrust and the sand underneath the crust. We will further discuss the penetration rate and record to derive values for the penetration resistance and estimate the thickness of the duricrust. The results of scoop–soil interactions will be used to calculate the cohesion of the duricrust and the sand and estimate the internal friction angle for the latter. The estimate of the cohesion of the duricrust value will be compared with a value derived from the penetration resistance. The thermal measurements with the HP³ radiometer and the TEM-A hardware have been

used to estimate the thermal conductivity and the density up to 40 cm depth. Seismic velocities, elastic moduli and the Poisson's ratio have been determined using the hammering recordings with the seismometer SEIS. In the following Sect. 7 we will combine the results in a synopsis summarizing our model of the top 40 cm of the martian soil at the site of the HP³ mole pit.

6.1 Pit Formation and Soil Porosity

We begin by discussing the formation of the pit during the first two hammerings on Sols 92 and 94 (compare Table 2 and Fig. 7) and its depth. The pit has been described in Sect. 5.3 and is shown in Figs. 9 through 11. It is about 2 mole diameters (63 ± 3 mm) wide and 20 ± 1 mm on average deep with a maximum depth of 72 mm. Its dimensions and shape and the position of the mole in the pit pointing towards a southwesterly direction at a tilt of $20 \pm 1^\circ$ suggest that it has been carved by the mole through a precession-like movement about a point roughly midway on its vertical axis. We have attempted to follow the mole movement by tracking the path of its tip and of its top end in Fig. 12. Unfortunately, the STATIL data are ambiguous with respect to mole tip movement and mole rotation. The top panel shows the angular distance in degrees that the mole tip would have moved if the STATIL readings could all be interpreted as tip movement. Accordingly, the tip moved first in a southerly direction during the first 78 strokes before turning west and possibly back. The light blue and, in particular, the orange dots after stroke 415, may include or completely represent a rotation of the mole about its axis which is consistent with the position and tilt of the mole in the pit and the observed twist of the science tether. In the bottom panel we map the motion of the mole top by using characteristic markings on the imprint in the sand of the support structure feet. The lower apex of the triangles mark the midpoint of the back cap as known from the dimensions of the support structure. The blue triangle indicates the first position after deployment followed by the red and the yellow triangle. Accordingly, the top end moved northeast first and then turned east. Taken together these data support an almost half circle precession movement of the mole.

Some early explanations of the formation of the pit suggested that the original fill was drained to hollows existing at depth before the pit was formed. Images of the pit wall suggest that there may be hollows in the duricrust but there is no way to prove or disprove their existence. An alternative proposal is based on the high porosity of the soil derived from the TEM-A data, which suggest a bulk density of 1211_{-113}^{+149} kg/m³ and a bulk porosity of $63_{-4}^{+9}\%$ (Grott et al. 2021). Note that this density has been determined after the pit was filled with sand and encompasses ~ 40 cm of regolith containing duricrust, sand compacted by hammering, sand fill, and sand with gravel and/or pebbles. Assuming that the mole upon penetrating destroyed the fabric of the duricrust and reduced the porosity of the material, it is proposed that the pit formed as a consequence of the mole grinding duricrust to sand. The volume of the pit as reported in Sect. 5.3 of 5.4 to 6.7×10^4 mm³ would then equal the difference of the volume of the duricrust worked by the mole and the volume of resulting sand after accounting for the volume of the mole. To test this hypotheses we consider a cylinder of the surface radius of the pit r_{pit} with a height of the thickness of the duricrust d_0 . (For simplicity, we neglect any effects on the volumes due to a tilt between the mole axis and that of the cylinder.) Conserving mass, the ratio between the (uncompacted) densities of the sand ρ_s and of the duricrust ρ_0 can be calculated from

$$\frac{\rho_s}{\rho_0} = \frac{1}{1 - \frac{d_{pit}}{d_0} - \left(\frac{r_m}{r_{pit}}\right)^2} \quad (2)$$

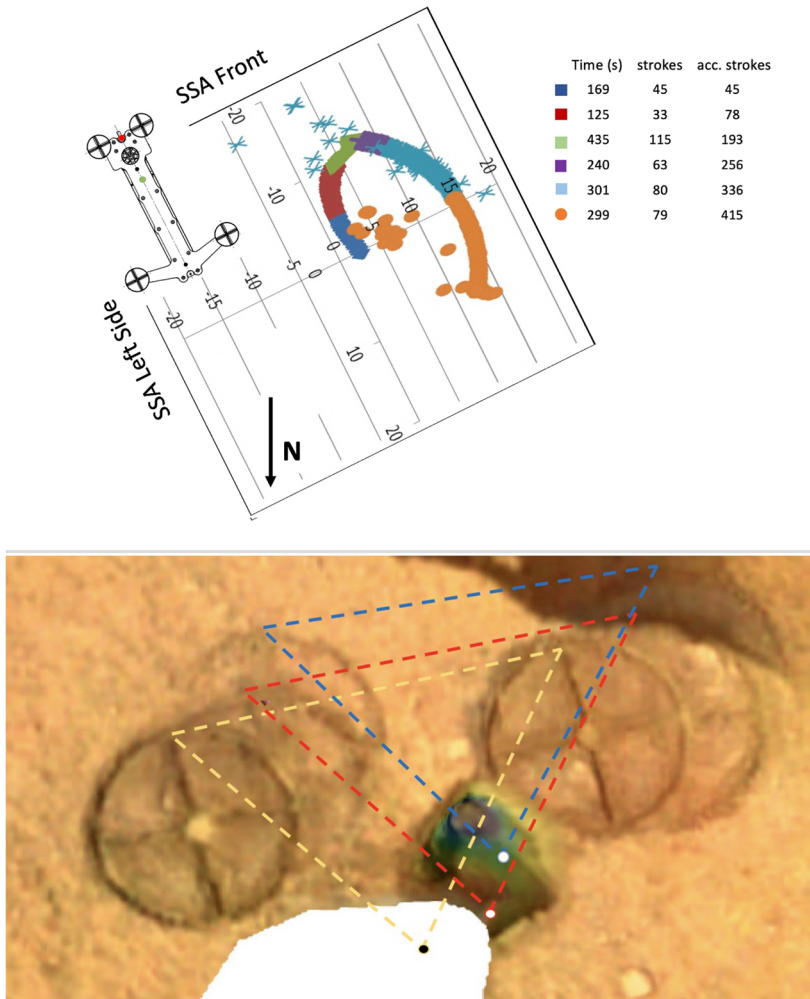


Fig. 12 Top: Reading of the x-y sensors of STATIL during the first 325 hammer strokes on Sol 92 in degrees. The recordings are ambiguous with respect to rotation of the mole and x-y motion of the tip. The recordings are consistent, however, with a south and west movement of the tip and followed by a northward rotation of the mole as suggested by the position and the attitude of the mole and the twisted orientation of the tether in images taken at Sol 230. Bottom: Reconstructed path of the back-cap from the footprints of the feet using the known dimensions of the support structure. While STATIL data indicate a movement of the tip southward and then westward, the back-cap moved northeastward and then eastward

where d_{pit} is the average depth of the pit. The second term in the denominator on the RHS represents the volume of the pit relative to the volume of the cylinder while the third term accounts for the mole volume. Fitting the mole in the cylinder requires ρ_s/ρ_0 to be 1.2 to 1.25 in which case the pit would be filled ($d_{pit} = 0$). For a duricrust extending down to 31 cm depth and a pit depth as observed, ρ_s/ρ_0 would have to be 1.25 to 1.35. And with a duricrust of 20 cm, the range would extend to 1.4. Assuming as another extreme case that the mole was fully accommodated by compressing the sand, the ratio between the density of the uncompacted sand and the duricrust would be about 1.1. Morgan et al. (2018) give a

representative value for martian sand of 1300–1350 kg/m³ but values of up to 1500 kg/m³ have been reported (Herkenhoff et al. 2008). Considering a regolith bulk density of around 1200 kg/m³, a density of the duricrust of around 1100 kg/m³ would be a reasonable estimate, but it could be as low as 950 kg/m³. With a grain density of 3200 kg/m³ (typical of basalt), the above density ratio suggests a ratio of porosities of 1.1, or a reduction of the bulk porosity from the duricrust to sand by about 10%.

6.2 Rate of Mole Penetration and Soil Penetration Resistance

6.2.1 Observed Rates of Penetration

The rate of penetration of the mole has varied markedly over the limited depth reached (compare Figs. 7 and 8). Unfortunately, the accuracy of the estimates of the tip depth is limited since the TLM was designed to engage only after the mole tip reached a depth of 54 cm as discussed in Sects. 2.1 and 5.1.

In Fig. 15 we present four sets of data taken on specific sols for which the data are of particular interest. The first is from sol 92 for which we have (albeit very limited) penetration data for the duricrust with a good coverage of tilt changes. For sols 308–320 (pinning 1) reasonable penetration data from tracking the glint on the back cap are available allowing an estimate of the penetration resistance below 31 cm depth while the change in tilt is small. This also applies to sols 458–536, a part of the back cap push phase in which the back cap was still visible. The data for sols 346–380 (pinning 2) allow an estimate of the resistance to (re)penetration, most likely of the sand below the duricrust to a depth of 31 cm.

For the initial penetration rate on Sol 92, the available constraints are (1) the time the mole back cap passed the contact switch, (2) the STATIL tilt data, and (3) the internal geometry of the SS. The back cap passed the contact switch after 77 hammer strokes (~293 seconds). The switch is located in the tube such that when the back cap of the 40 cm mole passes it, 17.8 cm of the mole is below the bottom of the tube, and 14.8 cm of the mole is below the SS feet. Had the mole been oriented vertically, we would conclude that ~15 cm of the mole had penetrated into the regolith. The STATIL data, however, tell a very different story.

During the first 400 strokes the mole tilt changed rapidly (compare Figs. 13 and 15). Initial tilt reported by STATIL was ~4°, about two degrees less vertical than the local ground slope of ~2°. Within the first minute (~16 strokes), the initial tilt reduced to 2.5°, then began to rise again, plateauing at ~14° after about 11 minutes (~stroke 170). A slight break in the time-varying tilt curve around 4.8 minutes (stroke 77) is consistent with the moment of contact switch passage. Further STATIL data from this interval and sol 94 are well recorded, but unfortunately provide no further constraints on mole motion without significant assumptions.

Limiting the discussion to just the moment of contact switch passage, STATIL reported a mole tilt of 11°, implying 9 to 13° of mole tilt with respect to the SS vertical tube, more likely 13° as the STATIL data suggest that the mole tip moved roughly in the direction of the ground slope. However, the vertical tube of the SS cannot accommodate such a large relative mole tilt when the back cap is level with the contact switch; rather the maximum allowable mole-vs-SS tilt is only 5°, assuming a full compression of the friction springs. To resolve this geometric conundrum, we invoke the following: (1) The SS is very light weighing only 7.4 N on Mars, which is less than the rebound resistance provided by the SS friction springs. (2) The SS moved at a time or times unknown during the sols 92 and 94 hammerings, as revealed by the footprint markings in the upper soil layer in e.g., Fig. 12. (3) The front

Fig. 13 Statil recording of the first 500 strokes on sol 92. Marked are the mole passage of the contact switch as sensed by STATIL and the stroke when the mole tip suddenly changed direction from mostly southward to mostly northward (compare Fig. 12). Note that because of the ambiguity in the STATIL data the inferred change in direction of tip movement may also be a sudden change in sense of rotation. Also note the wavy character of the increase in tilt angle after stroke 200

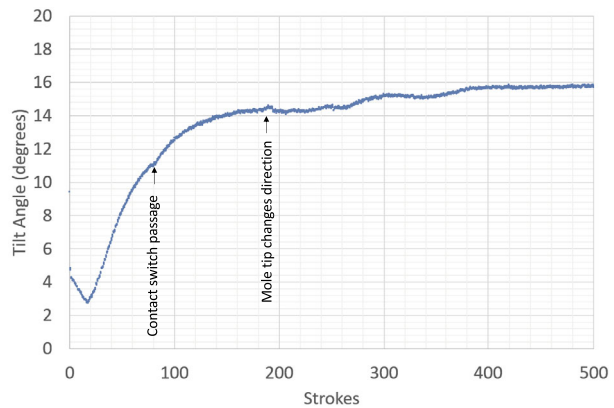
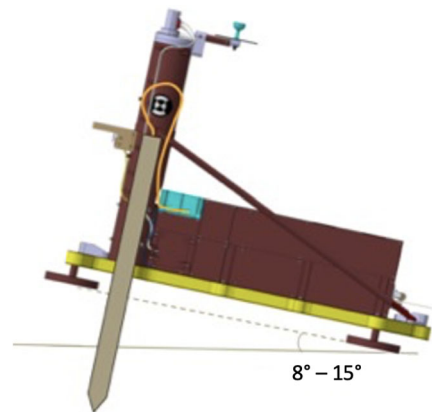


Fig. 14 Illustration of the support structure lift and rotation about an axis through its back feet as suggested by the interpretation of the STATIL data recorded on sol 92 and discussed in Sect. 6.2.1



footprint impressions show little to no scuffing, especially after sol 94 where the internal cross-beams of the feet have left clear markings in the soil. This suggests the SS was lifted away from the regolith and then replaced in a new position, rather than just being dragged or pushed horizontally. (4) The SS was seen to jump or jostle about during the Diagnostic Hammerings on sol 118 and 158. And finally (5) as revealed when the SS was lifted away, the mole azimuth had its tip pointing towards the southwest, meaning the rebound vector pointed northeast. The SS motions of y-axis translation and aft-right-foot rotation, seen after the first and second hammering intervals, respectively, are roughly consistent with the mole pushing against the SS during mole rebound. Thus we conclude that the mole rebound acted to lift the front feet of the light support structure away from the soil at some time or times during sol 92 (and possibly also sol 94). Unfortunately, mid-hammering movies were not captured during the 4 hr hammering interval, and there is no tilt data for the SS itself.

Using the STATIL reported tilt of the mole (11°), the length of the mole and position of the contact switch in the SS, the maximum allowable mole-vs-SS tilt (5°), and the local ground slope (2°), we can bound the geometry of the system at the moment of contact switch passage. The smallest possible lift that is consistent with all the data implies an SS tilted up by 8° relative to the ground around a pivot point at the back of the aft feet (see Fig. 14). The mole, extending 14.8 cm below the bottom of the SS feet, would then have a tip depth of ~ 9 cm. The largest possible SS lift implies an SS tilted up by 15° relative to the

ground around the same pivot. The mole, extending the same 14.8 cm below the bottom of the SS feet, would then have a tip depth of ~ 4 cm. These then place limits on the average penetration rate for the first 77 strokes of 0.5–1.2 mm/stroke.

The change of mole tilt during the same time by ~ 0.13 degrees/stroke required additional displacement of soil. We can estimate the average rate of volume displacement due to forward penetration and mole tilting. For the forward penetration, we find for the tip reaching 9 cm depth a volume displacement rate of $\pi r_m^2 \times 1.2$ mm/stroke or about 0.7 cm³/stroke. For 4 cm depth, we get about 0.3 cm³/stroke. For the average volume displacement rate for mole tilting, we take half of the along mole cross-section area of the mole corrected for the tip height of 3 cm, which amounts to about 3.5 cm² for the 4 cm tip depth and 10 cm² for the 9 cm tip depth. These values need to be multiplied – assuming constant rates of tilt increase as the STATIL data suggest – by the average length of mole out of the support structure when passing the contact switch minus half of the tip depth reached, and by the rate of tilt change in arc sec per stroke. Doing so, we get a volume displacement rate of about 0.14 cm³/stroke for the 4 cm tip depth and 0.33 cm³/stroke for 9 cm tip depth, or a little less than half of the average volume displacement rates for downward penetration. Taken together, the average volumetric penetration rate during the first 77 strokes in the topmost layers of the duricrust is between 0.45 and 1 cm³/stroke. At that rate, the pit as discussed in Sect. 6.1 would have been formed by the first 400 to 800 strokes, that is well within the hammering on sol 92. The mole may have reached the tip depth of 31 cm during that time. By the end of each multi-hour session on sols 92 and 94, the SS had settled back to the surface. With the back cap necessarily below the contact switch and all four SS feet on the ground (confirmed by post-hammering images on sol 92), the mole tip was therefore deeper than ~ 15 cm at the end of sol 92.

Better time- and depth-resolved estimates of the penetration rates are available after Sol 308 where IDC images could be used to compute the height of the back-cap above ground. The error of the depth determination from imaging data is estimated to be ± 0.5 cm for cases where the glint feature on the back cap was visible, and ± 1.0 cm for cases where the scoop fully or partially blocked the view of the back cap. Considering only the downward motion of the mole reported by stroke in Fig. 15, the average rate of penetration from sol 311 to sol 322 was 0.11 mm/stroke, with little change in tilt. Faster rates were observed during recovery from Reversal 1, with a maximum ‘re-penetration’ rate of 0.9 mm/stroke during sols 349, 366, and the beginning of 373. The later portion of sol 373 and sol 380 averaged ~ 0.3 mm/stroke. Likewise, recovery from Reversal 2 was initially rapid (~ 0.6 mm/stroke on sol 458) but quickly decreased to an average rate of ~ 0.13 mm/stroke over sols 472–536, again with little change in tilt. All subsequent penetration was < 0.1 mm/stroke with very low penetration rates of < 0.05 mm/stroke from Sol 543 on. On Sols 557 and 754, the mole did not penetrate at all.

6.2.2 Comparison with Test Data and Models – Soil Penetration Resistance

Laboratory tests of the mole (Wippermann et al. 2020) in cohesionless quartz-sand (WF 34) and mildly cohesive, high friction angle sands (Syar, MSS-D) at DLR Bremen and at JPL in Pasadena have measured significantly higher penetration rates than on Mars at similarly shallow depths (compare Tables 3 and 4). The term “Syar” was used by the team as a shorthand for a commercially available crushed basalt sand.¹ Syar sand has sharpened-edged grains

¹“Syar Industries” is the trademarked name of a building material supply company in northern California. Crushed basalt from the Lake Herman Volcanics Group was procured by the InSight project from Syar In-

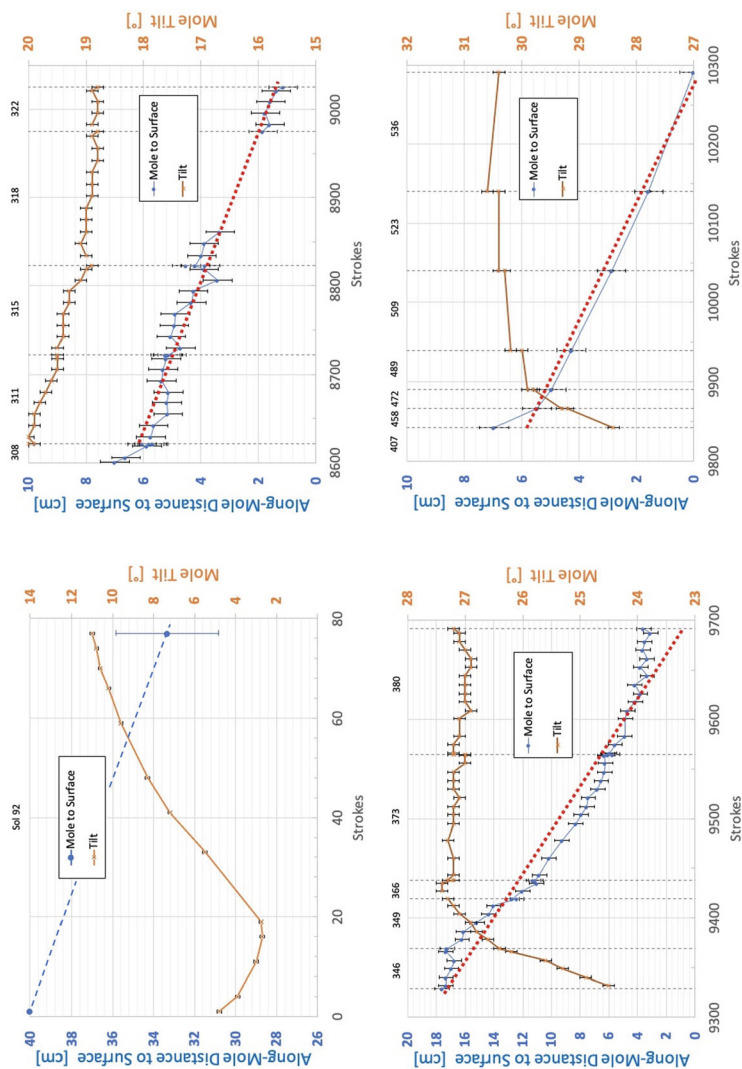


Fig. 15 Data used to estimate the penetration resistances of the layers the mole penetrated or attempted to penetrate. Plotted are the “Along-Mole Distances to the Surface” in centimeters and the “Mole Tilt” in degrees as functions of the cumulative number of strokes at the sols indicated. The top left panel shows the estimate of the along-mole distance after 77 strokes on sol 92 at the time of the back-cap passing the contact switch in the SSA (compare text) and the evolution of the tilt from 4° to 11°. The top-right panel shows the progress of the mole by 5 cm between sols 308 and 322 and the change of the tilt by about 1°. The bottom left panel gives the data for the re-penetration after mole extraction during sols 346–380. The bottom right panel shows the penetration by about 6 cm during sols 458–536 accompanied by an initial increase in tilt by about 2° keeping mostly steady thereafter

Table 3 Comparison of penetration rates at depths between 300 and 720 mm in the Deep Penetration Tests with Syar sand and with quartz-sand WF 34 described in more detail in Wippermann et al. (2020). Most readings were taken at 400 mm tip depth. The mole models listed are the Preliminary Proto Flight Model PPFM, three Proto Flight Equivalent Models PFE-1 through -3, and the Qualification Model QM. Some models differ in their stroke energy but the rates have been adjusted for a stroke energy of 0.7 J. The measured penetration rates vary by a factor of about 2 but even the penetration rate in Syar sand is about an order of magnitude higher than estimated for a similar depth of 310 mm on Mars. For DPT-2 and DPT-3 with PFE-1 penetration resistances of the sand were measured before and after the tests using a commercial hydraulic cone penetrometer HYSO 100 kN – LW of the manufacturer A.P. van den Berg. At the depth of interest here, the resistance values did not change much between pre- and post-test recordings

Simulant	Mole model	Stroke energy (J)	Test ID	Tip depth (mm)	Penetration rate (mm/stroke)	Penetration resistance (kPa)
Syar	PPFM	0.85	DPT 4	400	1.34	
Quartz sand	PPFM	0.85	DPT 1	300	2.03	
WF 34	PPFM	0.70	DPT 6	300	2.33	
	PFE-1	0.85	DPT 1	400	1.73	
	PFE-1	0.85	DPT 2	400	3.67	200
	PFE-1	0.85	DPT 3	400	2.65	250
	PFE-1	0.85	DPT 4	400	2.92	
	PFE-2	0.70	DPT 1	400	2.37	
	PFE-2	0.70	DPT 2	630	2.91	
	PFE-3	0.70	DPT 1	720	2.10	
	QM	0.70	DPT 1	650	2.56	

Table 4 Comparison of the change of penetration rate through the first 30 cm observed in laboratory experiments and on Mars. N_{St} is the number of hammer strokes to reach 30 cm tip depth. R_0 is the penetration rate at the surface and R_{30} the rate at 30 cm tip depth. The fourth column gives the ratio between the two rates. The penetration rate on Mars decreased at least as much as in compacted sands or more. The number of hammer strokes needed to reach 30 cm depth on Mars is not known, unfortunately

Simulant	N_{St}	R_0 (mm/stroke)	R_{30} (mm/stroke)	R_0/R_{30}
Syar (with stones)	31	4.839	1.183	4.1
MSS-D	14	10.71	1.408	7.6
MSS-D (with stones)	23	6.521	3.877	1.6
MSS-D (compacted)	64	2.312	0.469	4.9
MSS-D (compacted with stones)	57	2.632	0.618	4.2
Mars	–	0.5–1.2	0.11	5–12

with sizes ranging up to 100 μm . A mix of 80 weight-% sand and 20 weight-% Syar dust was used at DLR. Wippermann et al. (2020) list a friction angle for the Syar mix used of 54.8° (see also Spohn et al. 2022). MSS-D is Mars Simulant Sand-D. Mechanical properties of MSS-D have been described in Delage et al. (2017) and are listed in Spohn et al. (2022) who give a friction angle for MSS-D of 37°.

We list in Table 3 the penetration rates that were recorded for the smallest tip depths during the tests. Because the gravity on Earth is roughly three times higher than on Mars,

dustries as a bulk regolith simulant. The term ‘Syar’ was used by the team to distinguish this simulant from other basaltic materials used in testing.

the soil overburden pressure was proportionally higher in the terrestrial laboratory. Some data are available for the decrease of the penetration rate through the first 30 cm (Table 4) in Syar and MSS-D sands. With the exception of a test in pure MSS-D sand (second line from the top in Table 4), the ratios are smaller than the minimum estimate of the decrease of the penetration rate on Mars. The latter test stands out because of a high initial penetration rate, R_0 .

Many models have been published aiming at predicting the rate of penetration of penetrometers in sand. These include analytical theories such as e.g., Rahim et al. (2004) and Salgado and Prezzi (2007) based on the cavity expansion theory of Salgado et al. (1997) as well as numerical models based on e.g., Dynamic Cone Penetration Theory (Poganski et al. 2017) and Discrete Element Modeling (e.g., Lichtenheldt and Krömer 2016; Zhang et al. 2019). In general, they find the penetration resistance σ_p for a penetrator of a given stroke energy E to be inversely proportional to the penetration rate

$$AR \cdot \sigma_p = \epsilon E \quad (3)$$

where A is the cross-section area of the penetrator, R the penetration rate, ϵ is the efficiency of the mole converting its stroke energy E into deformation energy. AR is the volume displacement rate of the penetrator. The stroke energy of the mole flight model is known to be 0.7 J and its cross-section area can be calculated from its radius of 1.35 cm. Accordingly,

$$R \cdot \sigma_p \approx \epsilon \times 1.22 \text{ kPa} \cdot \text{m/stroke}. \quad (4)$$

Some pre-flight mole models had a higher stroke energy of 0.85 J. The penetration rates given in Table 3 have been corrected for the difference and referenced to a stroke energy of 0.7 J.

The efficiency of energy conversion ϵ is more difficult to estimate and the result is more uncertain. Rahim et al. (2004) use 0.75 while Zhang et al. (2019) find 0.5 as a typical value. The efficiency of the hammer mechanism converting spring energy to kinetic energy of the penetrator depends on the ratio between the hammer and the suppressor mass (compare Fig. 1), the spring constants, and the coefficient of restitution of the metals used (Spohn et al. 2022). For the HP³ mole and a coefficient of restitution of 0.8–0.9, the efficiency is 0.53–0.59. We estimate the efficiency of penetration in sand using our laboratory data published in Wippermann et al. (2020). The penetration resistance of the sand was measured before and after the tests with a commercial penetrometer and compared with the penetration rate during two of the laboratory tests in quartz-sand with the Proto Flight Equivalent Model PFE 1 (compare Table 3). These data allow an estimate of ϵ at least for these tests, since Zhang et al. (2019) find the static resistance (the resistance to a slowly penetrating penetrometer) to be very close to the dynamic resistance for penetration resistances smaller than 10 MPa. By comparing the penetration rates with the penetration resistances up to 3 m tip depth, we find $\epsilon = 0.47 \pm 0.05$. It should be noted, however, that in both tests the penetration rates at depths > 3 m decreased substantially although the measured penetration resistance did not increase accordingly. The reason for the decrease in penetration rates for quartz-sand and the difference to the test with Syar sand has been explained by Wippermann et al. (2020) as being due to the effects of friction on the tether.

With the penetration efficiency from the laboratory experiments in quartz-sand, we estimate the penetration resistance of the soil from the four subsets of data plotted in Fig. 15. For the topmost layers of the duricrust we use the volumetric penetration rate estimated in the previous section to imply a penetration resistance of 0.35–0.70 MPa. For the penetration resistance of the layers below 31 cm depth we use the slopes of the fitting line for the

data from sols 308 to 322 of 0.11 mm/stroke and from sols 458 to 543 of 0.13 mm/stroke. For these, changes in mole tilt are small and penetration rate estimates rather reliable. From Eq. (3) we get a penetration resistance of 4.9 ± 0.4 MPa. This value is likely to increase with further depth as the penetration rate kept decreasing as the mole got deeper. For the (re)penetration during sols 346 to 380 through the sand layer underneath the duricrust we use a fit with a slope of 0.7 mm/stroke and find 0.83 MPa for the resistance, a value that is by a factor of 1.2 to 2.4 larger than the above estimates for the duricrust.

Zhang et al. (2019), citing evidence from Discrete Element Modeling as well as from field measurements, report that the penetration resistance increases with the square of the relative density and linearly with overburden pressure. Rahim et al. (2004) find the penetration resistance to depend on initial porosity and internal friction angle of the granular material while cohesion was found to be of smaller importance. For small internal friction angles of 20° or less, the dependence on initial porosity is small with resistance increasing by a few percent when porosity is decreased from e.g., 0.6 to 0.3. Resistance will increase by a factor of 5.5, though, in that same porosity range for a friction angle of 40° . Data collected by Golombek et al. (2008) and Herkenhoff et al. (2008) show that martian soils have friction angles between 30° and 40° with dust having friction angles as low as 20° .

While we consider overburden pressure of limited importance at 10s of cm depth, the dependence on the relative density may offer an explanation for the resistance to (re)penetration of the sand layer as compared with the resistance of the duricrust. Taking the square root of the ratio between the resistances gives relative density values of 1.1 to 1.4 consistent with our estimates of the densities of the sand and the duricrust in Sect. 6.1, especially if the sand is assumed to be compacted upon penetration and by the previous hammerings.

Increase in relative density cannot easily explain the increase in resistance at 31 cm depth, though. Here, the relative density would have to increase by a factor of more than 2. It is possible, if not likely, that the soil at that depth was further compacted during the first 8600 strokes hammered during Sols 92 and 94. Vibration generated by the hammer strokes could also have been a factor in compacting the soil. It should be noted, however, that the seismic energy in the hammer signals recorded by SEIS during hammering is less than a percent of the stroke energy when geometrically projected to the mole tip as the source area (compare Sect. 6.5.4 below). Penetration models usually find a compacted region in front of the penetrator with a thickness of a few times the radius of the penetrator. The mole penetrated roughly 7.5 radii aided by the robotic arm beneath the depth of interest without an increase in the rate having been observed. On the contrary, the rate decreased further, from 0.6 mm/stroke for 20 strokes on Sol 308 to 0.06–0.15 mm/stroke between Sols 311–322 and less than 0.05 mm/stroke from Sol 543 on.

A simple explanation for the low penetration rate beneath 31 cm tip depth is that the mole had entered into an intrinsically more resistant layer than sand that got more resistant with depth, e.g. a layer of gravel or a layer of small stones embedded in sand. An early test with a breadboard model (the MM-mole model) has been reported in Wippermann et al. (2020). That mole penetrated a mono-layer of Columbia river basalt stones of 5–15 cm size. The rate estimated from the data was about 0.03 mm/stroke but that mole had a smaller spring energy than the flight model. The TEM-A thermal conductivity measurements (Grott et al. 2021), do not show any evidence for layering or an increase of conductivity with depth as might be expected if an highly compacted sand region extended from 30 to 37 cm depth. A layer of gravel or small rocks is thought to be consistent with the data, though, (compare Sect. 6.6) and could have a density of 1600 kg/m^3 . The gravel rich material could be rocky ejecta from a crater (e.g., Warner et al. 2020).

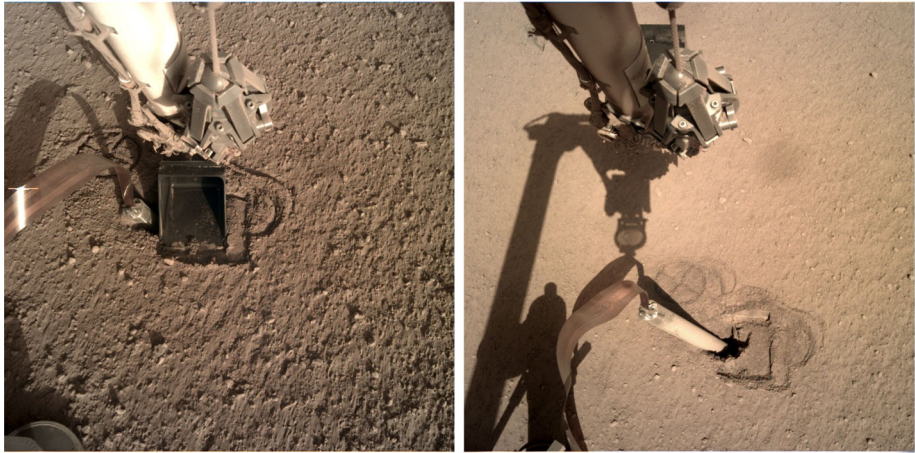


Fig. 16 Configuration of the scoop during regolith push. The left panel shows the scoop pressed onto the surface next to the mole for the intended regolith push on Sol 322. The right panel shows the mole pit, the backed-out mole and the scoop indentation after lifting the scoop on Sol 333

6.3 Estimate the Thickness of the Duricrust from Mole Backing Out on Sol 325 After Regolith Push

As we have reported in Sect. 5.5, the mole backed out of the ground by a total of 17.4 cm on sol 325. Not being able to pin the mole any further, the scoop had been pressed onto the surface next to the mole to provide vertical stress that would increase friction on the mole hull. The vertical force of the scoop was estimated to be 46 N, equivalent to a vertical stress immediately underneath the 7.6×10.6 cm scoop of 5.7 kPa. Stress propagation in an elastic half space suggests that this stress is concentrated underneath the load but decreases to about one tenth at a depth of two scoop widths. The scoop was thus placed above the mole (Fig. 16) although part of the scoop would then be above the pit through which vertical stress could not be transferred. Without much evidence on the thickness and the stiffness of the duricrust at the time, it was not clear how well stress could be transferred to the mole hull. Simple calculations for an elastic half-space suggested that the necessary friction could be provided.

The mole backed out right from the beginning of the first 150 strokes set on sol 325 at an average rate of -0.9 mm/stroke. All in all, the mole had moved a total of 17.4 cm, from 1.1 cm to 18.5 cm along mole distance. During the time, the mole tilt changed little during most of the upward motion. When the mole had almost reached its maximum back out it made a small tipping motion, increasing the tilt from 20° – 24° (Fig. 8).

The mole reversing its direction of motion has been observed in the laboratory at martian atmosphere pressure in high-friction-angle sand such as Syar. A proposal to explain the backward motion assumes that the mole is embedded in sand underneath the duricrust and in sand that has accumulated by its penetration through duricrust as described in Sect. 6.1. When the mole bounces in place, sand having been compacted by the mole penetration may relax and flow in front of the tip during an upward motion thus raising the floor underneath the bouncing mole. The rate of accumulation of sand would be about equal to the rate of upward motion ignoring some (re)compaction of sand when the mole falls back onto the sand. With an average upward motion of about 1 mm/stroke, a millimeter of sand would have

to fill in underneath the mole per stroke. The mole would have stopped its upward motion when its tip reached the bottom of the duricrust when the lateral flow of sand stopped. If this simple model is correct, then the distance of the upward motion provides an estimate of the thickness of the duricrust. From the length of the mole out of the ground of 18.5 cm, its total length of 40 cm and the tip angle of 27° , we get an estimate of the thickness of the duricrust of 19.2 cm.

6.4 Soil Mechanical Parameters Derived from Scoop – Soil Interactions

6.4.1 Cohesion Estimate from Regolith Interaction 1

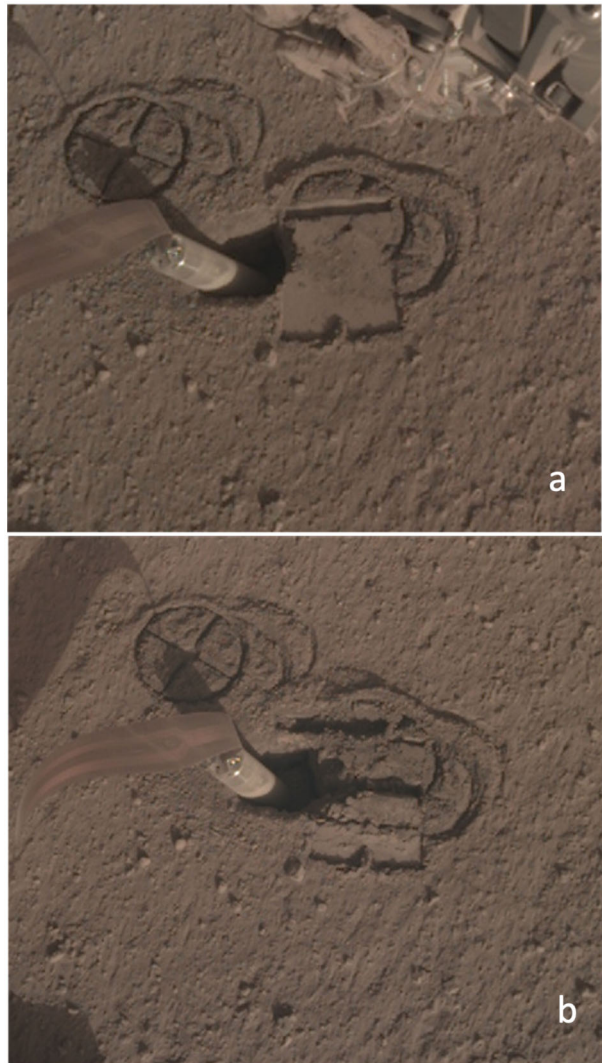
The pit that formed around the HP³ mole offers a unique opportunity to combine slope stability analysis with measurements of IDA forces at the scoop and images to estimate the mechanical properties of the martian soil. The stability of the pit is examined with a three-dimensional Finite Element Method (FEM) calculation using the PLAXIS 3D program. In considering the problem of slope stability, we assume that the material is homogeneous and that a Mohr-Coulomb failure criterium is satisfied along the failure plane, i.e., that the regolith shear strength τ is defined by: $\tau = c + \sigma \tan \phi$, where σ is the normal stress on the potential failure plane, ϕ is the internal friction angle, and c is the cohesion.

As outlined in Sect. 5.3, on Sol 240, the flat part of the IDA scoop was used to apply a preload at the edge of the HP³ mole pit in an attempt to cause failure of the western wall. The IDA algorithm used to compute the force at the end-effector (Trebi-Ollennu et al. 2018) determined that the force applied by the scoop was $F_z = 29$ N in the vertical direction and $F_r = 15$ N in the radial direction. Interestingly, this ratio corresponds to a friction angle of about 30° , showing that the scoop is not far from sliding along the regolith surface, with sliding probably impeded by a notch at the bottom of the scoop. Such force did not cause slope failure (Fig. 17a). It is worth noting that, without a slope failure, the slope stability analysis provides a lower bound estimate of the cohesion. The force F_r , which acts away from the lander, does not affect the stability and only the vertical force F_z is considered in the analysis.

The topographic map of the HP³ pit presented in Fig. 9 is used to measure the slope inclination angle $\beta = 85^\circ$, height $h = 0.07$ m, and width $w = 0.045$ m. Minimum estimates of the cohesion are calculated for a presumed internal friction angle ϕ of 30° and a bulk density ρ of 1200 kg/m^3 . The results indicate that a minimum cohesion c of 0.4 kPa is required for the slope to be marginally stable when a force F_z of 29 N is applied by the flat part of the IDA scoop.

Subsequently, on Sol 250, the tip of the scoop was pushed into the soil near the HP³ mole pit. The force applied by the tip of the scoop was $F_z = 45$ N. The IDA interaction with the surface resulted in the failure of a soil wedge (Fig. 17b). High-fidelity Digital Elevation Models obtained using Structure-from-Motion (SfM) computation (Garvin et al. 2019) provided information on the geometry of the failure wedge, i.e., a failure angle of 35° and a height of 0.013 m. If we use this finding in conjunction with the slope stability model, and take into account the lower bound estimate of the cohesion obtained from the flat push on Sol 240, we obtain a cohesion c of 5.8 kPa for a value of the internal friction angle ϕ of 30° and bulk density ρ of 1200 kg/m^3 . The effect of uncertainty in the model input parameters was explored using a sensitivity analysis. Results show that the cross-sectional area on which the force is applied has the most effect on the cohesion value, while variations in internal friction angle, slope height, soil bulk density and vertical force applied do not greatly influence the cohesion estimate.

Fig. 17 Images of IDA scoop interactions with the surface material near the HP³ mole pit. (a) After a flat push on Sol 240. (b) After a tip push on Sol 250



These cohesion values are consistent with a steep-sided open pit, the wall slopes created by the IDA scrapes, and are similar to relatively strong, blocky, indurated soil at Viking Lander 2 (Moore et al. 1987).

6.4.2 Scrape Angles from Regolith Interaction 4

On sol 673, two overlapping 12 cm long scrapes were commanded to bring regolith from the far side of the pit into the pit. The scrapes created two piles close to the mole, referred to P1 and P2 in Fig. 18a, and walls parallel to the direction of the scoop's scrapes, denoted by W1 and W2 in Fig. 18a. As a result of the IDA scraping actions, the piles P1 and P2 are created by bulldozing mounds of grains over the relatively flat ground surface. It is worth noting that mounds obtained by scraping typically yield different geometries and properties than piles formed by pouring the material from a given height, from which the angle of

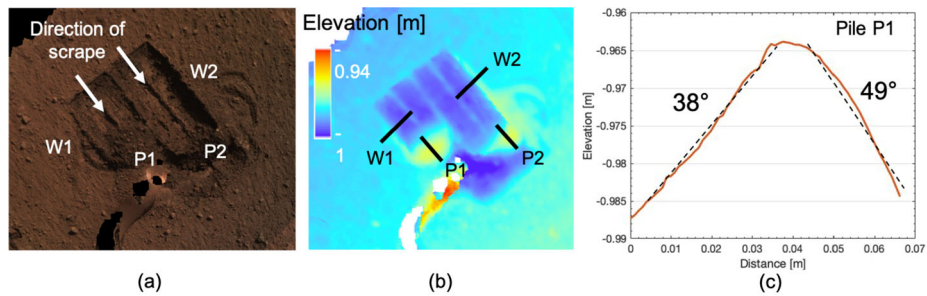


Fig. 18 Digital elevation model of the pit based on the stereo pair taken on sol 673 after IDA scraping. (a) Orthoimage showing the piles P1 and P2 and walls W1 and W2 left after the scoop scraped the regolith. (b) Digital elevation model (c) Elevation profile for pile P1

repose is typically measured (Beakawi Al-Hashemi and Baghabra Al-Amoudi 2018; Chik and Vallejo 2005; ASTM C1444-00 2000). The scoop scraping action disturbs the regolith and likely breaks the cohesive bonds between the grains.

Elevation profiles are extracted from the sol 673 digital elevation model (Fig. 18b) to measure the slopes of the piles and walls. We find that the slopes of the bulldozed mounds of regolith can be as high as 38–39° on the upstream side, where the grains have been pushed by the scoop. Once the scoop loses contact with the regolith, some of the grains likely come down along the created slope. On the downstream side, where the grains have been pushed away by the scoop with no back sliding once the contact with the scoop was lost, the slopes of the piles are between 49 to 53°. The walls scraped by the vertical sides of the scoop have slope values of 78° and 70°, for the wall W1 and W2, respectively.

The slopes of the piles are larger than that of a pile poured from a given height defined, in non-cohesive granular materials, by an angle of repose that is close to the friction angle at the density of the pile (the larger the falling height, the higher the density and friction angle). Part of the difference in slope angle may be due to the difference in setting up the pile. In their investigation of soil tool interactions in extraterrestrial conditions, Jiang et al. (2017) conducted some 2D DEM modelling of a heap, made up of circular particles of 1.2 mm average diameter, pushed by a vertical blade. Compared to the 30° angle of repose of their material (a value that they found independent of the gravity field), they observed that the downstream slope of the pushed heap was 45°, a value comparable to that observed in pile P1. They also found that this angle increased to 47° when accounting for the cohesion resulting from the significant van der Waals inter-grains attractive forces under the high vacuum conditions (10^{-7} Pa) of the Moon. Indeed, the tests conducted on a lunar simulant by Bromwell (1966) and Nelson (1967) under high vacuum and high temperature (394 K) showed an increase in friction angle of 13° and an increase in cohesion of 1.1 kPa. In this regard, it would be interesting to investigate the possible increase in van der Waals inter-grain forces under Mars atmospheric conditions, so as to better estimate the possible resulting cohesion.

The slopes of the walls W1 and W2 left by the scoop's scrapes are significantly larger than the slopes of the piles and slope failure was not observed on these walls. This result can be interpreted as a result of the presence of some cohesive forces in the undisturbed regolith within the mounds.

6.5 Seismic Observations of the Hammering

InSight's seismic experiment for interior structure (SEIS) seismometer assembly was installed on Mars to monitor the martian seismicity and image the deep interior of the planet

with seismological methods (e.g., Lognonné et al. 2019; Stähler et al. 2021). Due to the limited reach of the IDA, SEIS was placed on the ground about 1.2 m away from HP³. Induced ground displacement and mechanical vibrations from all HP³ related operations such as the mole hammering and IDA activities to assist the hammering generated seismic (elastic) signals that were recorded by SEIS. These seismic signals were used to support the mole anomaly recovery activities. For example, the seismometer was used as a tiltmeter to monitor the quality of the preload force exerted on the mole by the IDA (see Sect. 5.4).

In addition, the seismic recordings of mole hammering provide a unique opportunity to study the near-surface structure and elastic parameters at the InSight landing site. Knowing these parameters is relevant, for example, to understand the coupling of the seismometer to the ground, to infer on the local geological structure, composition and history at the landing site, and to collect information on the martian regolith for future missions (Kedar et al. 2017; Golombek et al. 2018). Listening to the HP³ hammering marks, to the best of our knowledge, the first controlled-source seismic experiment ever conducted on another planet (Brinkman et al. 2019). This experiment on Mars can be seen as a continuation of successful seismic experiments on the Moon (Cooper et al. 1974; Sollberger et al. 2016) and on comet 67P/Churyumov-Gerasimenko (Knapmeyer et al. 2016). Interestingly enough, the experiments on comet 67P/Churyumov-Gerasimenko bear some similarity to the mole hammering on Mars in terms of source type and scale.

Seismic studies of the subsurface at the InSight landing site covering the topmost 5 m initially planned to be reached by the mole and the section below include first traveltimes analyses of the first HP³ hammering sessions (Lognonné et al. 2020), compliance inversions (Kenda et al. 2020; Lognonné et al. 2020), and an ambient vibrations Rayleigh wave ellipticity study (Hobiger et al. 2021). These initial seismic investigations suggest a shallow low velocity layer (P-wave velocities < 300 m/s; S-wave velocities < 150 m/s) that cannot be thicker than 1 to 1.5 m. Below 1 to 2 m depth, the fine-grained regolith seems to be mixed with blocky ejecta resulting in increased bulk seismic velocities (P-wave velocities > 700 m/s; S-wave velocities > 400 m/s) as indicated by both the Rayleigh wave analysis and compliance inversions. Below this transition zone, a sequence of high and low velocity layers found by the Rayleigh wave ellipticity inversion for the topmost 200 m is interpreted as a sequence of lava flows inter-fingered with a sedimentary unit. Manga and Wright (2021) have concluded that the seismic velocities in the top 10 km underneath InSight are too low to suggest an ice-saturated cryosphere.

6.5.1 Preparing SEIS for Recording Hammering Signals

Studying the near-surface using the HP³ seismic signals did not address any of the primary InSight mission goals. Furthermore, exploiting the HP³ seismic signals was not conceived before key decisions on the system design were already taken. Therefore, a series of ad-hoc adaptations had to be implemented to realise this opportunistic experiment and extensive feasibility tests had to be performed.

The SEIS sensor assembly was deployed by the IDA on the ground on sol 22. SEIS consists of six seismic sensors, covering a nominal seismic bandwidth from 0.01 to 50 Hz: a three-component very broad band seismometer (VBB) and a three-component short period seismometer (SP), all mounted on a three-legged leveling system. After the sensor assembly was deployed, a wind and thermal shield was placed over SEIS to provide a first level of environmental noise protection.

SEIS is operated using the so-called E-Box housing all acquisition and control electronics. Programmable digital finite impulse response (FIR) filters, for example, are used

to low-pass filter the seismic data before down-sampling in preparation of transmission to Earth (Zweifel et al. 2021). Changing these FIR filters during hammering proved to be critical for successful recording of the hammering signals (Sollberger et al. 2021).

6.5.2 Pre-mission Preparation Activities

The preparation for the recording of HP³ seismic signals began early in the mission (Kedar et al. 2017). In a first phase, the mole seismic source time function was measured and used to generate sets of time series simulating the signals recorded by SEIS from a mole that penetrates through a simple layered model. It was concluded that in spite of the low nominal resolution of the SEIS data relative to the hammer source duration, it would be feasible to retrieve key elastic parameters such as the seismic P-wave and S-wave velocities of the near-surface, including possibly detecting sharp interfaces up to several meters beneath the InSight lander (Golombek et al. 2018; Brinkman et al. 2019).

Once the scientific value of listening to the hammering was demonstrated, an extensive field analogue experiment was carried out in the Mojave Desert, California. The site was selected since it provided a sharp contact between sedimentary and an igneous rock layer, similar to the landing site at Elysium Planitia on Mars. A seismic survey was conducted to characterize the site stratigraphy. A mole engineering model together with broadband seismometers were installed in a similar geometry to the HP³-SEIS configurations planned for Mars. The seismic signals were recorded at 1,000 Hz sampling frequency, and then down-sampled to 100 Hz sampling frequency to simulate SEIS highest nominal resolution setting.

We demonstrated that under those conditions the seismic velocity in the soft sediment can be determined with high fidelity using the HP³ STATIL time tags and the HP³ mole depth. Yet, it was determined that due to the relatively low temporal resolution of SEIS, due to reverberation of the HP³ mole and the fact that the HP³ seismic source shows a double pulse 0.06 s apart (Kedar et al. 2017) caused by double strikes of the hammer mechanism (Sect. 2) that determining the depth of the sediment-rock interface would be challenging. The field experiment highlighted the need to accurately synchronize the SEIS and HP³ clocks to take full advantage of the STATIL hammer stroke time tag and to implement strategies to maximize the temporal resolution.

6.5.3 Regolith Properties from HP³-SEIS

Analysing the seismic signals traveling between the mole and SEIS allows inferring the regolith elastic parameters governing seismic wave propagation (Lognonné et al. 2020; Brinkman et al. 2022). Because of the short travel path of around 1.2 m, the traveltimes of the seismic waves were expected to be on the order of several milliseconds only and therefore shorter than the SEIS sampling interval of 10 ms (governed by the sampling frequency of 100 Hz). In order to reach the necessary high temporal resolution and to record the broad-band hammering signals, we developed a recording and data-processing strategy to overcome the nominal sampling limitations (Sollberger et al. 2021). Firstly, the anti-aliasing FIR filters to prepare the seismic data for down-sampling to the highest nominal sampling frequency of 100 Hz were turned-off during seismic acquisition of most hammering sessions. This resulted in the seismic signals being aliased, containing energy in the frequency range 0–250 Hz but (multiply) folded around the nominal Nyquist frequency of 50 Hz. Based on the assumption that the HP³ hammering signals are highly repeatable (see

Fig. 19a for two example hammer strokes measured on Mars), the original seismic waveforms can be reconstructed at a high virtual sampling rate using a sparseness-promoting algorithm (Sollberger et al. 2021; InSight Mars SEIS Data Service 2020).

To compute seismic velocities, it is important that the mole stroke triggering times are accurately known to compute the absolute traveltimes between the mole and SEIS. Because HP³, SEIS, and the lander operate with independently running clocks, a high-precision clock-correlation procedure had to be designed and implemented.

We analysed around 2,000 traveltime picks extracted from the waveform data displayed in Fig. 19 recorded with the high-resolution SEIS settings (hammering sessions between sol 311 and 632). Based on these traveltimes, we estimated a bulk P- (compressional) and S- (shear) wave velocity of 119_{-21}^{+45} m/s and 63_{-7}^{+11} m/s, respectively, for the regolith volume between the mole and SEIS (Brinkman et al. 2022). Assuming a density of 1200 kg/m^3 , the velocity estimates translate into bulk, shear, and Young's moduli as well as Poisson's ratio of $7.79_{-1.55}^{+1.60}$ MPa, $4.47_{-0.83}^{+2.00}$ MPa, $11.48_{-2.23}^{+5.91}$ MPa, and $0.28_{-0.23}^{+0.12}$, respectively. When interpreting these estimates, one should keep in mind that they were derived from elastic waves with a dominant frequency content of around 40 to 80 Hz (see Fig. 19c).

The observed seismic velocities are interpreted as bulk averages for shallowest few tens of centimeters. The velocity values appear low compared to laboratory measurements for unconsolidated dry quartz sand on Earth. However, extrapolations of laboratory measurements on martian regolith soil simulants to the low gravity (low overburden pressure) conditions at the surface of Mars result in very similar P-wave velocities of 100–120 m/s (Delage et al. 2017; Morgan et al. 2018).

6.5.4 Radiated Seismic Energy from HP³ Hammering

An estimate of the radiated seismic energy, E_R , can be made by integrating over the elastic energy flux from each hammer stroke. Using the formulation of Shearer (2019)

$$E_R = \rho \int_S \int_{-\infty}^{\infty} \alpha (\dot{u}_\alpha^2 + \dot{v}_\alpha^2 + \dot{w}_\alpha^2) dt dS = 4\pi \rho \alpha r^2 I_P \quad (5)$$

with

$$I_P \equiv \int_{-\infty}^{\infty} (\dot{u}_\alpha^2 + \dot{v}_\alpha^2 + \dot{w}_\alpha^2) dt, \quad (6)$$

where ρ marks density assumed to be $\sim 1200 \text{ kg/m}^3$, α is the measured P-wave velocity, \dot{u}_α , \dot{v}_α , and \dot{w}_α are the three SEIS measured components of the ground velocity during a hammer stroke, and r the distance from HP³ to SEIS. It is further assumed that the ~ 25 Hz reverberations observed during each hammer stroke (see Fig. 19b) were excited by the source (as opposed to being excited by the wind), and that the energy measured at SEIS is predominantly P-wave energy radiated spherically from a point source. Averaging over multiple hammer stroke recordings from the hammering session conducted on sol 158, we obtain $E_R \sim 1.3 \times 10^{-3}$ Joules per hammer stroke which may be compared with the mole stroke energy of 0.7 J. Thus, the seismic energy in the hammer signals recorded by SEIS during hammering is less than a percent of the stroke energy when geometrically projected back to the mole tip as the source area. This suggests that only a small part of the mole stroke energy is partitioned into vibrational energy.

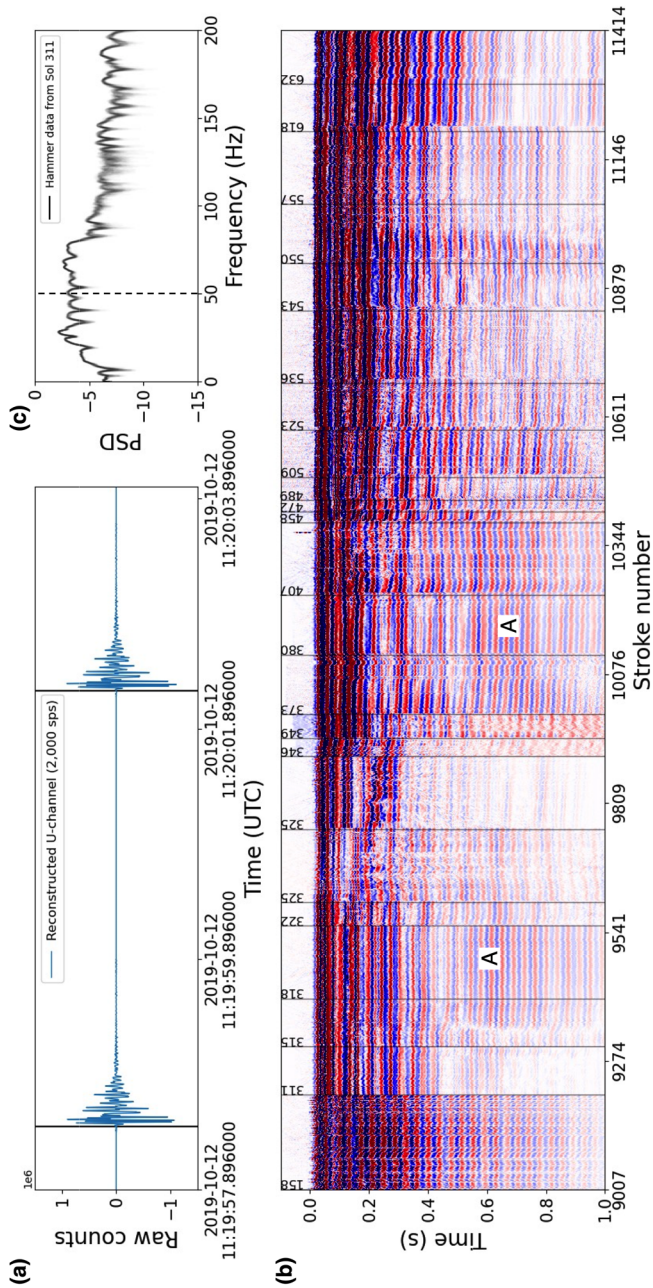


Fig. 19 Seismic data collected during HP³ mole hammering. The SEIS SP data were recorded with an adapted acquisition procedure that allowed reconstructing the broadband waveforms. (a) Waveforms of two subsequent mole strokes separated by around 3.7 s recorded during the diagnostic hammering on sol 158. Vertical black lines mark the hammering time. (b) All broadband east-component SP data recorded for hammering sessions between sol 158 and 632. Vertical bars show the beginnings of the sessions marked with the corresponding sol. Time $t = 0$ s corresponds to the mole hammering time. The seismic signal show clear first arriving energy being interpreted as the P-wave arrival. The mole hammer strokes also excite the 25-Hz resonance denoted with A, which is assumed to originate from vibrations of the SEIS housing and/or leveling system. (c) Power spectral density computed for all data recorded during the hammering on sol 311. Note how the frequency bandwidth of the hammer signal exceeds the Nyquist frequency of 50 Hz of the nominal SEIS acquisition (marked by the dashed line) highlighting the value of the reconstruction method by Sollberger et al. (2021)

6.6 Implications from Thermal Measurements

The thermal properties of the soil around the lander have been probed by the HP³ radiometer, which observes two spots north of the lander (Spohn et al. 2018; Mueller et al. 2020), as well as the thermal sensors inside the HP³ mole termed TEM-A (Thermal Excitation and Measurement – Active (Spohn et al. 2018; Grott et al. 2019)). These measurements are sensitive to different depth ranges and results of the investigations are summarized in Fig. 20.

The surface response to insolation changes is diagnostic of the surface thermal inertia, which is defined as

$$\Gamma = \sqrt{k\rho c_p} \quad (7)$$

where k is thermal conductivity, ρ is density, and c_p is specific heat capacity. For fast changing illumination conditions, measurements are sensitive to shallow depths, while long-term periodic changes probe deeper soil layers. So far, measurements of the surface temperature response to transits of the martian moon Phobos (Mueller et al. 2021) as well as measurements of the temperature response to diurnal insolation changes (Piqueux et al. 2021) have been performed.

The transit measurements are sensitive to the depth range between 0 and 0.4 cm, and a best fitting thermal inertia of $103^{+22}_{-16} \text{ J m}^{-2} \text{ K}^{-1} \text{ s}^{-1/2}$ has been determined for that layer (compare Fig. 20(a), where the layer is indicated in brown). These data are complemented by the analysis of diurnal temperature changes, which are sensitive to about 8 cm depth. For this layer, a best fitting thermal inertia of $183 \pm 25 \text{ J m}^{-2} \text{ K}^{-1} \text{ s}^{-1/2}$ has been determined (Fig. 20(b)). The thermal properties of the deeper soil have been probed by direct thermal conductivity measurements using the mole as a modified line heat source (Grott et al. 2021), and a thermal conductivity of $0.039 \pm 0.002 \text{ W m}^{-1} \text{ K}^{-1}$ has been determined for the 3 to 37 cm depth range (Fig. 20(c)).

To compare the radiometer and TEM-A measurements, thermal inertia can be converted to thermal conductivity using Eq. (7) if some assumptions regarding soil density and heat capacity are made. Here we use a heat capacity of $c_p = 630 \text{ J kg}^{-1} \text{ K}^{-1}$ as appropriate for basaltic sand at 220 K (Morgan et al. 2018) and a soil bulk density of 1211 kg m^{-3} as derived from the active heating experiments (Grott et al. 2021). Resulting values for thermal inertia (Fig. 20c) and thermal conductivity (Fig. 20a–b) are given in gray. Except for the uppermost unconsolidated layer, estimates for the soil thermal conductivity fall within the range expected for uncemented martian soils, which is 0.02 to $0.1 \text{ W m}^{-1} \text{ K}^{-1}$ (Grott et al. 2007).

All measurements of thermal properties indicate that the soil at the landing site is a poor thermal conductor, and the derived soil thermal conductivities place strong constraints on the allowable degree of soil cementation. Only minor amounts of cement are consistent with the derived low thermal conductivities (Piqueux and Christensen 2009a,b). Further study is needed to see how well these constraints can be reconciled with the observed cohesion in the duricrust.

While thermal soil properties determined for the different depth ranges do not indicate layering below the uppermost 0.4 cm, layering can also not be ruled out because the different measurements yield average values in their respective depth ranges. In particular, TEM-A yielded the average thermal conductivity between 3 and 37 cm depth. In order to explore the range of admissible soil properties, we consider a four layer soil model as shown in Fig. 20(d), consisting of a 1 cm thick unconsolidated layer of sand mixed with dust through which the thermal conductivity would increase, a duricrust layer between 1 and 19 cm,

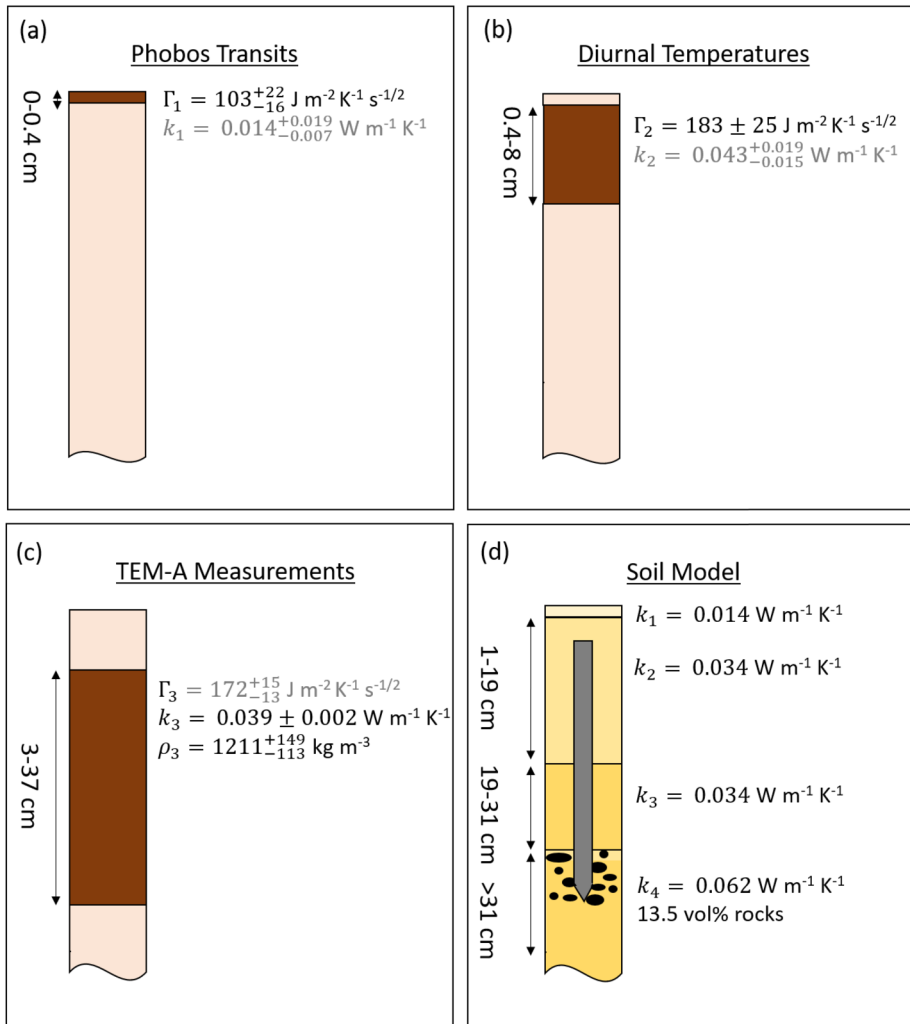


Fig. 20 (a)–(c) Summary of regolith physical properties derived from HP³ RAD and active heating experiments using TEM-A. The sensing depths of the different methods are indicated. Quantities that are immediately calculated from the data such as thermal inertia in panels a and b and thermal conductivity and density in panel c are given in black. Values inferred from the data are given in gray. To convert thermal conductivity to thermal inertia, a soil heat capacity of $630 \text{ J kg}^{-1} \text{ K}^{-1}$ has been assumed (Morgan et al. 2018). (d) Soil thermal model compatible with all observations assuming four regolith layers: A top unconsolidated sand/dust layer, a duricrust, an unconsolidated sand layer, as well as a layer including small rocks or gravel. Thermal conductivity of the rocks was assumed to be $3 \text{ W m}^{-1} \text{ K}^{-1}$

a layer of sand between 19 and 31 cm, and a layer containing gravel or small pebbles below 31 cm. Assuming minimal cementation and a minimum particle size of $100 \mu\text{m}$ compatible with mobilization by winds (Kok et al. 2012), the duricrust and the layer of sand can be assigned a minimum thermal conductivity of $k_{2,3} = 0.034 \text{ W m}^{-1} \text{ K}^{-1}$.

To calculate the rock abundance in the gravel layer compatible with the TEM-A results, we use mixing models for layering parallel to the direction of heat flow during the mea-

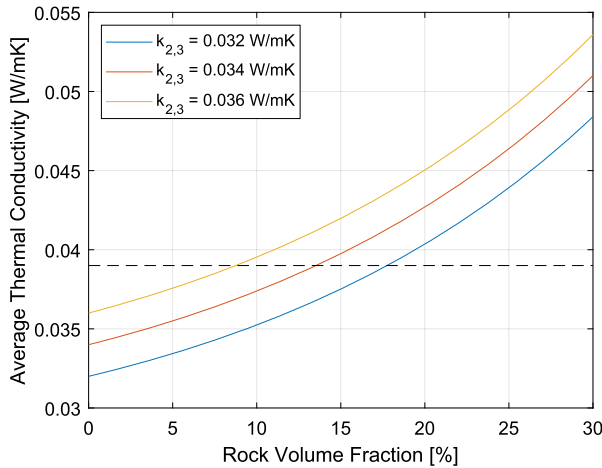


Fig. 21 Average thermal conductivity in the 3 to 37 cm depth range as a function of the volume fraction of stones in a hypothetical gravel layer located below 31 cm depth (compare Fig. 20). Results are shown for three different thermal conductivities $k_{2,3}$ of the uppermost duricrust and intermediate sand layer, respectively. The average thermal conductivity of the entire soil column as measured using TEM-A is indicated by the horizontal dashed line. For 100 μm diameter particles, $k = 0.032$ to $0.036 \text{ W m}^{-1} \text{ K}^{-1}$ (Presley and Christensen 1997). Thus the volume fraction of rocks is limited to be smaller than 18%

surements (Beardsmore and Cull 2001) and determine the maximum thermal conductivity admissible in the gravel layer. We then use mixing laws for randomly mixed material (Beardsmore and Cull 2001) to estimate the rock abundance in the gravel layer itself assuming a rock thermal conductivity of $3 \text{ W m}^{-1} \text{ K}^{-1}$. Results of the calculations are shown in Fig. 21, where the average thermal conductivity is given as a function of the volume fraction of rocks in the gravel layer for three different thermal conductivities $k_{2,3}$ of the duricrust and unconsolidated layer. The average thermal conductivity as determined using TEM-A is indicated by the horizontal dashed line. Results indicate that $\sim 15 \text{ vol}\%$ of rocks in the gravel layer would be compatible with the TEM-A results, and this scenario is summarized in Fig. 20d.

7 Synopsis

The HP³ was a bold experiment, attempting to reach unprecedented depth in the martian regolith with a very compact, low power, and low mass mechanism. Its science goal was to measure the martian surface heat flow, a quantity that has been often modeled (e.g., Schubert and Spohn 1990; Plesa et al. 2018) and that provides an important constraint for the energy budget of the martian interior, its thermal and dynamic history and its composition (e.g., Spohn et al. 2018; Smrekar et al. 2018). Most recently, Khan et al. (2021) have attempted to use the recordings of SEIS to invert for the lithosphere temperature gradient and estimated the heat flow after assuming a value for the thermal conductivity. Their value of about 20 mW/m^2 is consistent with most recent thermal models of Mars.

HP³ proved to have lower performance margins than originally planned and the system encountered an environment more difficult than expected. In a separate paper, Spohn et al. (2022) have discussed lessons learned for the design and the operation of an HP³-type heat

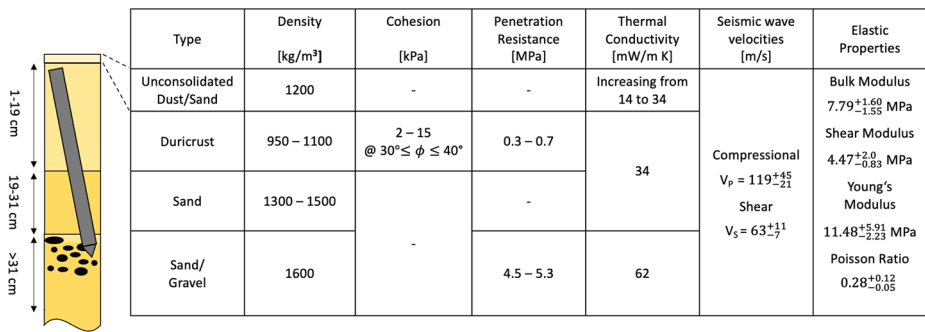


Fig. 22 Model of the martian soil at the HP³ mole pit. The assumed range of internal friction angle ϕ for the listed cohesion value range is indicated

flow probe. They conclude that a more massive design may have been able to meet the challenges, but at the expense of more mass and likely at greater cost. A further dimension in which the effort was challenged was the operations schedule: there was pressure to achieve operation depth ahead of the shadowing thermal wave, and deployment delays eroded the available time. This, in turn, motivated more aggressive (i.e., longer) hammering commands during the initial penetration sols, which may have been detrimental. More generous margins in any of these dimensions may have allowed success, but the Discovery mission framework does not foster large margins.

Although HP³ did not meet its primary science goal, the two years of carefully operating the mole and the robotic arm provided a wealth of data on the martian soil that were not available before. The primary data that HP³ acquired were the radiometer data (Piqueux et al. 2021; Mueller et al. 2021) and the measurements of the thermal conductivity using the TEM-A sensors on the mole (Grott et al. 2021). Power permitting, these data will be continued to be acquired to study the time variability of the thermal inertia and the soil thermal conductivity, the latter to include a study of the effect of the gas pressure in the porous regolith. Inversion of the TEM-A data taken after mole burial suggests that the layer between 3 cm and 37 cm depth has an average density of 1211^{+149}_{-113} kg/m³ consistent with a porosity of $63^{+9}_{-4}\%$ for a grain density of basalt of 3200 kg/m³. This average value encompasses a regolith containing duricrust, sand compacted by hammering, sand fill, and sand with gravel and/or pebbles.

In its attempt to penetrate, the mole acted as a penetrometer as is used in civil engineering and geology to study the properties of soils (e.g., Terzaghi and Peck 1947; Verruijt 2018). Unfortunately, the data were not acquired through a carefully planned soil mechanics experiment. Still, carefully selected data acquired from the mole and scoop operations, the thermal data from the radiometer and TEM-A, and the data from SEIS recording the mole hammering can be combined to form a consistent record of the soil properties as shown in Fig. 22.

Working from the top surface to depth, we find a sand layer possibly mixed with dust of about 1 cm thickness to form the top layer. This layer has been observed in the images taken by the robotic arm instrument deployment camera IDC and has been indented by the feet of the SS and by the scoop, when the latter was pressed onto the surface by the robotic arm. The mechanical strength of the layer is weak, at least much weaker than the duricrust below and was compressed by the 3.8 kPa force per unit area exerted by the arm. The sand has been scraped to form ridges and a slope analysis as reported in Sect. 6.4.2 showed

slopes of 49–53° and 70° and 78° of the fore and side walls of the scrape, respectively. Electrostatic forces may contribute to these high values (in comparison with estimates of the internal friction angle of around 30°) and to the cohesion of the sand. Thermal data reported in Sect. 6.6 suggest a low value of thermal inertia of about $103 \text{ J m}^{-2} \text{ K}^{-1} \text{ s}^{-1/2}$ and – accordingly – a small thermal conductivity of $0.014 \text{ W m}^{-1} \text{ K}^{-1}$ increasing through the layer to $0.034 \text{ W m}^{-1} \text{ K}^{-1}$ and suggesting high porosity. We assign this layer a density of about 1200 kg/m^2 , representative of a mixture of loose basaltic sand with some dust.

Underneath the sand layer, the mole found a duricrust that provided significant resistance to mole penetration of about 0.3 to 0.7 MPa, depending on uncertainties in the timing of the penetration progress. The penetration resistance even at small depth can be explained by significant cohesion. Slope stability analysis as reported in Sect. 6.4.1 after pressing the blade of the scoop into the duricrust and causing part of it to fail suggest a cohesion of 5.8 kPa.

Using the analytical theory of Terzaghi and Peck (1947), as reported in Poganski et al. (2017) the penetration resistance can be related to the cohesion and the angle of internal friction ϕ . At small depth, the relation is

$$\sigma_P \approx c(\chi - 1) \frac{(1 + \sin \phi)\chi - 1}{\chi - 1} \cot \phi \quad (8)$$

with

$$\chi \equiv \frac{1 + \sin \phi}{1 - \sin \phi} e^{\pi \tan \phi} \quad (9)$$

Assuming an angle of internal friction of 30°–40° and a penetration resistance of 0.3 to 0.7 MPa as inferred from the penetration rate during the first 77 strokes (Sect. 6.2.2), Eq. (8) suggests a cohesion of about 2–15 kPa, consistent with the estimate from slope stability analysis, given the uncertainties. A comparison with the latter estimate tends to favour a penetration rate in the upper half of the range of values given in Sect. 6.2.1 and in the lower half of the range of penetration resistance values given in Sect. 6.2.2. It should be noted, however, that even a cohesion of 15 kPa is small in comparison with cohesion values from terrestrial soils. Grott et al. (2021) have argued that the thermal conductivity of 0.034 W/m K inferred from the TEM-A data would be difficult to reconcile with extensive bridges of cement between sand grains. The actual cohesion of the duricrust may possibly be acquired with thin layers of cementation that would still be consistent with a small thermal conductivity. Electrostatic attraction and interlocking of grains may also contribute to the cohesion.

The thickness of the duricrust could not be directly measured. The digital elevation data for the pit discussed in Sect. 5.3 and the images taken by the IDC suggest a thickness of at least 7 cm while we have argued from the distance of the mole backing out for a thickness of about 20 cm in Sect. 6.3.

In Sect. 6.1 we explain the formation of the pit as a result of penetration accompanied by a precession of the mole while grinding the duricrust to sand that partially filled the pit. The inferred ratio of the densities between the duricrust and the sand depends on the thickness of the former and on the compaction of the sand upon penetration and is thus uncertain. Reasonable values consistent with the average density from the TEM-A data and the values given by Morgan et al. (2018) are $950\text{--}1100 \text{ kg/m}^3$ for the duricrust and $1300\text{--}1500 \text{ kg/m}^3$ for the sand layer extending from the bottom of the duricrust to a depth of about 31 cm where the mole hit a more resistant layer. The mole likely penetrated through the sand layer at a

rate of around 0.8 mm/stroke suggesting a penetration resistance of around 0.8 MPa. The duricrust could have formed from this sand by low water-to-rock ratio aqueous reactions (e.g., Banin et al. 1992; Haskin et al. 2005; Hurowitz et al. 2006).

After penetrating to a depth of 31 cm (or 33 cm measured along the mole) the mole encountered a layer into which it penetrated about 6 cm vertically aided by pinning and back cap pushing at a rate of only ~ 0.1 mm/stroke or even less. A rate, that is approximately by an order of magnitude smaller than the rate estimated for the duricrust and the sand layer underneath it. The small penetration rate suggests a penetration resistance of about 5 MPa. We can only speculate about the nature of this layer. A significant reduction of penetration rate has been observed in the laboratory when penetration through a layer of gravel was attempted (Wippermann et al. 2020). The size of the gravel stones was about the size of the mole diameter, up to a small multiple thereof. Such a layer of gravel may be present as buried ejecta from an impact crater (Golombek et al. 2020a). It is also conceivable although less likely that the mole has compacted the sand in front of the tip during the ~ 9000 hammer strokes on sols 92 and 94 and provided sufficient resistance. While the penetration resistance undoubtedly increases with increasing compaction it is questionable whether the mole could have sufficiently increased the relative density in a layer of four times its radius. Thermal modelling shows that the TEM-A data would be consistent with a layer of almost twice the conductivity of the duricrust with a rock fraction of 15 vol-%. Taking a grain density of martian crust basalt of 3200 kg/m^3 and a bulk density of the sand of 1300 kg/m^3 we estimate a bulk density of the gravel layer of 1600 kg/m^3 .

Recordings of the hammer signals of the mole have been used to estimate a seismic bulk P- and S-wave velocity of $119^{+45}_{-21} \text{ m/s}$ and $63^{+11}_{-7} \text{ m/s}$, respectively, as well as the elastic moduli such as a shear modulus of $4.47^{+2.00}_{-0.83} \text{ MPa}$ (Brinkman et al. 2022) as discussed in Sect. 6.5. Civil engineers and soil scientists have attempted to relate the shear modulus of soils to their shear strengths and find empirical relations of the form

$$G \approx A S^\beta \quad (10)$$

where G is the shear modulus, A and β are empirical constants and S is the shear strength which we identify at low confining pressure with the cohesion (e.g., Hardin and Drnevich 1972). Hara et al. (1974) have collected data on 25 terrestrial sites and find β to be close to 1 while the values for $A = G/S$ at $\beta \approx 1$ cluster around 500, but range up to 1600. It should be noted, however, that these empirical values are for the undrained – that is water saturated – shear strength. Given $G = 4.47^{+2.00}_{-0.83} \text{ MPa}$ and assuming $A = 500$, we obtain shear strength values between 7.28 and 12.9 kPa deduced from the seismic data. These strength values are in good agreement with the cohesion estimates from the slope stability analysis of 5.8 kPa (see Sect. 6.4.1) and from the penetration resistance estimates of 2–15 kPa.

The proposed layering is consistent with the geology of the InSight landing site (Golombek et al. 2020a). The soils observed at the landing site are generally similar to soils at other landing sites on Mars (Christensen and Moore 1992; Herkenhoff et al. 2008; Golombek et al. 2008) and their origin via impact and eolian processes is likely similar to the Spirit landing site and other Hesperian lava plains on Mars (Golombek et al. 2020b; Warner et al. 2022), but details such as the thickness of duricrust and the detailed layering of the topmost soil may vary significantly.

Supplementary Information The online version contains supplementary material available at <https://doi.org/10.1007/s11214-022-00941-z>.

Acknowledgements The authors thank two anonymous reviewers for valuable suggestions and the operations team at JPL and DLR for their continued support. Part of this work was performed at the Jet Propulsion Laboratory, California Institute of Technology under a contract with NASA. US government support acknowledged. Support of this work by DLR, the Swiss Space Office and CNES is thankfully acknowledged as well as funding from ETH Research Grant ETH-06 17-02. Lab. Navier, Ecole des Ponts (UMR CNRS 8205, Paris) received from CNES a Grant N°6397 (2021).

The seismic waveform data are available from NASA PDS (National Aeronautics and Space Administration Planetary Data System, <https://pds.nasa.gov>; InSight Mars SEIS Data Service, 2019; https://doi.org/10.18715/SEIS.INSIGHT.XB_2016). The high-rate seismic data from HP³ hammering were obtained using a reconstruction algorithm and are made available in a public repository at <https://doi.org/10.5281/zenodo.4001920>.

This is InSight Contribution Number 223.

Funding Note Open Access funding enabled and organized by Projekt DEAL.

Declarations

Competing Interests The authors declare that they have no conflict of interest.

Open Access This article is licensed under a Creative Commons Attribution 4.0 International License, which permits use, sharing, adaptation, distribution and reproduction in any medium or format, as long as you give appropriate credit to the original author(s) and the source, provide a link to the Creative Commons licence, and indicate if changes were made. The images or other third party material in this article are included in the article's Creative Commons licence, unless indicated otherwise in a credit line to the material. If material is not included in the article's Creative Commons licence and your intended use is not permitted by statutory regulation or exceeds the permitted use, you will need to obtain permission directly from the copyright holder. To view a copy of this licence, visit <http://creativecommons.org/licenses/by/4.0/>.

References

- Abarca H, Deen R, Hollins G, Zamani P, Maki J, Tinio A, Pariser O, Ayoub F, Toole N, Algermissen S, Soliman T, Lu Y, Golombek M, Calef F, Grimes K, De Cesare C, Sorice C (2019) Image and data processing for InSight lander operations and Science. *Space Sci Rev* 215(B9):14,095–14,104. <https://doi.org/10.1007/s11214-019-0587-9>
- ASTM C1444-00 (2000) Standard test method for measuring the angle of repose of free-flowing mold powders. Standard, ASTM International, West Conshohocken, PA, USA
- Banaszkiewicz M, Seiferlin K, Spohn T, Kargl G, Koemle N (1997) A new method for the determination of thermal conductivity and thermal diffusivity from line heat source measurements. *Rev Sci Instrum* 68:4184–4187
- Banerdt WB, Smrekar SE, Banfield D, Giardini D, Golombek M, Johnson CL, Lognonné P, Spiga A, Spohn T, Perrin C, Stähler SC, Antonangeli D, Asmar S, Beghein C, Bowles N, Bozdog E, Chi P, Christensen U, Clinton J, Collins GS, Daubar I, Dehant V, Drilleau M, Fillingim M, Folkner W, Garcia RF, Garvin J, Grant J, Grott M, Grygorczuk J, Hudson T, Irving JCE, Kargl G, Kawamura T, Kedar S, King S, Knapmeyer-Endrun B, Knapmeyer M, Lemmon M, Lorenz R, Maki JN, Margerin L, McLennan SM, Michaut C, Mimoun D, Mittelholz A, Mocquet A, Morgan P, Mueller NT, Murdoch N, Nagihara S, Newman C, Nimmo F, Panning M, Pike WT, Plesa AC, Rodriguez S, Rodriguez-Manfredi JA, Russell CT, Schmerr N, Siegler M, Stanley S, Stutzmann E, Teanby N, Tromp J, van Driel M, Warner N, Weber R, Wiczorek M (2020) Initial results from the InSight mission on Mars. *Nat Geosci* 13:183–189. <https://doi.org/10.1038/s41561-020-0544-y>
- Banin A, Clark BC, Waenke H (1992) Surface chemistry and mineralogy. In: George M (ed) *Mars*. University of Arizona Press, Tucson, pp 594–625
- Beakawi Al-Hashemi HM, Baghabra Al-Amoudi OS (2018) A review on the angle of repose of granular materials. *Powder Technol* 330:397–417. <https://doi.org/10.1016/j.powtec.2018.02.003>
- Beardsmore GR, Cull JP (2001) *Crustal Heat Flow*. Cambridge University Press, Cambridge
- Brinkman N, Schmelzbach C, Sollberger D, van Driel M, ten Pierick J, Robertsson JOA, Andersson F, Stähler S, Giardini D, Kedar S, Hudson T, Hurst K, KiVely A, Banerdt WB, Grott M, Spohn T, Krause C, Fayon L, Lognonné P, Knapmeyer-Endrun B, Delage P, Pike WT, Horleston A, Teanby N, Vrettos C (2019) The

- first active seismic experiment on Mars to characterize the shallow subsurface structure at the InSight landing site. In: SEG Technical Program Expanded Abstracts, pp 4756–4760. <https://doi.org/10.1190/segam2019-3215661.1>
- Brinkman N, Schmelzbach C, Sollberger D et al (2022) In-situ regolith seismic velocity measurement at the InSight landing site on Mars. *J Geophys Res.* <https://doi.org/10.1190/segam2022JE007229>
- Bromwell LG (1966) The friction of quartz in high vacuum. In: Research Report R66-18. Department of Civil Engineering, MIT, Cambridge
- Carslaw HS, Jaeger J (1959) *Conduction of Heat in Solids*, 2nd edn. Oxford University Press, Oxford
- Charalambous C (2014) *On the Evolution of Particle Fragmentation with Applications to Planetary Surfaces*. Imperial College, London
- Chik Z, Vallejo LE (2005) Characterization of the angle of repose of binary granular materials. *Can Geotech J* 42(2):683–692. <https://doi.org/10.1139/t04-118>
- Christensen P, Moore HJ (1992) The Martian surface layer. In: Kieffer HH, Jakosky BM, Snyder CW, Matthews MS (eds) *Mars*. University of Arizona Press, Tucson
- Cooper MR, Kovach RL, Watkins JS (1974) Lunar near-surface structure. *Rev Geophys* 12(3):291–308
- Delage P, Karakostas F, Dhemaied A, Belmokhtar M, Lognonné P, Golombek M, De Laure E, Hurst K, Dupla JC, Kedar S, Cui YJ, Banerdt B (2017) An investigation of the mechanical properties of some Martian regolith simulants with respect to the surface properties at the InSight mission landing site. *Space Sci Rev* 211:191–213. <https://doi.org/10.1007/s11214-017-0339-7>
- Garvin B, Dotson R, Williams N, Maki J, Deen R, Abarca H, Ruoff N, Trebi-Ollennu A (2019) Microtopography of the Mars InSight landing site: geological implications. In: *Lunar and Planetary Science Conference Abstract* 2132
- Golombek M, Grant J, Crumpler L, Greeley R, Arvidson R, Bell J III, Weitz C, Sullivan R, Christensen P, Soderblom L, Squyres S (2006) Erosion rates at the Mars Exploration Rover landing sites and long-term climate change on Mars. *J Geophys Res* 111:E12S10. <https://doi.org/10.1029/2006JE002754>
- Golombek MP, Haldemann AFC, Simpson RA, Ferguson RL, Putzig NE, Arvidson RA, Bell JF, Mellon MT (2008) Martian surface properties from joint analysis of orbital, Earth-based, and surface observations. In: Bell JF (ed) *The Martian Surface: Composition, Mineralogy and Physical Properties*. Cambridge University Press, Cambridge, pp 468–498. <https://doi.org/10.1017/CBO9780511536076.022>
- Golombek M, Kipp D, Warner N et al (2017) Selection of the InSight landing site. *Space Sci Rev* 211:5–95. <https://doi.org/10.1007/s11214-016-0321-9>
- Golombek M, Grott M, Kargl G, Andrade J, Marshall J, Warner N, Teanby NA, Ansan V, Hauber E, Voigt J, Lichtenheldt R, Knapmeyer-Endrun B, Daubar IJ, Kipp D, Muller N, Lognonné P, Schmelzbach C, Banfield D, Trebi-Ollennu A, Maki J, Kedar S, Mimoun D, Murdoch N, Piqueux S, Delage P, Pike WT, Charalambous C, Lorenz C, Fayon L, Lucas A, Rodriguez S, Morgan P, Spiga A, Panning M, Spohn T, Smrekar S, Gudkova T, Garcia R, Giardini D, Christensen U, Nicollier T, Sollberger D, Robertsson J, Ali K, Kenda B, Banerdt WB (2018) Geology and physical properties investigations by the InSight lander. *Space Sci Rev* 214(5):84. <https://doi.org/10.1007/s11214-018-0512-7>
- Golombek M, Warner NH, Grant JA, Hauber E, Ansan V, Weitz CM, Williams N, Charalambous C, Wilson SA, DeMott A, Kopp M, Lethcoe-Wilson H, Berger L, Hausmann R, Marteau E, Vrettos C, Trussell A, Folkner W, Le Maistre S, Mueller N, Grott M, Spohn T, Piqueux S, Millour E, Forget F, Daubar I, Murdoch N, Lognonné P, Perrin C, Rodriguez S, Pike WT, Parker T, Maki J, Abarca H, Deen R, Hall J, Andres P, Ruoff N, Calef F, Smrekar S, Baker MM, Banks M, Spiga A, Banfield D, Garvin J, Newman CE, Banerdt WB (2020a) Geology of the InSight landing site on Mars. *Nat Commun* 11:1014. <https://doi.org/10.1038/s41467-020-14679-1>
- Golombek M, Williams N, Warner NH, Parker T, Williams MG, Daubar I, Calef F, Grant J, Bailey P, Abarca H, Deen R, Ruoff N, Maki J, McEwen A, Baugh N, Block K, Tampari L, Call J, Ladewig J, Stoltz A, Weems WA, Mora-Sotomayor L, Torres J, Johnson M, Kennedy T, Sklyanskiy E (2020b) Location and setting of the Mars InSight lander, instruments, and landing site. *Earth Space Sci* 7(10):e01248. <https://doi.org/10.1029/2020EA001248>
- Grant JA, Arvidson R, Bell JF, Cabrol NA, Carr MH, Christensen P, Crumpler L, Marais DJD, Ehlmann BL, Farmer J, Golombek M, Grant FD, Greeley R, Herkenhoff K, Li R, McSweeney HY, Ming DW, Moersch J, Rice JW, Ruff S, Richter L, Squyres S, Sullivan R, Weitz C (2004) Surficial deposits at Gusev crater along spirit rover traverses. *Science* 305(5685):807–810. <https://doi.org/10.1126/science.1099849>
- Grant JA, Arvidson RE, Crumpler LS, Golombek MP, Hahn B, Haldemann AFC, Li R, Soderblom LA, Squyres SW, Wright SP, Watters WA (2006) Crater gradation in Gusev crater and Meridiani Planum, Mars. *J Geophys Res, Planets* 111(E2):E02S08. <https://doi.org/10.1029/2005JE002465>
- Grant J, Golombek M, Wilson S, Farley K, Williford K, Chen A (2018) The science process for selecting the landing site for the 2020 Mars rover. *Planet Space Sci.* <https://doi.org/10.1016/j.pss.2018.07.001>
- Grant JA, Warner NH, Weitz CW, Golombek MP, Wilson SA, Baker M, Hauber E, Ansan V, Charalambous C, Williams N, Calef F, Pike WT, DeMott A, Kopp M, Lethcoe H, Banks ME (2020) Degradation of

- Homestead Hollow at the InSight landing site based on the distribution and properties of local deposits. *J Geophys Res, Planets* 125(E4):e2019JE006350. <https://doi.org/10.1029/2019JE006350>
- Grott M (2009) Thermal disturbances caused by lander shadowing and the measurability of the Martian planetary heat flow. *Planet Space Sci* 57(1):71–77. <https://doi.org/10.1016/j.pss.2008.11.005>
- Grott M, Helbert J, Nadalini R (2007) Thermal structure of Martian soil and the measurability of the planetary heat flow. *J Geophys Res, Planets* 112(E9):E09004. <https://doi.org/10.1029/2007JE002905>
- Grott M, Spohn T, Knollenberg J, Krause C, Scharringhausen M, Wippermann T, Smrekar SE, Hudson TL, Banerdt WB (2019) Calibration of the heat flow and physical properties package (HP³) for the InSight Mars mission. *Earth Space Sci* 6(12):2556–2574. <https://doi.org/10.1029/2019EA000670>
- Grott M, Spohn T, Knollenberg J, Krause C, Hudson TL, Piqueux S, Müller N, Golombek M, Vrettos C, Marteau E, Nagihara S, Morgan P, Murphy JP, Siegler M, King SD, Smrekar SE, Banerdt WB (2021) Thermal conductivity of the Martian soil at the InSight landing site from HP³ active heating experiments. *J Geophys Res, Planets* 126(7):e06861. <https://doi.org/10.1029/2021JE006861>
- Hara A, Ohta T, Niwa M, Tanaka S, Banno T (1974) Shear modulus and shear strength of cohesive soils. *Soil Found* 14(3):1–12. https://doi.org/10.3208/sandf1972.14.3_1
- Hardin B, Drnevich V (1972) Shear modulus and damping in soils: design equations and curves. *J Soil Mech Found Div* 97(SM 8):667–692
- Haskin L, Wang A, Bradley L et al (2005) Water alteration of rocks and soils on Mars at the Spirit rover site in Gusev crater. *Nature* 436:66–69. <https://doi.org/10.1038/nature03640>
- Herkenhoff KE, Golombek MP, Guinness EA, Johnson JB, Kusack A, Richter L, Sullivan RJ, Gorevan S (2008) In-situ observations of the physical properties of the Martian surface. In: Bell JF (ed) *The Martian Surface: Composition, Mineralogy and Physical Properties*. Cambridge University Press, Cambridge, pp 451–467. <https://doi.org/10.1017/CBO9780511536076.021>
- Hobiger M, Hallo M, Schmelzbach C, Stähler SC, Fäh D, Giardini D, Golombek M, Clinton J, Dahmen N, Zenhäusern G, Knapmeyer-Endrun B, Carrasco S, Charalambous C, Hurst K, Kedar S, Banerdt WB (2021) The shallow structure of Mars at the InSight landing site from inversion of ambient vibrations. *Nat Commun* 12:6756. <https://doi.org/10.1038/s41467-021-26957-7>
- Hurowitz S, McLennan S, Tosca N et al (2006) In situ and experimental evidence for acidic weathering of rocks and soils on Mars. *J Geophys Res* 111:E02S19. <https://doi.org/10.1029/2005JE002515>
- InSight Mars SEIS Data Service (2020) SEIS reconstructed data from HP³ hammering. <https://doi.org/10.5281/zenodo.4001920>
- Jiang M, Xi B, Arroyo M, Rodriguez-Dono A (2017) Dem simulation of soil-tool interaction under extraterrestrial environmental effects. *J Terramech* 71:1–13. <https://doi.org/10.1016/j.jterra.2017.01.002>
- Kedar S, Andrade J, Banerdt B, Delage P, Golombek M, Grott M, Hudson T, Kiely A, Knapmeyer M, Knapmeyer-Endrun B, Krause C, Kawamura T, Lognonne P, Pike T, Ruan Y, Spohn T, Teanby N, Tromp J, Wookey J (2017) Analysis of regolith properties using seismic signals generated by InSight's HP³ penetrator. *Space Sci Rev* 211:315–337. <https://doi.org/10.1007/s11214-017-0391-3>
- Kenda B, Drilleau M, Garcia RF, Kawamura T, Murdoch N, Compaire N, Lognonné P, Spiga A, Widmer-Schmidrig R, Delage P et al (2020) Subsurface structure at the InSight landing site from compliance measurements by seismic and meteorological experiments. *J Geophys Res, Planets* 125:e2020JE006387. <https://doi.org/10.1029/2020JE006387>
- Khan A, Ceylan S, van Driel M, Giardini D, Lognonné P, Samuel H, Schmerr NC, Stähler SC, Duran AC, Huang Q, Kim D, Broquet A, Charalambous C, Clinton JF, Davis PM, Drilleau M, Karakostas F, Lekic V, McLennan SM, Maguire RR, Michaut C, Panning MP, Pike WT, Pinot B, Plasman M, Scholz JR, Widmer-Schmidrig R, Spohn T, Smrekar SE, Banerdt WB (2021) Upper mantle structure of Mars from InSight seismic data. *Science* 373(6553):434–438. <https://doi.org/10.1126/science.abf2966>
- Knapmeyer M, Fischer HH, Knollenberg J, Seidensticker K, Thiel K, Arnold W, Schmidt W, Faber C, Finke F, Möhlmann D (2016) The SESAME/CASSE instrument listening to the MUPUS PEN insertion phase on comet 67P/Churyumov–Gerasimenko. *Acta Astronaut* 125:234–249. <https://doi.org/10.1016/j.actaastro.2016.02.018>
- Kok JF, Parteli EJR, Michaels TI, Karam DB (2012) The physics of wind-blown sand and dust. *Rep Prog Phys* 75(10):106901. <https://doi.org/10.1088/0034-4885/75/10/106901>
- Krömer O, Scharringhausen M, Fittock M, Tsakyridis G, Wippermann T, Witte L, Grott M, Knollenberg J, Spohn T, Krause C, Hudson TL, Lichtenheldt R, Grygorczuk J, Wisniewski L (2019) Design details of the HP³ mole onboard the InSight mission. *Acta Astronaut* 164:152–167. <https://doi.org/10.1016/j.actaastro.2019.06.031>
- Lichtenheldt R, Krömer O (2016) Soil modeling for InSight's HP³-Mole: from highly accurate particle-based towards fast empirical models. In: *Proceedings of Earth and Space 2016*. <https://doi.org/10.1061/9780784479971.016>
- Lognonné P, Banerdt WB, Giardini D, Pike WT, Christensen U, Laudet P, de Raucourt S, Zweifel P, Calcutt S, Bierwirth M, Hurst KJ, Ijpelaar F, Umland JW, Llorca-Cejudo R, Larson SA, Garcia RF, Kedar S,


- Knapmeyer-Endrun B, Mimoun D, Mocquet A, Panning MP, Weber RC, Sylvestre-Baron A, Pont G, Verdier N, Kerjean L, Facto LJ, Gharakanian V, Feldman JE, Hoffman TL, Klein DB, Klein K, Onufer NP, Paredes-Garcia J, Petkov MP, Willis JR, Smrekar SE, Drilleau M, Gabsi T, Nebut T, Robert O, Tillier S, Moreau C, Parise M, Aveni G, Ben Charef S, Bennour Y, Camus T, Dandonneau PA, Desfoux C, Lecomte B, Pot O, Revuz P, Mance D, tenPierick J, Bowles NE, Charalambous C, Delahuntz AK, Hurley J, Irshad R, Liu H, Mukherjee AG, Standley IM, Stott AE, Temple J, Warren T, Eberhardt M, Kramer A, Kühne W, Miettinen EP, Monecke M, Aicardi C, André M, Baroukh J, Borrien A, Bouisset A, Boutte P, Brethomé K, Brysbaert C, Carlier T, Deleuze M, Desmarres JM, Dilhan D, Doucet C, Faye D, Faye-Refalo N, Gonzalez R, Imbert C, Larigauderie C, Locatelli E, Luno L, Meyer JR, Mialhe F, Mouret J, Nonon M, Pahn Y, Paillet A, Pasquier P, Perez G, Perez R, Perrin L, Pouilloux B, Rosak A, Savin de Larclause I, Sicre J, Sodki M, Toulemont N, Vella B, Yana C, Alibay F, Avalos OM, Balzer MA, Bhandari P, Blanco E, Bone BD, Bousman JC, Bruneau P, Calef FJ, Calvet RJ, D'Agostino SA, de los Santos G, Deen RG, Denise RW, Ervin J, Ferraro NW, Gengl HE, Grinblat F, Hernandez D, Hetzel M, Johnson ME, Khachikyan L, Lin JY, Madzunkov SM, Marshall SL, Mikellides IG, Miller EA, Raff W, Singer JE, Sunday CM, Villalvazo JF, Wallace MC, Banfield D, Rodriguez-Manfredi JA, Russell CT, Trebi-Ollennu A, Maki JN, Beucler E, Böse M, Bonjour C, Berenguer JL, Ceylan S, Clinton J, Conejero V, Daubar I, Dehant V, Delage P, Euchner F, Estève I, Fayon L, Ferraioli L, Johnson CL, Gagnepain-Beyneix J, Golombek M, Khan A, Kawamura T, Kenda B, Labrot P, Murdoch N, Pardo C, Perrin C, Pou L, Sauron A, Savoie D, Stähler S, Stutzmann E, Teanby NA, Tromp J, van Driel M, Wieczorek M, Widmer-Schmidrig R, Wookey J (2019) SEIS: InSight's seismic experiment for internal structure of Mars. *Space Sci Rev* 215(1):12. <https://doi.org/10.1007/s11214-018-0574-6>
- Lognonné P, Banerdt WB, Pike WT, Giardini D, Christensen U, Garcia RF, Kawamura T, Kedar S, Knapmeyer-Endrun B, Margerin L, Nimmo F, Panning M, Tauzin B, Scholz JR, Antonangeli D, Barkaoui S, Beucler E, Bissig F, Brinkman N, Calvet M, Ceylan S, Charalambous C, Davis P, van Driel M, Drilleau M, Fayon L, Joshi R, Kenda B, Khan A, Knapmeyer M, Lekic V, McClean J, Mimoun D, Murdoch N, Pan L, Perrin C, Pinot B, Pou L, Menina S, Rodriguez S, Schmelzbach C, Schmerr N, Sollberger D, Spiga A, Stähler S, Stott A, Stutzmann E, Tharimena S, Widmer-Schmidrig R, Andersson F, Ansan V, Beghein C, Böse M, Bozdag E, Clinton J, Daubar I, Delage P, Fuji N, Golombek M, Grott M, Horleston A, Hurst K, Irving J, Jacob A, Knollenberg J, Krasner S, Krause C, Lorenz R, Michaut C, Myhill R, Nissen-Meyer T, ten Pierick J, Plesa AC, Quantin-Nataf C, Robertsson J, Rochas L, Schimmel M, Smrekar S, Spohn T, Teanby N, Tromp J, Vallade J, Verdier N, Vrettos C, Weber R, Banfield D, Barrett E, Bierwirth M, Calcutt S, Compaire N, Johnson C, Mance D, Euchner F, Kerjean L, Mainsant G, Mocquet A, Rodriguez Manfredi JA, Pont G, Laudet P, Nebut T, de Raucourt S, Robert O, Russell CT, Sylvestre-Baron A, Tillier S, Warren T, Wieczorek M, Yana C, Zweifel P (2020) Constraints on the shallow elastic and anelastic structure of Mars from InSight seismic data. *Nat Geosci* 13(3):213–220. <https://doi.org/10.1038/s41561-020-0536-y>
- Maki J, Golombek M, Deen R, Abarca H, Sorice C, Goodsall T, Schwochert M, Lemmon M, Trebi-Ollennu A, Banerdt W (2018) The color cameras on the InSight lander. *Space Sci Rev* 214:105. <https://doi.org/10.1007/s11214-018-0536-z>
- Manga M, Wright V (2021) No cryosphere-confined aquifer below InSight on Mars. *Geophys Res Lett* 48:e2021GL093127. <https://doi.org/10.1029/2021GL093127>
- Moore HJ, Hutton RE, Clow GD, Spitzer CR (1987) Physical properties of the surface materials at the Viking landing sites on Mars. USGS Publications Warehouse
- Morgan P, Grott M, Knapmeyer-Endrun B, Golombek M, Delage P, Lognonné P, Piqueux S, Daubar I, Murdoch N, Charalambous C, Pike WT, Müller N, Hagermann A, Siegler M, Lichtenheldt R, Teanby N, Kedar S (2018a) A pre-landing assessment of regolith properties at the InSight landing site. *Space Sci Rev* 214(6):104. <https://doi.org/10.1007/s11214-018-0537-y>
- Mueller NT, Knollenberg J, Grott M, Kopp E, Walter I, Krause C, Hudson T, Spohn T, Smrekar S (2020) Calibration of the HP³ radiometer on InSight. *Earth Space Sci* 7(5):e01086. <https://doi.org/10.1029/2020EA001086>
- Mueller NT, Piqueux S, Lemmon M, Maki J, Lorenz R, Grott M, Spohn T, Smrekar S, Knollenberg J, Hudson T, Krause C, Millour E, Forget F, Golombek M, Hagermann A, Attree N, Siegler M, Banerdt W (2021) Near surface properties derived from Phobos transits with HP³ RAD on InSight, Mars. *Geophys Res Lett* 48:e2021GL093542. <https://doi.org/10.1029/2021GL093542>
- Nelson JD (1967) Environmental Effects on Engineering Properties of Simulated Luna Soils. PhD Thesis, Illinois Institute of Technology, Chicago
- Piqueux S, Christensen PR (2009a) A model of thermal conductivity for planetary soils: 1. Theory for unconsolidated soils. *J Geophys Res, Planets* 114(E9):E09005. <https://doi.org/10.1029/2008JE003308>
- Piqueux S, Christensen PR (2009b) A model of thermal conductivity for planetary soils: 2. Theory for cemented soils. *J Geophys Res, Planets* 114(E9):E09006. <https://doi.org/10.1029/2008JE003309>

- Piqueux S, Mueller N, Grott M, Siegler M, Millour E, Forget F, Lemmon M, Golombek M, Williams N, Grant J, Warner N, Ansan V, Daubar I, Knollenberg J, Maki J, Spiga A, Banfield D, Spohn T, Smrekar S, Banerdt B (2021) Soil thermophysical properties near the InSight lander derived from 50 sols of radiometer measurements. *J Geophys Res, Planets* 126:e2021JE006859. <https://doi.org/10.1029/2021JE006859>
- Plesa AC, Padovan S, Tosi N, Breuer D, Grott M, Wieczorek MA, Spohn T, Smrekar SE, Banerdt WB (2018) The thermal state and interior structure of Mars. *Geophys Res Lett* 45(22):12,198–12,209. <https://doi.org/10.1029/2018GL080728>
- Poganski J, Kömle NI, Kargl G, Schweiger HF, Grott M, Spohn T, Krömer O, Krause C, Wippermann T, Tsakyridis G, Fittock M, Lichtenheldt R, Vrettos C, Andrade JE (2017) Extended pile driving model to predict the penetration of the InSight/HP³ mole into the Martian soil. *Space Sci Rev* 211:217–236. <https://doi.org/10.1007/s11214-016-0302-z>
- Presley MA, Christensen PR (1997) The effect of bulk density and particle size sorting on the thermal conductivity of particulate materials under Martian atmospheric pressures. *J Geophys Res, Planets* 102(E4):9221–9230. <https://doi.org/10.1029/97JE00271>
- Rahim A, Prasad SN, George KP (2004) Dynamic cone penetration resistance of soils: theory and evaluation. In: *Geotechnical Engineering for Transportation Projects*, pp 1755–1767. [https://doi.org/10.1061/40744\(154\)169](https://doi.org/10.1061/40744(154)169)
- Reershemius S, Fittock M, Hudson TL, Sasaki K, Scharringhausen M, Spohn T, Sprowitz T, Wippermann T (2019) Structure development of the HP³ instrument support system for the Mars mission InSight. *Acta Astronaut* 164:9–22. <https://doi.org/10.1016/j.actaastro.2019.06.035>
- Rummel JD, Beatty DW, Jones MA, Bakermans C, Barlow NG, Boston PJ, Chevrier VF, Clark BC, de Vera JPP, Gough RV, Hallsworth JE, Head JW, Hipkin VJ, Kieft TL, McEwen AS, Mellon MT, Mikucki JA, Nicholson WL, Omelon CR, Peterson R, Roden EE, Sherwood Lollar B, Tanaka KL, Viola D, Wray JJ (2014) A new analysis of Mars “special regions”: findings of the second MEPAG special regions science analysis group (SR-SAG2). *Astrobiology* 14(11):887–968. <https://doi.org/10.1089/ast.2014.1227>. PMID: 25401393
- Salgado R, Prezzi M (2007) Computation of cavity expansion pressure and penetration resistance in sands. *Int J Geomech* 7(4):251–265. [https://doi.org/10.1061/\(ASCE\)1532-3641\(2007\)7:4\(251\)](https://doi.org/10.1061/(ASCE)1532-3641(2007)7:4(251))
- Salgado R, Mitchell JK, Jamiolkowski M (1997) Cavity expansion and penetration resistance in sand. *J Geotech Geoenviron Eng* 123(4):344–354. [https://doi.org/10.1061/\(ASCE\)1090-0241\(1997\)123:4\(344\)](https://doi.org/10.1061/(ASCE)1090-0241(1997)123:4(344))
- Schubert G, Spohn T (1990) Thermal history of Mars and the sulfur content of its core. *J Geophys Res* 95(B9):14,095–14,104. <https://doi.org/10.1029/JB095iB09p14095>
- Shearer PM (2019) *Introduction to Seismology*, 3rd edn. Cambridge University Press, Cambridge. <https://doi.org/10.1017/9781316877111>
- Siegler S, Smrekar SE, Grott M, Piqueux S, Mueller N, Williams N, Plesa A, Spohn T (2017) The InSight Mars Lander and its effect on the subsurface thermal environment. *Space Sci Rev* 211:259–275. <https://doi.org/10.1007/s11214-017-0331-2>
- Smrekar SE, Lognonné P, Spohn T, Banerdt WB, Breuer D, Christensen U, Dehant V, Drilleau M, Folkner W, Fuji N, Garcia RF, Giardini D, Golombek M, Grott M, Gudkova T, Johnson C, Khan A, Langlais B, Mittelholz A, Mocquet A, Myhill R, Panning M, Perrin C, Pike T, Plesa AC, Rivoldini A, Samuel H, Stähler SC, van Driel M, Van Hoolst T, Verhoeven O, Weber R, Wieczorek M (2018) Pre-mission InSights on the interior of Mars. *Space Sci Rev* 215:3. <https://doi.org/10.1007/s11214-018-0563-9>
- Sollberger D, Schmelzbach C, Robertsson JO, Greenhalgh SA, Nakamura Y, Khan A (2016) The shallow elastic structure of the lunar crust: new insights from seismic wavefield gradient analysis. *Geophys Res Lett* 43(19):10,078–10,087. <https://doi.org/10.1002/2016GL070883>
- Sollberger D, Schmelzbach C, Andersson F, Robertsson J, Brinkman N, Kedar S, Banerdt B, Clinton J, van Driel M, Garcia R, Giardini D, Grott M, Haag T, Hudson T, Lognonné P, ten Pierick J, Pike WT, Spohn T, Stähler S, Zweifel P (2021) A reconstruction algorithm for temporally aliased seismic signals recorded by the InSight Mars lander. *Earth Space Sci* 8:e2020EA001234. <https://doi.org/10.1029/2020EA001234>
- Sorice C, Ali KS, Trebi-Ollenu A, Pranay M, Lim G, Bailey P, Hudson TL, Marteau E, Kim J (2021) In-Sight robotic arm testing activities for HP³ mole anomaly recovery on Mars. In: 2021 IEEE Aerospace Conference (50100), pp 1–19. <https://doi.org/10.1109/AERO50100.2021.9438334>
- Spohn T, Grott M, Smrekar SE, Knollenberg J, Hudson TL, Krause C, Müller N, Jänchen J, Börner A, Wippermann T, Krömer O, Lichtenheldt R, Wisniewski L, Grygorczuk J, Fittock M, Rheershemius S, Sprowitz T, Kopp E, Walter I, Plesa AC, Breuer D, Morgan P, Banerdt WB (2018) The heat flow and physical properties package (HP³) for the InSight mission. *Space Sci Rev* 214(5):96. <https://doi.org/10.1007/s11214-018-0531-4>

- Spohn T, Hudson TL, Witte L, Wippermann T, Wisniewski L, Kedziora B, Vrettos C, Lorenz RD, Golombek MP, Lichtenheldt R, Grott M, Knollenberg J, Krause C, Fantinati C, Nagihara S, Grygorczuk J (2022) The InSight-HP³ Mole on Mars: lessons learned from attempts to penetrate to depth in the Martian soil. *Adv Space Res* 69:3140–3163. <https://doi.org/10.1016/j.asr.2022.02.009>
- Stähler SC, Khan A, Banerdt WB, Lognonné P, Giardini D, Ceylan S, Drilleau M, Duran AC, Garcia RF, Huang Q, Kim D, Lekic V, Samuel H, Schimmel M, Schmerr N, Sollberger D, Stutzmann É, Xu Z, Antonangeli D, Charalambous C, Davis PM, Irving JCE, Kawamura T, Knapmeyer M, Maguire R, Marusiak AG, Panning MP, Perrin C, Plesa AC, Rivoldini A, Schmelzbach C, Zenhäusern G, Beucler É, Clinton J, Dahmen N, van Driel M, Gudkova T, Horleston A, Pike WT, Plasman M, Smrekar SE (2021) Seismic detection of the Martian core. *Science* 373(6553):443–448. <https://doi.org/10.1126/science.abi7730>
- Sweeney J, Warner NH, Ganti V, Golombek MP, Lamb MP, Ferguson R, Kirk R (2018) Degradation of 100-m-scale rocky ejecta craters at the InSight landing site on Mars and implications for surface processes and erosion rates in the Hesperian and Amazonian. *J Geophys Res, Planets* 123(10):2732–2759. <https://doi.org/10.1029/2018JE005618>
- Terzaghi K, Peck R (1947) *Theoretical Soil Mechanics*. Wiley, New York
- Trebi-Ollennu A, Kim W, Ali K, Khan O, Soric C, Bailey P, Umland J, Bonitz R, Ciarleglio C, Knight J, Haddad N, Klein K, Nowak S, Klein D, Onufer N, Glazebrook K, Kobeissi B, Baez E, Sarkissian F, Badalian M, Abarca H, Deen R, Yen J, Myint S, Maki J, Pourangi A, Grinblat J, Bone B, Warner N, Singer J, Ervin J, Lin J (2018) InSight Mars lander robotics instrument deployment system. *Space Sci Rev* 214:93. <https://doi.org/10.1007/s11214-018-0520-7>
- Verruijt A (2018) *An Introduction to Soil Mechanics*. Springer, New York
- Warner N, Grant J, Wilson S, Golombek M, DeMott A, Charalambous C, Hauber E, Ansan V, Weitz C, Pike T, Williams N, Banks M, Calef F, Baker M, Kopp M, Deahn N, Lethcoe H, Berger L (2020) An impact crater origin for the InSight landing site at Homestead hollow, Mars: implications for near surface stratigraphy, surface processes, and erosion rates. *J Geophys Res, Planets* 125:e2019JE006333. <https://doi.org/10.1029/2019JE006333>
- Warner N, Golombek M, Ansan V, Marteau E, Williams N, Grant J et al (2022) In situ and orbital stratigraphic characterization of the InSight landing site—a type example of a regolith-covered lava plain on Mars. *J Geophys Res, Planets* 127:e2022JE007232. <https://doi.org/10.1029/2022JE007232>
- Weitz CM, Grant JA, Golombek MP, Warner NH, Hauber E, Ansan V, Wilson SA, Charalambous C, Williams N, Calef F, Pike WT, Lethcoe-Wilson H, Maki J, DeMott A, Kopp M (2020) Comparison of InSight Homestead hollow to hollows at the Spirit landing site. *J Geophys Res, Planets* 125:e2020JE006435. <https://doi.org/10.1029/2020JE006435>
- Wippermann T, Hudson TL, Spohn T, Witte L, Scharringhausen M, Tsakyridis G, Fittock M, Krömer O, Hense S, Grott M, Knollenberg J, Lichtenheldt R (2020) Penetration and performance testing of the HP³ Mole for the InSight Mars mission. *Planet Space Sci* 181:104780. <https://doi.org/10.1016/j.pss.2019.104780>
- Zhang N, Arroyo M, Ciantia MO, Gens A, Butlanska J (2019) Standard penetration testing in a virtual calibration chamber. *Comput Geotech* 111:277–289. <https://doi.org/10.1016/j.compgeo.2019.03.021>
- Zweifel P, Mance D, ten Pierick J, Giardini D, Schmelzbach C, Haag T, Nicollier T, Ceylan S, Stähler S, van Driel M, Sollberger D, Euchner F, Clinton JF, Bierwirth M, Eberhardt M, Lognonné P, Pike WT, Banerdt WB (2021) Seismic high-resolution acquisition electronics for the NASA InSight mission on Mars. *Bull Seismol Soc Am* 111:2909–2923. <https://doi.org/10.1785/0120210071>

Publisher's Note Springer Nature remains neutral with regard to jurisdictional claims in published maps and institutional affiliations.

Authors and Affiliations

T. Spohn^{1,2}  · T.L. Hudson³ · E. Marteau³ · M. Golombek³ · M. Grott² · T. Wippermann⁴ · K.S. Ali³ · C. Schmelzbach⁵ · S. Kedar³ · K. Hurst³ · A. Trebi-Ollennu³ · V. Ansan⁶ · J. Garvin⁷ · J. Knollenberg² · N. Müller² · S. Piqueux³ · R. Lichtenheldt⁸ · C. Krause⁹ · C. Fantinati⁹ · N. Brinkman⁵ · D. Sollberger⁵ · P. Delage¹⁰ · C. Vrettos¹¹ · S. Reershemius⁴ · L. Wisniewski¹² · J. Grygorczuk¹² · J. Robertsson⁵ · P. Edme⁵ · F. Andersson⁵ · O. Krömer¹³ · P. Lognonné¹⁴ · D. Giardini⁵ · S.E. Smrekar³ · W.B. Banerdt³

✉ T. Spohn
tilman.spohn@dlr.de

- ¹ International Space Science Institute, Hallerstrasse 6, 3012 Bern, Switzerland
- ² DLR Institute of Planetary Research, Rutherfordstr. 2, 12489 Berlin, Germany
- ³ Jet Propulsion Laboratory, California Institute of Technology, Oak Grove Drive, Pasadena, CA 91109, USA
- ⁴ DLR Institute of Space Systems, Robert-Hooke-Str. 7, 28359 Bremen, Germany
- ⁵ Department of Earth Sciences, ETH Zürich, Institute of Geophysics, CH-8092 Zürich, Switzerland
- ⁶ Laboratoire de Planétologie et Géodynamique de Nantes, Université de Nantes, 44322 Nantes, France
- ⁷ NASA Goddard Space Flight Center, 8800 Greenbelt Road, Greenbelt, MD 20771, USA
- ⁸ DLR Institute of System Dynamics and Control, Münchener Strasse 20, 82234 Wessling, Germany
- ⁹ DLR MUSC Space Operations and Astronaut Training, Linder Höhe, 51147 Köln, Germany
- ¹⁰ École nationale des ponts et chaussées, Laboratoire Navier, Paris, France
- ¹¹ Department of Civil Engineering, University of Kaiserslautern, Kaiserslautern, Germany
- ¹² Astronika Sp. z o.o., ul. Bartycka 18, 00-716 Warszawa, Poland
- ¹³ Astrium, Bremen, Germany
- ¹⁴ Institut du Physique du Globe Paris, CNRS, Université Paris Cité, Paris, France